The Pennsylvania State University

The Graduate School

Department of Mechanical and Nuclear Engineering

VEHICLE DYNAMIC MODELING FOR THE PREDICTION AND PREVENTION OF VEHICLE ROLLOVER

A Thesis in

Mechanical Engineering

by

John Thomas Cameron

Submitted in Partial Fulfillment
of the Requirements
for the Degree of

Master of Science

December 2005

John Thomas Cameron

The thesis of John Thomas Cameron was reviewed and approved* by the following:

Sean N. Brennan
Assistant Professor of Mechanical Engineering
Thesis Advisor

Bohdan T. Kulakowski
Professor of Mechanical Engineering

H.J. Sommer III
Professor of Mechanical Engineering
Interim Head of the Department of Mechanical Engineering

*Signatures are on file in the Graduate School

ABSTRACT

This work presents results of an initial investigation into models and control strategies suitable to predict and prevent vehicle rollover due to untripped driving maneuvers. Outside of industry, the study of vehicle rollover inclusive of experimental validation, model-based predictive algorithms, and practical controller design is limited. The researcher interested in initiating study on rollover dynamics and control is left with the challenging task of identifying suitable vehicle models from the literature, comparing these models in their ability to match experimental results, and determining suitable parameters for the models and controller gains. This work presents results that address these issues via comparisons between simulation and experimental results. Experimental results are then presented and compared to the output predicted by the various models in the frequency domain and the time domain in order to provide a foundation for the remainder of the work.

Following experimental model validation, a model-based predictive algorithm is developed that can determine a vehicle's propensity to experience wheel-lift (and possibly rollover) as a function of vehicle speed and transient input. This method is rather conservative as a result of the assumptions made in its derivation. Despite this, the method is unique in that its focus is on the entire range of possible driver inputs, rather than static measurements or fixed time domain maneuvers.

For vehicles that are deemed to be susceptible to wheel-lift, various open-loop and closed-loop control strategies are implemented in simulation. The primary assumption in their implementation is that the vehicle in question is equipped with a

steer-by-wire system. The general control strategy behind the rollover mitigation methods examined is to directly modify the drivers steering command in order to mitigate vehicle wheel-lift incidents and enforce a slide before roll condition.

TABLE OF CONTENTS

LIST OF FIGURES

LIST OF TABLES

ACKNOWLEDGEMENTS

First, I'd like to thank and acknowledge the best engineer there could ever be – God. He's gotten me through some really rough spots in the creation of this work, and I don't know if it would have been completed otherwise. I would also like to thank God for creating everything, and thus giving me something to actually model and control.

I would like to thank the Department of Mechanical Engineering and the Pennsylvania Transportation Institute (PTI) for providing the funds used to sponsor this work. Also, very special thanks to PTI and the gentlemen at the Bus Testing Facility for allowing me to use the test track and test vehicle, and to Dr. Sommer for being my reader. Very special thanks go to Dr. Kulakowski as well for agreeing to be a second reader, despite the last minute notification. It is very much appreciated.

Next, I owe a great deal of thanks to my family. They have been my ever present support structure throughout my entire life, and this thesis has been no exception. Thank you so much for being there for me through this and everything else. I love you guys with all my heart.

My advisor, Dr. Sean Brennan, was also incredibly instrumental in my graduate education and in the formation of this work. I want to thank you for taking a chance on me back in the beginning of the lab. It's been a tough journey getting to this point, and I wanted to thank you for helping me get here. You truly are a great teacher.

Finally, I would like to thank all of the great people that I've met at Penn State. I will remember the good times we all had for the rest of my life.

Chapter 1

Introduction

This thesis details the theoretical development of several 2 degree-of-freedom (DOF) and 3DOF dynamic vehicle models found in literature, experimental validation of those models, and simulation-based work on utilizing these models to predict and prevent vehicle rollover. A number of goals are specified for this work and are listed below.

The first is to examine certain commonly used simplifying modeling assumptions in the creation of dynamic models of vehicle rollover behavior. Such an investigation aims to determine how these assumptions affect the order of a model and the complexity of the dynamic representation, and how the assumptions change the relationships between the various parameters. This will aid in the future derivation and use of vehicle models.

The second goal is to determine, by comparison to experimental data, the accuracy of dynamic models for planar and roll dynamics commonly found in literature. This will allow for a detailed and critical examination of the underlying physics of vehicle rollover as well as how the various modeling assumptions made in the formulation affect the resulting response.

The final and most important goal of this work is to use these models to develop effective methods to predict and prevent untripped vehicle rollover incidents. Predictive work includes determining the velocity and inputs necessary to achieve rollover. Prevention methods include the design of controllers that can mitigate or prevent rollover.

1.1 Motivation

There are many motivations for this work ranging from the societal impact of improving vehicle safety, to the purely academic goal of establishing dynamics and theory governing vehicle rollover propensity. These motivations are each outlined below.

1.1.1 Safety Concerns

According to the Center for Disease Control (CDC), from 1999-2002 vehicle accidents were the single largest cause of fatalities for males 44 years and under and for females 34 years and under [1]. The societal impact of vehicle safety is clearer when considering the number of life-years lost. For the same time period, the CDC estimates that for all people who die under the age of 65, accidental death due to motor vehicle accidents claims over 1.2 million potential life years [2]. For people under 65, there are more potential life years lost to automotive accidents than any other cause [2]. These deaths are sudden, and most often strike when a person is at the peak of both their professional and personal/family life.

There are over 11 million motor vehicle crashes per year [3]. Fifty-five thousand of these accidents result in fatalities [3]. The frightening statistic, however, is that while vehicle rollover is involved in only 2.5% of all accidents, it accounts for approximately 20% of all fatalities [3]. That means approximately 250,000 potential life years are lost **per year** due to vehicle rollover.

Following an announcement in June of 2000, NHTSA formally adopted the concept of the static stability factor (SSF) in January of 2001. The SSF is a relatively simple metric that is intended to give consumers a qualitative assessment of a vehicle's resistance to rollover. The SSF is defined as a ratio of track width divided by two times the height of the vehicle CG. This number is then compared to the value of average road friction. A higher number indicates better "rollover stability" [4]. For current production vehicles, the highest value of the SSF is approximately 1.45 [5].

The practical use of the SSF is limited because it is a purely static measurement. It is a measure a vehicle's resistance to rollover based on physical dimensions and only steady-state conditions. While steady-state rollover prevention is important, the SSF factor has little relevance when one considers that NHTSA has never tested a vehicle that will rollover under steady-state turning situations [6]. Most maneuvers leading to rollover are not steady-state, however. Because of increasing public concern about untripped vehicle rollover and as a result of recommendations made by the National Academy of Science, Congress mandated the TREAD Act in October of 2000 to require the National Highway Traffic Safety Administration to find a series of dynamic tests to replace the SSF.

As a result of ongoing experimental research, NHTSA has since developed a number of maneuvers that, given a high enough speed, induce vehicle rollover [7, 8]. These maneuvers were found by repeated experimentation using a wide variety of vehicles to find steering inputs and driving conditions that appear to excite untripped rollover events. However, there is little theoretical foundation to justify the use of one particular steering input or maneuver over another (e.g. whether all the tests are

necessary), or whether the lack of wheel lift and/or rollover on a test maneuver certifies that the vehicle will not exhibit unsafe rollover behavior for *any* maneuver (e.g. whether all the tests are *sufficient*) . This problem of necessity and sufficiency is further exacerbated since, as will be discussed shortly in this thesis, most publications analyzing the theoretical derivation of dynamic rollover models do not correlate results or assumptions with any type of experimentation. Outside of industry, the study of vehicle rollover inclusive of both theoretically sound dynamic models of rollover dynamics and experimental validation is very limited.

1.1.2 Understanding the Physics behind Rollover

The automobile is a highly non-linear dynamic system containing many parameters that are either difficult or (as yet) impossible to directly measure. While many physical parameters such as mass, location of mass center, and inertial properties have been made available by the National Highway Traffic Safety Administration, many common parameters used in vehicle roll models such as suspension stiffness and damping characteristics are not readily available to the experimenter. This makes it difficult or impossible to perform a broad vehicle rollover study that encompasses multiple vehicles without actually having access to the vehicles themselves.

A parameter of significant importance to the study of vehicle rollover that is often overlooked is the driver and his/her reactions to the world. While a number of mathematical representations of the human driver have been developed [9-13], none of them can remove the uncertainty of life and predict exactly how a driver will respond in

an emergency situation. Therefore, any study of rollover must allow for all possible steering responses.

There are two options to the automobile designer wishing to design a vehicle incapable of rollover – design a vehicle chassis or chassis control system very conservatively to mitigate driver inputs that push the vehicle to the limits of safe handling and instability, or modify the driver's input to the vehicle such that instability is avoided. In the past, auto manufacturers have sought chassis modifications as a means to influence stability. This is evidenced by the appearance of various types of active suspensions, electronic stability controls, and traction control systems in modern production vehicles [14].

But recent research is changing focus toward developing new types of assistive devices. For example, research is currently underway to predict, for measured steering inputs, the amount of time that will elapse before wheel-lift will occur. Such predictive methods are developed in order to either provide a warning to drivers or utilize on-board systems to prevent rollover onset. Examples of the development of Time-To-Rollover (TTR) metrics may be found by Chen, working under Huei Peng at the University of Michigan Transportation Research Institute (UMTRI) [15, 16] and Hyun, working under Reza Langari at Texas A&M [17, 18].

The most apparent drawback to such methods is the limited amount of warning given. It was found by Chen that, even under ideal circumstances, the largest forward prediction in time, and hence the largest amount of warning a driver can feasibly use, is 0.3 seconds when considering an SUV [15]. Such warnings are barely at the limit of human reaction times for unexpected events. Thus, there is a clear need for and utility in

an automated system capable of preventing vehicle roll by modifying a vehicle's steering input.

Additionally, current TTR methods primarily rely on setting a threshold for roll angle and/or lateral acceleration. Despite extensive model development by academic researchers, no one has yet been able to consistently match in simulation the rollover threshold predictions found by the NHTSA experimental trials. Whether a model is used to predict the amount of time before this limit is reached, or sensors are used to determine when this limit has been crossed and a TTR is then generated, the lack of simulation-based tools reflects the current lack of understanding of the physics behind vehicle rollover.

The option of allowing a vehicle to actively modify the driver's input is an idea only in its infancy, but there are research precedents. One example is presented by Hosaka and Morakami from Keio University, Japan in [19]. Here, a combination of PD control, state-feedback control, and a disturbance observer were used to either provide additional steering input to or directly modify a driver's steering command to deal with disturbances such as wind gusts for increased yaw stability.

Another example is by Oh et. al., from Hyundai and associated with Hanyang University [20]. Here the authors propose a feedforward control method that imposes an artificial gear ratio on the steering input so that the dynamic behavior of the vehicle may be changed according to the situation. It also discusses the possibility to prevent rollover by not allowing a driver to steer the vehicle into a region where the lateral acceleration is above a certain threshold. Additionally, the system would add more resistive torque to the wheel as the driver approaches this limit, making it more difficult to steer.

Other examples may be found related to increasing the stability of four-wheel steered vehicles as investigated by Ackermann while at the Institute for Robotics and System Dynamics [21] and Plochl at the Institute of Mechanics at the University of Technology in Wien, Austria [22]. Additionally, work done under J. Christian Gerdes at the Dynamic Design Laboratory at Stanford University includes methods that allow improved disturbance rejection to vehicle steering angle [23] and roll limiting techniques [24] which use a combination of a steer-by-wire system and measurements from a Global Positioning System (GPS) and an Inertial Measurement Unit (IMU) to ensure tracking of the desired path.

Despite these finding, the literature remains rather limited in regards to this area. This work seeks to contribute significantly to the rollover mitigation methods that directly modify the driver's steering command in a way such that the driver does not realize the effect of the controller. However, in order to properly accomplish this goal, the physics behind vehicle rollover must first be understood.

1.1.3 Benefit to the Academic Community

Industry publications, while generally far more advanced in the state-of-the-art in rollover control and modeling versus academia, are by necessity limited in the specificity of the algorithm details, implementation results, or model/control tuning parameters presented. The researcher interested in initiating study on rollover dynamics and control is left with the challenging task of identifying suitable vehicle models from the literature, comparing these models in their respective behavior and in their ability to match

experimental results, and determining suitable parameters for the models and controller gains. This work seeks to address these issues via comparisons between simulation and experimental results so that this divide may be bridged.

1.2 Outline of the Remaining Chapters

The remainder of this thesis is organized as follows: Chapter 2 will contain the derivation of a simple linear 2DOF vehicle model that is commonly used to describe the planar dynamics of a non-articulated vehicle. The behavior of this model will be compared to the 3DOF models derived in Chapter 3. These models will include a description for the planar dynamics described by the 2DOF model, and will also include a description of the roll dynamics.

Chapter 4 will describe how the test vehicle was used to take the dynamic measurements necessary for model validation. The types of experiments performed with this system, as well as their results, will be presented in Chapter 5. From these results, a vehicle model will be selected for use in the development of predictive and preventative measures for vehicle rollover.

Chapter 6 will develop a methodology by which a vehicle's propensity to rollover may be determined. Using the information derived from this methodology, design criteria for control synthesis will be drawn. These specifications will be used to develop both open- and closed-loop control methods for rollover mitigation. Final conclusions and a discussion of future work will be outlined in Chapter 7.

[1] "Web-based Injury Statistics Query and Reporting System (WISQARS): Leading Causes of Death Reports, 1999 - 2002," February 8, 2005. Atlanta, Georgia: The Center for Disease Control (CDC), 2002, *http://webappa.cdc.gov/sasweb/ncipc/leadcaus10.html*.

[2] "Web-based Injury Statistics Query and Reporting System (WISQARS): Years of Potential Life Lost (YPLL) Reports, 1999 - 2002," February 8, 2005. Atlanta, Georgia: The Center for Disease Control (CDC), 2002, *http://webapp.cdc.gov/sasweb/ncipc/ypll10.html*.

[3] "Traffic Safety Facts 2003 - Final Report," U.S. Department of Transportation: National Highway Traffic and Safety Board 2004.

[4] "Consumer Information; New Car Assessment Program; Rollover Resistance," National Highway Traffic Safety Administration (NHTSA) Docket No. NHTSA-2001-9663; Notice 3, 2001.

[5] A. Y. Lee, "Coordinated Control of Steering and Anti-Roll Bars to Alter Vehicle Rollover Tendencies," *Journal of Dynamic Systems, Measurement, and Control*, vol. 124, pp. 127, 2002.

[6] United States Department of Transportation, "An Experimental Examination of Selected Maneuvers That May Induce On-Road, Untripped Light Vehicle Rollover – Phase I-A of NHTSA's 1997-1998 Vehicle Rollover Research Program," National Highway Traffic Safety Administration (NHTSA) HS 359 807, August 2001.

[7] United States Department of Transportation, "An Experimental Examination of Selected Maneuvers That May Induce On-Road Untripped, Light Vehicle Rollover - Phase II of NHTSA's 1997-1998 Vehicle Rollover Research Program," National Highway Traffic Safety Administration (NHTSA) HS 808 977, July 1999 1999.

[8] United States Department of Transportation, "A Comprehensive Experimental Examination of Selected Maneuvers That May Induce On-Road, Untripped, Light Vehicle Rollover - Phase IV of NHTSA's Light Vehicle Rollover Research Program," National Highway Traffic Safety Administration HS 809 513, October 2002.

[9] B. Song, D. Delorme, and J. V. Werf, "Cognitive and hybrid model of human driver," Dearbon, MI, USA, 2000.

[10] C. C. Macadam, "Understanding and modeling the human driver," *Vehicle System Dynamics*, vol. 40, pp. 101, 2003.

[11] R. Majjad, U. Kiencke, and H. Koerner, "Design of a hybrid driver model," Detroit, MI, USA, 1998.

[12] K. Guo, H. Ding, J. Zhang, J. Lu, and R. Wang, "Development of a longitudinal and lateral driver model for autonomous vehicle control," *International Journal of Vehicle Design*, vol. 36, pp. 50, 2004.

[13] U. Kiencke, R. Majjad, and S. Kramer, "Modeling and performance analysis of a hybrid driver model," *Control Engineering Practice*, vol. 7, pp. 985, 1999.

[14] D. Konik, R. Bartz, F. Barnthol, H. Bruns, and M. Wimmer, "Dynamic Drive: System Description and Functional Improvements," presented at Proceedings of

the 5th International Symposium on Advanced Vehicle Control (AVEC), Ann Arbor, Michigan, 2000.

[15] B.-C. Chen and H. Peng, "A Real-time Rollover Threat Index for Sports Utility Vehicles," presented at Proceedings of the 1999 American Control Conference, San Diego, California, 1999.

[16] B.-C. Chen and H. Peng, "Rollover Prevention for Sports Utility Vehicles with Human-In-The-Loop Evaluations," presented at Proceedings of the 5th International Symposium on Advanced Vehicle Control (AVEC), Ann Arbor, Michigan, 2000.

[17] D. Hyun and R. Langari, "Predictive Modeling for Rollover Warning of Heavy Vehicles," presented at Proceedings of the 2002 ASME International Mechanical Engineering Congress and Exposition (IMECE), New Orleans, Louisiana, 2002.

[18] D. Hyun, R. Langari, and J. Ochoa, "Vehicle Modeling and Prediction of Rollover Stability Threshold for Tractor-Semitrailers," presented at Proceedings of the 5th International Symposium on Advanced Vehicle Control (AVEC), Ann Arbor, Michigan, 2000.

[19] M. Hosaka and T. Murakami, "Yaw rate control of electric vehicle using steer-by-wire system," presented at Proceedings of the 8th IEEE International Workshop on Advanced Motion Control, Kawasaki, Japan, 2004.

[20] S.-W. Oh, H.-C. Chae, S.-C. Yun, and C.-S. Han, "The Design of a Controller for the Steer-by-Wire System," *JSME International Journal, Series C*, vol. 47, pp. 896-907, 2004.

[21] J. Ackermann, "Robust decoupling, ideal steering dynamics and yaw stabilization of 4WS cars," *Automatica*, vol. 30, pp. 1761, 1994.

[22] M. Plochl and P. Lugner, "Braking behaviour of a 4-wheel-steered automobile with an antilock braking system," *Vehicle System Dynamics*, vol. 25, pp. 547, 1996.

[23] P. Yih, J. Ryu, and J. C. Gerdes, "Modification of vehicle handling characteristics via steer-by-wire," presented at Proceedings of the 2003 American Control Conference, Denver, Colorado, 2003.

[24] C. R. Carlson and J. C. Gerdes, "Optimal Rollover Prevention with Steer-by-Wire and Differential Braking," presented at Proceedings of the 2003 ASME International Mechanical Engineering Congress and Exposition (IMECE), Washington D.C., 2003.

Chapter 2

Two-Degree-of-Freedom-Model

The planar dynamics of the 3DOF chassis dynamics models will be compared to a 2DOF chassis dynamics model commonly found in literature. This chapter will outline the basic assumptions made in the derivation of the 2DOF chassis dynamics model, develop the force equations in terms of the vehicle states by means of Newtonian mechanics, and finally develop the equations of motion from the force equations. The development of these equations is of particular interest as the dynamics in the 3DOF chassis dynamics models are closely related to the 2DOF formulation.

Typically referred to as the "bicycle model", the 2DOF model only exhibits lateral and yaw dynamics. Specific application examples of this model are usually found in papers dealing with tire slip estimation [1], vehicle body slip estimation [2], automated steering controllers [3-5], and vehicle stability [6, 7].

While it does not have any roll dynamics, the bicycle model is considered here as a reference because it is known to provide a reasonable match to experimental data for both lateral acceleration and yaw rate dynamics. This matching is known to be valid only for maneuvers that are not very aggressive [8], roughly those with lateral accelerations less than 0.4 times the acceleration of gravity (g's). Further, the parameters defined for the bicycle model are reused in all of the 3DOF models of this study, and hence the relatively simple 2DOF model can be used to determine a number of the parameters found in the other 3DOF models. Finally, the 2DOF model allows for a comparison of

non-rolling dynamics, e.g. lateral and yaw-rate dynamics, when roll dynamics do not appear in the model.

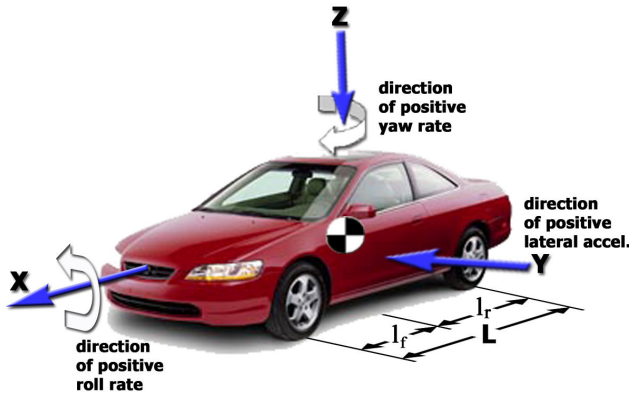

Figure 2.1: Standard SAE Vehicle Coordinate System

2.1 The Bicycle Model - Slip Coordinate Formulation

The 2DOF model of chassis dynamics known as the bicycle model will be derived in a body-fixed coordinate system as specified by the Society of Automotive Engineers (SAE) [9]. This coordinate system is shown in Figure 2.1. Additionally, all nomenclature used in the derivation of the 2DOF model is indicated by Table 2.1. Because the model is formulated with respect to a vehicle frame, a coordinate transformation is required in order to obtain the vehicle's position in the world, e.g. earth-fixed coordinates.

Table 2.1: Nomenclature used in 2DOF chassis dynamics model derivation

Parameter	Definition
U	Longitudinal velocity (body-fixed frame)
r	Yaw rate (angular rate about vertical axis)
m	Vehicle mass
I_{zz}	Inertia about the vertical axis
l_f	front-axle-to-CG distance
l_r	rear-axle-to-CG distance
L	Track of vehicle (lf + lr)
t	Width of vehicle
β	Slip angle of the vehicle body
C_f	Front cornering stiffness
C_r	Rear cornering stiffness
δ_f	Front steering angle

Typically the states used in the state-space representation of the body-coordinates bicycle model are the lateral velocity and yaw rate of the vehicle. The lateral velocity state is occasionally replaced by the angle of the vehicle body relative to its path of travel, called the body slip angle. However, such a substitution will not be done in this study.

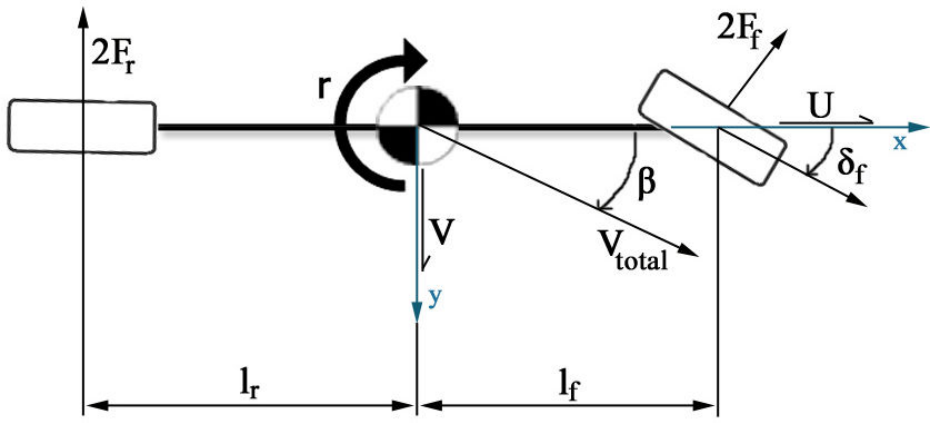

Figure 2.2: Slip Coordinate Model

A complete list of the assumption made in the proceeding formulation is:

- Small angles are assumed allowing the following simplification: $\cos(\theta) \approx 1$, $\sin(\theta) \approx \theta$
- Constant longitudinal (along the x-axis) velocity, e.g. $\dot{U} = 0$
- The lateral force acting on a tire is directly proportional to its slip angle (defined below).
- The tires roll without slipping in the longitudinal direction, e.g. no longitudinal forces (braking or throttle) are being produced that significantly affect lateral forces.
- The forces acting on the right-hand side of the vehicle are symmetric to the forces acting on the left-hand side of the vehicle, hence the four-tire model can be simplified to a 2-tire, single-track model.

From the free-body diagram shown in Figure 2.2, it is seen the last assumption is also the cause for the namesake "bicycle model" whereby the vehicle assumes a single-track model.

2.1.1 Development of Newtonian Force Equations for 2DOF Chassis Dynamics Model

From these assumptions, the force equations will now be developed. Shown in Figure 2.3 is a tire exhibiting lateral-, or side-slip. The side-slip angle α of a tire is defined as the difference between the steering angle of the tire and the tire's local velocity vector V_{tire}. The lateral force and side slip angle are related by the proportionality constant known as cornering stiffness. These constants are usually different for the front and rear, and are defined as C_f for the front tire and C_r for the rear.

Units for this constant are N/rad , with the relationship defined below in Eq. **2.1**. By SAE convention this constant is defined as the *negative* of the force-slip slope.

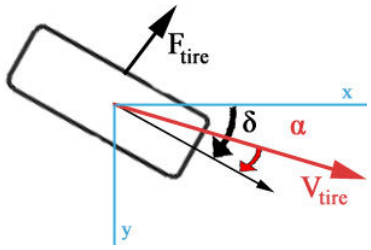

Figure **2.3**: Tire Velocity Vectors

$$F_f = C_f \alpha_f$$
$$F_r = C_r \alpha_r \qquad \textbf{2.1}$$

The slip angles of each tire may be readily expressed in terms of the local velocities local to each tire. We see that the tire's true velocity vector, V_{tire}, is offset from the vehicle's longitudinal axis by the slip angle α. From geometry, the relationship between local velocity components and tire slip angle becomes:

$$\alpha = \tan^{-1}\left(\frac{V_{tire,y}}{V_{tire,x}}\right) \approx \frac{V_{tire,y}}{V_{tire,x}} \qquad \textbf{2.2}$$

Examining Figure **2.2**, one can solve the lateral velocity vectors for the front and rear tire. These become:

$$V_{tire,y,frnt} = -U\beta - l_f r$$
$$V_{tire,y,rear} = l_r r - U\beta \qquad \textbf{2.3}$$

Substituting this definition into Eq. **2.2** gives the slip angles for the front and rear tires to be:

$$\alpha_f = \left(\frac{-U\beta - l_f r}{U}\right) + \delta_f = \delta_f - \beta - \frac{l_f r}{U} \qquad \textbf{2.4}$$

$$\alpha_r = \left(\frac{l_r r - U\beta}{U}\right) = \frac{l_r r}{U} - \beta \qquad \textbf{2.5}$$

Recognizing from geometry that:

$$\beta = \tan^{-1}\left(\frac{V}{U}\right) \approx \frac{V}{U} \qquad \textbf{2.6}$$

we arrive at the equivalent formulation of the slip angle using lateral velocity states. At the front tire this is:

$$\alpha_f = \delta_f - \frac{V + l_f r}{U} \qquad \textbf{2.7}$$

and for the slip angle at the rear tire:

$$\alpha_r = \frac{l_r r - V}{U} \qquad \textbf{2.8}$$

Substitution of these slip angles into the linear tire model leads to the force equations:

$$F_f = C_f \alpha_f = C_f\left(\delta_f - \beta - \frac{l_f}{U}\dot{\psi}\right) = C_f\left(\delta_f - \frac{V + l_f r}{U}\right) \qquad \textbf{2.9}$$

$$F_r = C_r \alpha_r = C_r\left(-\beta + \frac{l_r}{U}\dot{\psi}\right) = C_r\left(\frac{l_r r - V}{U}\right) \qquad \textbf{2.10}$$

2.1.2 Development of Motion Equations for the 2DOF Chassis Dynamics Model

The equations of motion for longitudinal and lateral accelerations will now be developed. By defining $\vec{\omega}$ as the angular velocity of the moving, body-fixed axes (x, y, z), and $\vec{A}$ as a vector whose components are time-varying with respect to the same axes, it has been shown in [10] (pages 84 - 85) that the time derivative of the vector is:

$$\dot{\vec{A}} = \frac{d\vec{A}}{dt} + \vec{\omega} \times \vec{A} \qquad 2.11$$

Using this definition, accelerations defined relative to body-fixed axes may be expressed in vector form by taking the derivative of the velocity vector $\vec{v}$ of the body in plane by the equation:

$$\vec{a} = \vec{\omega} \times \vec{v} + \dot{\vec{v}} \qquad 2.12$$

where $\vec{a}$ is the total acceleration of the body in the plane, $\dot{\vec{v}}$ is the time rate of change of $\vec{v}$, and $\vec{\omega}$ is the body's rate of angular rotation about the body-fixed origin – in this case, the vehicle's yaw rate.

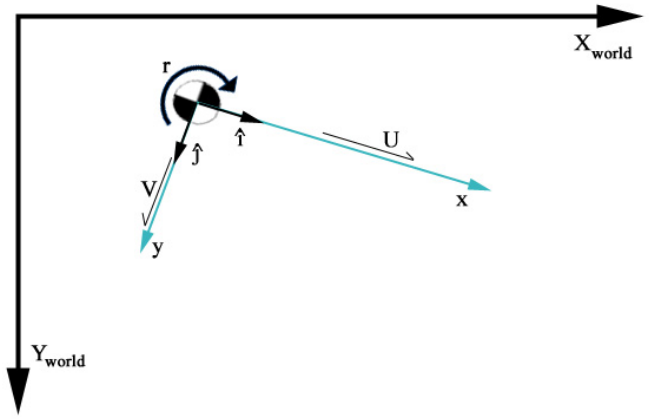

Figure 2.4: Motion of a Body-Fixed Frame

Referring to Figure 2.4, U and V are the time-varying velocities of the body along the x- and y- axes of the body-fixed frame, respectively. By specifying $(\hat{i},\hat{j},\hat{k})$ to be the unit vectors of the body-fixed (x,y,z) coordinate system, and defining:

$$\omega = r \tag{2.13}$$

Eq. 2.12 becomes:

$$\vec{a} = \left(r\hat{k}\times U\hat{i}\right)+\left(r\hat{k}\times V\hat{j}\right)+\dot{U}\hat{i}+\dot{V}\hat{j} \tag{2.14}$$

by Eq. 2.11. Taking the vector cross product:

$$\vec{a} = -r\cdot V\hat{i}+\dot{U}\hat{i}+r\cdot U\hat{j}+\dot{V}\hat{j} \tag{2.15}$$

gives the components of acceleration to be:

$$a_x = \dot{U} - Vr \tag{2.16}$$

$$a_y = \dot{V} + Ur \tag{2.17}$$

The components defined by Eq. 2.16 and Eq. 2.17 allow for the development of the equations of motion in the body-fixed frame. From the assumptions that longitudinal speed is constant and the tires are rolling without slipping, Eq. 2.16 is equal to zero. Therefore there are no net forces acting along the x-axis. By summing forces in the lateral direction and moments about the vertical axis, the resulting equations of motion are:

$$\begin{aligned}\sum F_y &= m\left(\dot{V}+Ur\right) = -2F_f - 2F_r \\ \sum M_z &= I_{zz}\dot{r} = -2F_f l_f + 2F_r l_r\end{aligned} \tag{2.18}$$

where I_{zz} is the moment of inertia of the vehicle about the yaw axis and $\dot{r}$ is the time rate of change of the yaw rate r. Substituting Eq. **2.9** for F_f and Eq. **2.10** for F_r, the system may be placed into the standard state-space representation as:

$$\begin{bmatrix} \dot{V} \\ \dot{r} \end{bmatrix} = \begin{bmatrix} \left(\frac{2(C_f + C_r)}{mU}\right) & \left(\frac{2(l_f C_f - l_r C_r)}{mU} - U\right) \\ \left(\frac{2(l_f C_f - l_r C_r)}{I_{zz} U}\right) & \left(\frac{2(l_r^2 C_r - l_f^2 C_f)}{I_{zz} U}\right) \end{bmatrix} \begin{bmatrix} V \\ r \end{bmatrix} + \begin{bmatrix} -\frac{2C_f}{m} \\ -\frac{2l_f C_f}{I_{zz}} \end{bmatrix} \delta_f \qquad \textbf{2.19}$$

In order to facilitate a simple comparison between this model and the others that will be derived in Chapter 3, an alternate form will be utilized. By rewriting Eq. **2.18** into the form:

$$M\ddot{q} + D\dot{q} + Kq = Fu_f \qquad \textbf{2.20}$$

where:

$$q = \begin{bmatrix} y \\ \psi \\ \phi \end{bmatrix} \qquad \textbf{2.21}$$

This gives the equation:

$$\begin{bmatrix} -m & 0 & 0 \\ 0 & -I_{zz} & 0 \\ 0 & 0 & 0 \end{bmatrix} \begin{bmatrix} \dot{V} \\ \dot{r} \\ \ddot{\phi} \end{bmatrix} + \begin{bmatrix} 0 & -mU & 0 \\ 0 & 0 & 0 \\ 0 & 0 & 0 \end{bmatrix} \begin{bmatrix} V \\ r \\ \dot{\phi} \end{bmatrix} + \begin{bmatrix} 0 & 0 & 0 \\ 0 & 0 & 0 \\ 0 & 0 & 0 \end{bmatrix} \begin{bmatrix} y \\ \psi \\ \phi \end{bmatrix} = \begin{bmatrix} 2 & 2 \\ 2l_f & -2l_r \\ 0 & 0 \end{bmatrix} \begin{bmatrix} F_f \\ F_r \end{bmatrix} \qquad \textbf{2.22}$$

with:

$$\begin{bmatrix} F_f \\ F_r \end{bmatrix} = \begin{bmatrix} -\frac{C_f}{U} & -\frac{l_f C_f}{U} & 0 \\ -\frac{C_r}{U} & \frac{l_r C_r}{U} & 0 \end{bmatrix} \begin{bmatrix} V \\ r \\ \phi \end{bmatrix} + \begin{bmatrix} C_f \\ 0 \end{bmatrix} \delta_f \qquad \textbf{2.23}$$

2.2 Derivation of Understeer Gradient

By definition, understeer gradient is simply a constant indicating the additional amount of steering versus the low-speed steering angle (measured per g of lateral acceleration) necessary to maintain a steady-state turn negotiated at increasingly larger velocities. It is measured in a steady state turning situation, and this acceleration typically comes from the centripetal acceleration acting upon a vehicle. An important result of the definition of understeer gradient is that it relates two parameters that are difficult to measure (C_f and C_r) to two parameters that are relatively easy to measure (W_{front} and W_{rear}). By solving for the understeer gradient, it will provide certain guidelines in the selection of values for cornering stiffness – a fact that will be of great importance in Chapter 5.

Additionally, understeer gradient provides a basic understanding of the vehicle's behavior. Generally speaking, if K_{us} is greater than 0, the vehicle is characterized as understeer and tends to resist a driver's efforts to make a turn as velocity increases. Likewise, if K_{us} is less than zero, the vehicle is characterized as oversteer and requires less steering to make a given turn as speed increases. Nearly all production vehicles are designed to be understeer due to safety concerns. For additional information, refer to Gillespie's book on Vehicle Dynamics [11], as further discussion is beyond the scope of this work.

In the development of the understeer gradient equation, a vehicle undergoing low speed turning will first be examined. As a vehicle's velocity approaches zero, the lateral

acceleration also approaches zero. Using the "single track" concept developed previously, the vehicle may be viewed as shown in Figure 2.5.

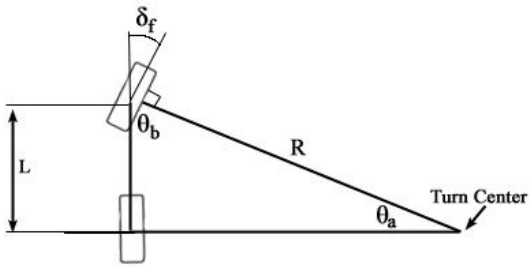

Figure 2.5: Single Track Vehicle Under Low-Speed, Steady State Turning

From geometry, we see that:

$$\pi = \delta_f + \theta_b + \frac{\pi}{2} \qquad 2.24$$

and:

$$\theta_a + \theta_b = \frac{\pi}{2} \qquad 2.25$$

Expressing Eq. 2.24 as:

$$\theta_b = \frac{\pi}{2} - \delta_f \qquad 2.26$$

and substituting Eq. 2.26 into Eq. 2.25 it may be seen that:

$$\delta_f = \theta_a \qquad 2.27$$

But since:

$$\theta_a \approx \sin\left(\frac{L}{R}\right) \approx \frac{L}{R} \qquad 2.28$$

then by the above assumptions the steering angle of the vehicle may be expressed as:

$$\delta_f = \frac{L}{R} \qquad \textbf{2.29}$$

This is the expression for low speed steering angle required to negotiate a turn of fixed radius.

When vehicle speed increases, the model presented in Figure **2.5** needs to be modified to include the side-slip of the tires. Shown below in Figure **2.6**, the single-track vehicle under high-speed steady state turning closely resembles the free-body diagram of the 2DOF model developed above. A summation of angles of the interior triangle formed by the turning center and the front and rear wheels gives:

$$\frac{\pi}{2} + \alpha_f - \delta_f + \frac{\pi}{2} - \alpha_r + \frac{L}{R} = \pi \qquad \textbf{2.30}$$

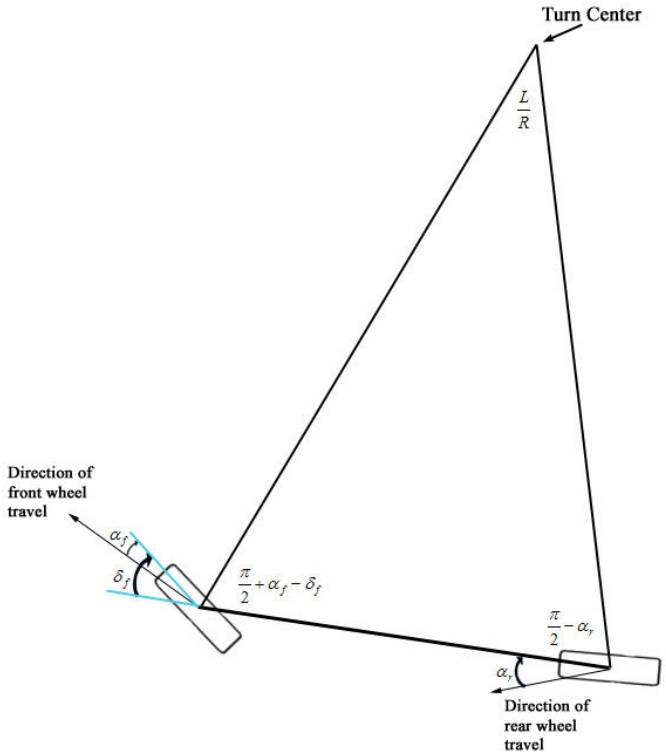

Figure **2.6**: Single Track Vehicle Under High-Speed, Steady State Turning

Solving for the steering angle results in:

$$\delta_f = \frac{L}{R} + \alpha_f - \alpha_r \qquad \textbf{2.31}$$

Following the assumption of a linear relationship between tire force generation and side-slip angle, α_f and α_r may be substituted with:

$$\alpha_f = \frac{F_f}{C_f} \qquad \textbf{2.32}$$

and:

$$\alpha_r = \frac{F_r}{C_r} \qquad \textbf{2.33}$$

which gives:

$$\delta_f = \frac{L}{R} + \left(\frac{2 \cdot F_f}{C_f} - \frac{2 \cdot F_r}{C_r} \right) \qquad \textbf{2.34}$$

Recalling that understeer gradient is the relationship between increasing steering angle required to go around a turn per g of lateral acceleration, a linear relationship needs to be established that expresses $\left(2 \cdot F_f \cdot C_f^{-1} - 2 \cdot F_r \cdot C_r^{-1}\right)$ in terms of lateral acceleration and vehicle parameters. In order to accomplish this, a proportional relationship will first be developed between the front and rear tire forces. Summation of moments about the vertical axis at the CG gives, for steady-state turning:

$$\sum M_{z,CG} = 2 \cdot \left(F_r \cdot l_r - F_f \cdot l_f\right) = 0 \qquad \textbf{2.35}$$

which provides the relationship:

$$F_f = \frac{l_r}{l_f} F_r \qquad \textbf{2.36}$$

Summing forces in the lateral direction results in:

$$\sum F_y = -2 \cdot F_f - 2 \cdot F_r = F_{centripital} = \frac{m \cdot U^2}{R} \qquad \textbf{2.37}$$

Substituting Eq. **2.36** into Eq. **2.37** and solving for F_r gives:

$$2 \cdot \frac{l_r}{l_f} \cdot F_r + 2 \cdot F_r = 2 \cdot F_r \cdot \left(\frac{l_r}{l_f} + 1 \right) = -\frac{m \cdot U^2}{R} \qquad \textbf{2.38}$$

$$F_r = -\frac{1}{2 \cdot \left(\frac{l_r}{l_f} + 1 \right)} \cdot \frac{m \cdot U^2}{R} = -\frac{l_f}{2 \cdot (l_r + l_f)} \cdot \frac{m \cdot U^2}{R} = -\frac{l_f \cdot m \cdot U^2}{2 \cdot L \cdot R} \qquad \textbf{2.39}$$

Similarly Eq. **2.35** may be solved for F_r and substituted into Eq. **2.37**:

$$F_r = \frac{l_f}{l_r} F_f \qquad \textbf{2.40}$$

$$F_f = -\frac{l_r \cdot m \cdot U^2}{2 \cdot L \cdot R} \qquad \textbf{2.41}$$

Now that the forces have been expressed in terms of the vehicle parameters and lateral acceleration, they may be substituted into Eq. **2.34**:

$$\delta_f = \frac{L}{R} + \left(\frac{2 \cdot F_f}{C_f} - \frac{2 \cdot F_r}{C_r} \right) = \frac{L}{R} + \left(\frac{l_f \cdot m \cdot U^2}{2 \cdot L \cdot R \cdot C_r} - \frac{l_r \cdot m \cdot U^2}{2 \cdot L \cdot R \cdot C_f} \right) \qquad \textbf{2.42}$$

Factorization results in:

$$\delta_f = \frac{L}{R} + \left(\frac{l_f \cdot m}{2 \cdot C_r \cdot L} - \frac{l_r \cdot m}{2 \cdot C_f \cdot L} \right) \cdot \frac{U^2}{R} \qquad \textbf{2.43}$$

From proportionality, the distance from the front axle to the CG, l_f, may be defined by:

$$l_f = \left(1 - \frac{W_{front}}{W_{car}}\right) \cdot L \qquad \textbf{2.44}$$

Using this relationship, the weight on the front axle of the vehicle may be expressed as:

$$W_{front} = W_{car} \frac{l_r}{L} = g \frac{l_r \cdot m}{L} \qquad \textbf{2.45}$$

The weight on the rear axle may be similarly expressed as:

$$W_{rear} = W_{car} \frac{l_f}{L} = g \frac{l_f \cdot m}{L} \qquad \textbf{2.46}$$

Substitution of Eq. **2.45** and Eq. **2.46** into Eq. **2.43** results in:

$$\delta_f = \frac{L}{R} + \left(\frac{W_r}{2 \cdot C_f} - \frac{W_f}{2 \cdot C_r}\right) \frac{U^2}{g \cdot R} \qquad \textbf{2.47}$$

From this it is seen that L/R is the steering angle required to make the turn at low speed, $U^2 \cdot (g \cdot R)^{-1}$ is the lateral acceleration, $a_{y,global}$, of the vehicle measured in g's, and the proportionality constant:

$$K_{us} = \frac{W_r}{2 \cdot C_f} - \frac{W_f}{2 \cdot C_r} \qquad \textbf{2.48}$$

is the understeer gradient of the vehicle and has units of rad/g. Applying these simplifications gives the final equation for the steering angle of a vehicle under high-speed steady-state turning conditions to be:

$$\delta_f = \frac{L}{R} + K_{us} \cdot a_{y,global} \qquad \textbf{2.49}$$

2.3 Conclusion

This chapter presented a simple two-degree-of-freedom model which will be used to provide a baseline comparison to the planar dynamics of the more complex models that include roll descriptions. Many of the models that will be discussed in this work follow the same simplifying assumptions as the bicycle model and should therefore mimic its behavior to a large extent in regards to both lateral velocity and yaw motion.

The form of the equations that will be used to represent all models discussed in this work was also presented. This form will allow for the most apparent comparison between the effects that different modeling assumptions have on the resulting equations of motion.

[1] S. Saraf and M. Tomizuka, "Slip Angle Estimation for Vehicles on Automated Highways," presented at Proceedings of the 1997 American Control Conference, Albuquerque, New Mexico, 1997.

[2] D. M. Bevly, R. Sheridan, and J. C. Gerdes, "Integrating INS Sensors with GPS Velocity Measurements for Continuous Estimation of Vehicle Sideslip and Tire Cornering Stiffness," presented at Proceedings of the 2001 American Control Conference, Arlington, Virginia, 2001.

[3] J. Ackermann, W. Sienel, and R. Steinhauser, "Robust automatic steering of a bus," presented at Proceedings of the Second European Control Conference (ECC), Groningen, The Netherlands, 1993.

[4] S. Mammar and V. B. Baghdassarian, "Two-degree-of-freedom Formulation of Vehicle Handling Improvement by Active Steering," presented at Proceedings of the 2000 American Control Conference, Chicago, Illinois, 2000.

[5] S.-S. You and S.-K. Jeong, "Controller design and analysis for automatic steering of passenger cars," *Mechatronics*, vol. 12, pp. 427--446, 2002.

[6] K. A. Unyelioglu, C. Hatipoglu, and U. Ozguner, "Design and stability analysis of a lane following controller," *IEEE Transactions on Control Systems Technology*, vol. 5, pp. 127--134, 1997.

[7] M. Shino, Y. Wang, and M. Nagai, "Motion Control of Electric Vehicles Considering Vehicle Stability," presented at Proceedings of the 5th International Symposium on Advanced Vehicle Control (AVEC), Ann Arbor, Michigan, 2000.

[8] U. Kiencke, Nielsen, L., *Automotive Control Systems for Engine, Driveline, and Vehicle*, 1st ed. New York: Springer, 2000.

[9] "Surface Vehicle Recommended Practice," Society of Automotive Engineers J670e, July 1976.
[10] J. H. Ginsberg, *Advanced Engineering Dynamics*, 2nd ed. New York, NY: Cambridge University Press, 1998.
[11] T. D. Gillespie, *Fundamentals of Vehicle Dynamics*: Society of Automotive Engineers (SAE), 1992.

Chapter 3

Roll Model Derivations

This chapter contains detailed derivations of several roll models chosen for evaluation in this study. While many more models are available, the purpose of this study is to compare a representative selection from literature spanning both models evaluated purely in simulation and those that were implemented experimentally. Experimentally validated models are especially important in order to gain a better understanding for what assumptions are appropriate and what degree of model complexity is required to obtain an accurate representation of a vehicle's dynamics as they undergo longitudinal, lateral and roll motions.

3.1 General Comments on Roll Models

An extensive, but not exhaustive, search of recent literature found twenty-three unique vehicle models that included a full mathematical description of roll dynamics. Of these, only three will be utilized in this study [1-3]. The reasoning used to narrow down the number of models under consideration is discussed below.

It is noted that many publications include models that dealt with trailer dynamics [4, 5], only examined suspension dynamics and ignored longitudinal and lateral motion [6], sought to only investigate the effect of lateral acceleration on vehicle rollover [7],

simply estimated roll with a correcting term [8, 9], or dealt with tripped rollovers [10, 11]. For these reasons, these models are not used in this thesis.

Another significant portion of the models found were discounted because there was simply not enough information given in the paper to recreate the simulations or derivations. For instance, [12-15] did not provide the equations of motion used for reported simulations and experimental comparisons. Others simply did not define all of the symbols used in their model [16] or provide sufficient detail to recreate equation derivations [17].

Additional factors narrowing model selection included the use of an overly complex model unsuitable for control synthesis. These include models derived from kinematic software packages that generate equations of motion that are so complex and high order that they are unsuitable for feedback control design [18, 19]. Other models included parameters that were either difficult to measure, or required input/output time-response data to obtain parameters whose physical meaning is unclear [20, 21]. Because the goal of this study is to develop models based on first-principles without the need for dynamic fitting, these models were abandoned.

Finally there was the category of models that, although the equations of motion were presented, a number of errors existed such that they were not reproducible in simulation [22-24]. In the case of [22, 23], the same model was presented in state-space form [23] and in transfer function form [22]. However, parameters were different between the two papers, with neither set seeming to match published results. The state-space representation proved to be open-loop unstable.

For these reasons, our study will focus on models based upon those derived in [1-3]. These three models still require information obtained only through experimental measurement [2], but the physical meaning of these parameters is clear and therefore allows offline estimation of these parameters.

3.2 General Comments on Roll Model Derivations

To emphasize the similarity between all of the models used in this study, each is presented and derived in similar fashion using similar state definitions and coordinate systems. All numerical representations follow the standard SAE right-handed sign convention shown in Figure **3.1**. In some cases, this sign convention differs from the original publications.

Also, in order to avoid confusion, each model will be derived to conform to the common notation described by Figure **3.2** and Table **3.1**. Any changes from the original published work will be indicated. All models are linear and are therefore subject to the same assumptions as the bicycle model unless otherwise specified, with the most obvious exception being that roll dynamics are considered.

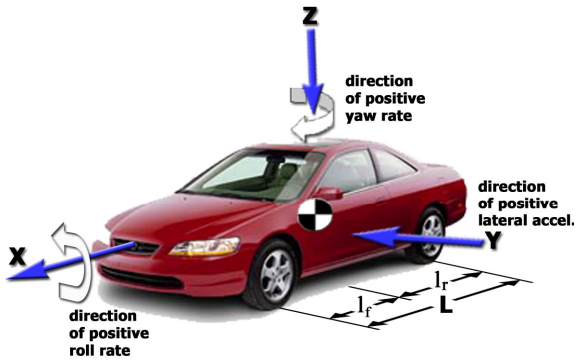

Figure **3.1**: Standard SAE Vehicle Coordinate System

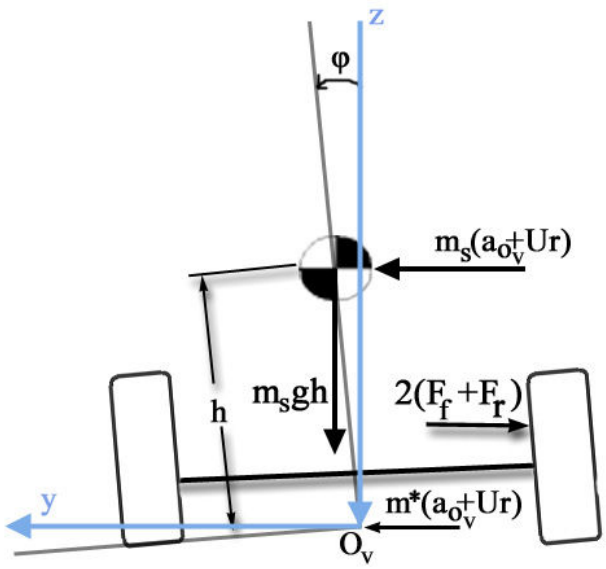

Figure **3.2**: Roll Angle Definition for 3DOF Vehicle Models (Front View)

Table 3.1: General Simulation Parameters and Notation Definitions

Variable	Value	Units	Uncertainty	How it was determined
m	1030	kg	5%	Measured
W_f	6339	N	5%	Measured
W_r	3781	N	5%	Measured
m_s	825	kg	5%	Model Fit[2]
I_{zz}	1850	kg-m^2	5%	Model Fit[1]
I_{yy}	1705	kg-m^2	5%	NHTSA database
I_{xx}	375	kg-m^2	5%	NHTSA database
I_{xz}	72	kg-m^2	5%	NHTSA database
l_f	0.93	m	5%	Measured[1]
l_r	1.56	m	5%	Measured[1]
l	1.4	m	5%	Measured1
h	0.52	m	5%	NHTSA database
K_φ	53000	N*m/rad	10%	Model Fit[2]
D_φ	6000	N*m*s/rad^2	10%	Model Fit[2]
C_f	-45500	N/rad	10%	Model Fit[2]
C_r	-76650	N/rad	10%	Model Fit[2]
K_{us}	0.045	rad/g	5%	Experimentally Determined

[1] - Indicates that the value is within 5% of the NHTSA database value.
[2] - Indicates that the value is not published in a readily available public database.

The values in Table 3.1 correspond to an instrumented 1992 5-door Mercury Tracer that was used for vehicle testing. Note that, in Table 3.1, where "model fit" is indicated as the method of determination it is referring to previous model validation experiments performed on the vehicle. These model fits are described in detail in Chapter 5 and the resulting best-fit parameters are presented in Table 3.1. All uncertainty bounds indicated are estimates.

3.3 Model Assuming Existence of Sprung Mass and No X-Z Planar Symmetry

The following model derivation is consistent with the work presented by Mammar et. al. [3]. The model presented here will differ in that the vehicle equations are derived in a body-fixed frame instead of being referenced to a global frame. It will also conform to the standard SAE coordinate system defined above in Figure 3.1 and Figure 3.2 as

opposed to that which was used in the original publication. This model will be designated as Model 2 (the bicycle model is denoted as Model 1).

Nonlinear moment equations may be derived from basic kinematics by considering the contribution of inertial forces combined with the motion of the CG about the origin O_v. Since the origin of the coordinate system is not fixed to the CG, the equations of motion must be expressed as [25]:

$$\sum M_{o_V} = m_s \cdot h \times a_{O_V} + \dot{H}_{O_V} \qquad \textbf{3.1}$$

where a_{O_V} is the acceleration at the origin and H_{O_V} is the angular momentum of the body about the origin. Eq. **3.1** clearly shows the coupled effects of linear and angular motion on the resulting moment acting on a body.

The first step necessary to solve Eq. **3.1** is to derive the relationship between the physical properties of the vehicle and the change in angular momentum. This begins by defining the angular momentum to be:

$$H_{O_V} = [I] \cdot [\omega] \qquad \textbf{3.2}$$

where $[I]$ is the inertia matrix:

$$[I] = \begin{bmatrix} I_{xx} & -I_{xy} & -I_{xz} \\ -I_{xy} & I_{yy} & -I_{yz} \\ -I_{xz} & -I_{yz} & I_{zz} \end{bmatrix} \qquad \textbf{3.3}$$

and ω is the angular velocity vector:

$$[\omega] = \begin{bmatrix} \omega_x \\ \omega_y \\ \omega_z \end{bmatrix} \qquad \textbf{3.4}$$

with ω_x, ω_y, and ω_z being the components of the vehicle's angular velocity about the body-fixed coordinate axes. Since the axes are body-fixed, then the inertial properties of the vehicle are constant. Therefore the time derivative of Eq. **3.2** is:

$$\dot{H}_{O_v} = \frac{\partial H_{O_v}}{\partial t} + [\omega] \times H_{O_v} = [I] \cdot [\alpha] + \begin{bmatrix} 0 & -\omega_z & \omega_y \\ \omega_z & 0 & -\omega_x \\ -\omega_y & \omega_x & 0 \end{bmatrix} \cdot [I] \cdot [\omega] \qquad \textbf{3.5}$$

where α is the angular acceleration of the vehicle about the body-fixed coordinate axes.

Since I_{xy} and I_{yz} are assumed to be zero, Eq. **3.3** may be expressed as:

$$[I_2] = \begin{bmatrix} I_{xx} & 0 & -I_{xz} \\ 0 & I_{yy} & 0 \\ -I_{xz} & 0 & I_{zz} \end{bmatrix} \qquad \textbf{3.6}$$

Additionally, examination of the free body diagram shown in Figure **3.2** gives $[\omega]$ to be:

$$[\omega] = \begin{bmatrix} \omega_x \\ \omega_y \\ \omega_z \end{bmatrix} = \begin{bmatrix} \dot{\phi} \\ -\dot{\psi}\sin(\phi) \\ -\dot{\psi}\cos(\phi) \end{bmatrix} \qquad \textbf{3.7}$$

Taking the time derivative of Eq. **3.7** defines $[\alpha]$ to be:

$$[\alpha] = \begin{bmatrix} \alpha_x \\ \alpha_y \\ \alpha_z \end{bmatrix} = \begin{bmatrix} \ddot{\phi} \\ -\ddot{\psi}\sin(\phi) - \dot{\psi}\cos(\phi)\dot{\phi} \\ -\ddot{\psi}\cos(\phi) + \dot{\psi}\sin(\phi)\dot{\phi} \end{bmatrix} \qquad \textbf{3.8}$$

which allows the vehicle's time rate of change of angular momentum to be solved for. More explicit details on the development of Eq. **3.5** may be found in Ginsberg's book on pages 166 – 191 [25].

It is now necessary to define the linear acceleration of the body so that Eq. **3.1** may be completely solved. For a body following a given path, there exists a component

of acceleration normal to the path and a component tangential to it. Thus a_{O_Y} may be defined as [26]:

$$a_{O_Y} = a_{O_Y,n} + a_{O_Y,t} \tag{3.9}$$

where the normal component is defined as:

$$a_{O_Y,n} = [\omega] \cdot U \tag{3.10}$$

and the tangential component is defined as:

$$a_{O_Y,t} = [\alpha] \cdot h \tag{3.11}$$

By substituting Eq. **3.9** and Eq. **3.5** into Eq. **3.1** and evaluating, the total moment acting about the three body-fixed coordinate axes may the found.

Lateral forces are summed as they were in Chapter 2, with the addition of the lateral acceleration components induced by the roll motion of the vehicle. By recognizing that the moment about the y-axis is zero by the assumption that the vehicle does not undergo pitch motion, the non-linear equations of motion are:

$$\begin{bmatrix} \sum F_y \\ \sum M_z \\ \sum M_x \end{bmatrix} = \begin{bmatrix} -m \cdot U \cdot \varpi \cdot c(\beta) - m_s \cdot h \cdot \dot{\psi}^2 \cdot s(\phi) + m_s \cdot h\left(\dot{\phi}^2 \cdot s(\phi) - \ddot{\phi} \cdot c(\phi)\right) \\ -I_{zz} \cdot \ddot{\psi} \cdot c(\phi) - I_{xz} \cdot \ddot{\phi} + I_{\gamma 1} \cdot \dot{\phi} \cdot \dot{\psi} \cdot s(\phi) + I_{xz} \cdot \dot{\psi}^2 \cdot s(\phi) \cdot c(\phi) \\ I_{xx} \cdot \ddot{\phi} + I_{xz} \cdot \ddot{\psi} + I_{\gamma 2} \cdot \dot{\psi}^2 \cdot s(\phi) \cdot c(\phi) + m_s \cdot h \cdot U \cdot \varpi \cdot c(\beta) \cdot c(\phi) + m \cdot h^2 \cdot \dot{\psi}^2 \cdot c^2(\phi) \end{bmatrix} \tag{3.12}$$

where:

$$I_{\gamma 1} = \left(I_{zz} + I_{xx} - I_{yy}\right) \tag{3.13}$$

$$I_{\gamma 2} = \left(I_{zz} - I_{yy}\right) \tag{3.14}$$

$$\varpi = \left(\dot{\beta} + \dot{\psi}\right) \tag{3.15}$$

$$c(x) = \cos(x),\ s(x) = \sin(x) \tag{3.16}$$

Utilizing the force equations derived in Section **2.1** defined by:

$$F_f = C_f \alpha_f = C_f\left(\delta_f - \beta - \frac{l_f}{U} r\right) \tag{3.17}$$

$$F_r = C_r \alpha_r = C_r\left(-\beta + \frac{l_r}{U} r\right) \tag{3.18}$$

and body-slip to be defined as in Eq. **2.6**:

$$\beta = \frac{V}{U} \tag{3.19}$$

gives the expression for lateral tire force. Note that due to the assumption that the vehicle is moving at constant speed and that there is no slip in the longitudinal direction, the longitudinal forces acting upon the tires are assumed to be zero. From these, it is seen that the external forces acting on the vehicle are:

$$\begin{bmatrix} \sum F_y \\ \sum M_z \\ \sum M_x \end{bmatrix} = \begin{bmatrix} 2F_f + 2F_r \\ 2l_f F_f - 2l_r F_r \\ -\left(K_\phi \phi + D_\phi \dot{\phi}\right) + m_s g h \phi \end{bmatrix} \tag{3.20}$$

where K_φ and D_φ are the roll stiffness and roll damping constants, respectively.

By equating the internal and external force-moment equations, combined with a small angle assumption and neglecting all higher order terms, the equations of motion may be placed in the compact notation presented in Eq. **2.20**, which is the linear equation

$$M\ddot{q} + D\dot{q} + Kq = Fu_f \tag{3.21}$$

This expands to:

$$\begin{bmatrix} -m & 0 & -m_s h \\ 0 & -I_{zz} & -I_{xz} \\ m_s h & I_{xz} & I_{xx} \end{bmatrix} \begin{bmatrix} \dot{V} \\ \dot{r} \\ \ddot{\phi} \end{bmatrix} + \begin{bmatrix} 0 & -mU & 0 \\ 0 & 0 & 0 \\ 0 & m_s hU & D_\phi \end{bmatrix} \begin{bmatrix} V \\ r \\ \dot{\phi} \end{bmatrix} + \begin{bmatrix} 0 & 0 & 0 \\ 0 & 0 & 0 \\ 0 & 0 & K_\phi - m_s gh \end{bmatrix} \begin{bmatrix} y \\ \psi \\ \phi \end{bmatrix} = \begin{bmatrix} 2 & 2 \\ 2l_f & 2l_r \\ 0 & 0 \end{bmatrix} \begin{bmatrix} F_f \\ F_r \end{bmatrix} \tag{3.22}$$

where:

$$\begin{bmatrix} F_{f,2} \\ F_{r,2} \end{bmatrix} = \begin{bmatrix} -\frac{C_f}{U} & -\frac{l_f C_f}{U} & 0 \\ -\frac{C_r}{U} & \frac{l_r C_r}{U} & 0 \end{bmatrix} \begin{bmatrix} V \\ r \\ \phi \end{bmatrix} + \begin{bmatrix} C_f \\ 0 \end{bmatrix} \delta_f \tag{3.23}$$

From here, Eq. **3.22** may be rewritten into the standard state-space representation following some manipulation of terms. The corresponding equations are presented in Appendix **A.1**.

While the derivation presented by Mammar [27] is very thorough and logical, the parameters given in the same reference appear unrealistic. Most notably in error are the values for front and rear cornering stiffness which are not only an order of magnitude lower than those obtained experimentally in this work, but are reported to be identical for the front and rear tires. This assumption is quite poor as there are virtually no reported cornering stiffness values from experimental tests that possess this characteristic.

3.4 Model Assuming Existence of Sprung Mass, X-Z Planar Symmetry, and Roll Steer Influence

Following the coordinate system specified by Figure 3.1, Kim and Park present a 3DOF model that describes the vehicle's lateral velocity, yaw rate, and roll angle [2]. The derivation presented here differs from the original work in that each tire is taken individually in this work so that the cornering stiffness defined above may be used. The sign of the cornering stiffness values also differ, and some of the notation was changed to coincide with that used in this work. This model will be designated as Model 3.

This derivation is similar to that which was presented in Section 3.3 with the exception that I_{xz} is set to zero. This follows from the assumption that the vehicle's mass is symmetric about the x-z plane. This simplification defines the inertia matrix used in Eq. 3.5 to be:

$$[I_3] = \begin{bmatrix} I_{xx} & 0 & 0 \\ 0 & I_{yy} & 0 \\ 0 & 0 & I_{zz} \end{bmatrix} \tag{3.24}$$

Following this modification, the nonlinear equations of motion become:

$$\begin{bmatrix} \sum F_y \\ \sum M_z \\ \sum M_x \end{bmatrix} = \begin{bmatrix} -m \cdot U \cdot \varpi \cdot c(\beta) - m_s \cdot h \cdot \dot{\psi}^2 \cdot s(\phi) + m_s \cdot h \cdot \left(\dot{\phi}^2 \cdot s(\phi) - \ddot{\phi} \cdot c(\phi) \right) \\ -I_{zz} \cdot \ddot{\psi} \cdot c(\phi) + I_{\gamma 1} \cdot \dot{\phi} \cdot \dot{\psi} \cdot s(\phi) \\ I_{xx} \cdot \ddot{\phi} + I_{\gamma 2} \cdot \dot{\psi}^2 \cdot s(\phi) \cdot c(\phi) + m_s \cdot h \cdot U \cdot \varpi \cdot c(\beta) \cdot c(\phi) + m \cdot h^2 \cdot \dot{\psi}^2 \cdot c^2(\phi) \end{bmatrix} \tag{3.25}$$

with the summation of the external forces acting upon the vehicle being defined by:

$$\begin{bmatrix} \sum F_y \\ \sum M_z \\ \sum M_x \end{bmatrix} = \begin{bmatrix} 2F_f + 2F_r \\ 2l_f F_f - 2l_r F_r \\ -\left(K_\phi \phi + D_\phi \dot{\phi} \right) + m_s g h \phi \end{bmatrix} \tag{3.26}$$

By again applying a small angle assumption and neglecting higher order terms, the equations of motion may be represented in the form described by Eq. **3.21** as:

$$\begin{bmatrix} -m & 0 & m_s h \\ 0 & -I_{zz} & 0 \\ -m_s h & 0 & I_{xx} \end{bmatrix} \begin{bmatrix} \dot{V} \\ \dot{r} \\ \ddot{\phi} \end{bmatrix} + \begin{bmatrix} 0 & -mU & 0 \\ 0 & 0 & 0 \\ 0 & -m_s hU & D_\phi \end{bmatrix} \begin{bmatrix} V \\ r \\ \dot{\phi} \end{bmatrix} + \begin{bmatrix} 0 & 0 & 0 \\ 0 & 0 & 0 \\ 0 & 0 & K_\phi - m_s gh \end{bmatrix} \begin{bmatrix} y \\ \psi \\ \phi \end{bmatrix} = \begin{bmatrix} 2 & 2 \\ 2l_f & -2l_r \\ 0 & 0 \end{bmatrix} \begin{bmatrix} F_f \\ F_r \end{bmatrix} \quad \textbf{3.27}$$

with the external forces being redefined as:

$$\begin{bmatrix} F_{f,3} \\ F_{r,3} \end{bmatrix} = \begin{bmatrix} -\frac{C_f}{U} & -\frac{l_f C_f}{U} & \frac{\partial \alpha_f^*}{\partial \phi} \\ -\frac{C_r}{U} & \frac{l_r C_r}{U} & \frac{\partial \alpha_r^*}{\partial \phi} \end{bmatrix} \begin{bmatrix} V \\ r \\ \phi \end{bmatrix} + \begin{bmatrix} C_f \\ 0 \end{bmatrix} \delta_f \quad \textbf{3.28}$$

Note the appearance of a partial derivative term in Eq. **3.28**. The star is placed in these terms to indicate that they refer to the influence of the vehicle's roll angle on the slip angle of the vehicle. This effect is commonly known as "roll steer" and is merely a constant value. The value suggested by the authors in [2] for this coefficient for the front tires was 0.2 and -0.2 for the rear tires.

A subtle change was made in the roll moment term in the stiffness matrix K between the derivation presented here and the version published by Kim and Park [2]. The original authors presented the term in the lower-right hand corner to simply be K_φ, with the gravitational effect on the sprung mass seemingly ignored. However, it is included here as it is believed by the author that the additional moment term, $-m_s gh$, is simply included in the definition of roll stiffness in the original work. This is reasoned by considering its appearance in a moment balance, as well as its magnitude being approximately 12% of the roll stiffness (see values in Table **3.1**). Therefore, it is unlikely that Kim and Park excluded this term from their derivation but rather included it in their definition of roll stiffness.

As with the previous model, the equations of motion may be represented in state-space form with the equations appearing in Appendix A.2.

3.5 Model Assuming Sprung Mass Suspended on a Massless Frame, X-Z Planar Symmetry, and No Yaw Influence on Roll

The next model presented is based on the model derived by Carlson et. al. [1]. It will be changed to coincide with the SAE coordinate system defined above in Figure 3.1 and Figure 3.2. Additionally, the notation will be changed from the original publication to coincide with the one used in this work and longitudinal tire forces will not be considered by the assumptions listed in Section 3.3. This model will be designated as Model 4.

In order to solve for the moment summations in this model, Eq. 3.1 will be redefined as:

$$\sum M_{o_V} = m \cdot h \times a_{O_V} + \dot{H}_{O_V} \tag{3.29}$$

This definition is provided by the assumption that the sprung mass of the vehicle is supported by a massless frame, thus making $m_s = m$. These are combined to give the nonlinear equations of motion:

$$\begin{bmatrix} \sum F_y \\ \sum M_z \\ \sum M_x \end{bmatrix} = \begin{bmatrix} -m \cdot U \cdot \varpi \cdot c(\beta) - m \cdot h \cdot \dot{\psi}^2 \cdot s(\phi) + m \cdot h \cdot \left(\dot{\phi}^2 \cdot s(\phi) - \ddot{\phi} \cdot c(\phi)\right) \\ -I_{zz} \cdot \ddot{\psi} \cdot c(\phi) + I_{\gamma 1} \cdot \dot{\phi} \cdot \dot{\psi} \cdot s(\phi) \\ I_{xx} \cdot \ddot{\phi} + I_{\gamma 2} \cdot \dot{\psi}^2 \cdot s(\phi) \cdot c(\phi) + m \cdot h^2 \cdot \dot{\psi}^2 \cdot c^2(\phi) \end{bmatrix} \tag{3.30}$$

with the external forces acting on the vehicle defined by:

$$\begin{bmatrix} \sum F_y \\ \sum M_z \\ \sum M_x \end{bmatrix} = \begin{bmatrix} 2 \cdot F_f + 2 \cdot F_r \\ 2 \cdot l_f \cdot F_f - 2 \cdot l_r \cdot F_r \\ -\left(K_\phi \cdot \phi + D_\phi \cdot \dot{\phi}\right) + m_s \cdot g \cdot h \cdot \phi + 2 \cdot h \cdot F_f + 2 \cdot h \cdot F_r \end{bmatrix} \tag{3.31}$$

By again assuming small angles and neglecting higher order terms, we arrive at the linear equations:

$$\begin{bmatrix} -m & 0 & -mh \\ 0 & -I_{zz} & 0 \\ 0 & 0 & I_{xx} \end{bmatrix} \begin{bmatrix} \dot{V} \\ \dot{r} \\ \ddot{\phi} \end{bmatrix} + \begin{bmatrix} 0 & -mU & 0 \\ 0 & 0 & 0 \\ 0 & 0 & D_{\phi} \end{bmatrix} \begin{bmatrix} V \\ r \\ \dot{\phi} \end{bmatrix} + \begin{bmatrix} 0 & 0 & 0 \\ 0 & 0 & 0 \\ 0 & 0 & K_{\phi} - mgh \end{bmatrix} \begin{bmatrix} y \\ \psi \\ \phi \end{bmatrix} = \begin{bmatrix} 2 & 2 \\ 2l_f & -2l_r \\ 2h & 2h \end{bmatrix} \begin{bmatrix} F_f \\ F_r \end{bmatrix} \quad \textbf{3.32}$$

with the external forces being defined as they were in Eq. **3.23**. State-space equations for this model may be found in Appendix **A.3**.

3.6 Model Comparison – Qualitative Analysis

Examination of the equations of motion of all of the models in this study reveals the similarities between Model 1 and Models 2, 3, and 4. It is therefore reasonable to expect that the lateral acceleration and yaw rate dynamics of the four models will be similar as well.

Model 2 is the most complex roll model presented in this study. This complexity comes from the fact that the vehicle is assumed to be asymmetric about the x-z plane. When compared with Model 2, Models 3 and 4 have less cross-coupling of the acceleration terms as a result of the assumption of symmetry about the x-z plane.

The most apparent difference between Model 4 and Models 2 and 3 is that the total mass of the vehicle is assumed to be supported by the suspension, with the frame being assumed massless. This assumption causes Model 4 to be the simplest parametrically (i.e. requires the least number of parameters) when compared to Models 2 and 3.

Another distinguishing feature that simplifies the notation of Model 4 in the form described by Eq. **3.21** is that lateral acceleration of the vehicle that induces a roll moment on the vehicle, is replaced by the external forces acting on the tires. If this assumption had not been made, the term *mh* would appear in the lower left hand corner of the mass matrix and the term *mhU* would appear in the lower middle of the damping matrix. The force resulting from the lateral acceleration of the mass center may be equated to the external tire forces from a simple force balance when viewing the vehicle as an inverted pendulum. However, this is only valid under the assumption that the frame of the vehicle is massless. This is shown graphically in Figure **3.3**.

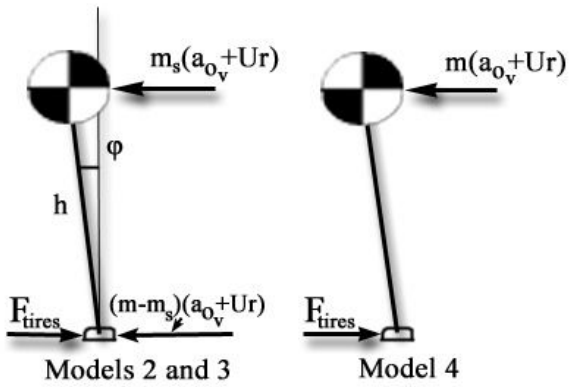

Figure **3.3**: Comparison of Lateral Forces Between Roll Models

While equating the forces in this manner is valid by Newtonian mechanics, it actually changes the plant dynamics and causes one of the system natural frequencies to be shifted by approximately 2.5 rad/s. To illustrate the effects that this assumption has on the plant dynamics of the model, Model 3 (Eq. **3.33**) will be directly compared to Model 4 (Eq. **3.34**), as they are largely similar.

$$\begin{bmatrix} -m & 0 & m_s h \\ 0 & -I_{zz} & 0 \\ -m_s h & 0 & I_{xx} \end{bmatrix}\begin{bmatrix} \dot{V} \\ \dot{r} \\ \ddot{\phi} \end{bmatrix}+\begin{bmatrix} 0 & -mU & 0 \\ 0 & 0 & 0 \\ 0 & -m_s hU & D_\phi \end{bmatrix}\begin{bmatrix} V \\ r \\ \dot{\phi} \end{bmatrix}+\begin{bmatrix} 0 & 0 & 0 \\ 0 & 0 & 0 \\ 0 & 0 & K_\phi - m_s gh \end{bmatrix}\begin{bmatrix} y \\ \psi \\ \phi \end{bmatrix}=\begin{bmatrix} 2 & 2 \\ 2l_f & -2l_r \\ 0 & 0 \end{bmatrix}\begin{bmatrix} F_f \\ F_r \end{bmatrix} \quad \textbf{3.33}$$

$$\begin{bmatrix} -m & 0 & -mh \\ 0 & -I_{zz} & 0 \\ 0 & 0 & I_{xx} \end{bmatrix}\begin{bmatrix} \dot{V} \\ \dot{r} \\ \ddot{\phi} \end{bmatrix}+\begin{bmatrix} 0 & -mU & 0 \\ 0 & 0 & 0 \\ 0 & 0 & D_\phi \end{bmatrix}\begin{bmatrix} V \\ r \\ \dot{\phi} \end{bmatrix}+\begin{bmatrix} 0 & 0 & 0 \\ 0 & 0 & 0 \\ 0 & 0 & K_\phi - mgh \end{bmatrix}\begin{bmatrix} y \\ \psi \\ \phi \end{bmatrix}=\begin{bmatrix} 2 & 2 \\ 2l_f & -2l_r \\ 2h & 2h \end{bmatrix}\begin{bmatrix} F_f \\ F_r \end{bmatrix} \quad \textbf{3.34}$$

In both Models 3 and 4, summing forces in the lateral direction results in:

$$\sum F_y = F_{tires} = m\left(a_{o_Y} + U \cdot r\right) \quad \textbf{3.35}$$

Since the frame in Model 4 is assumed to be massless, this equates the total forces acting at the CG to the total forces acting on the tires. From this equivalence, the roll moment induced by the acceleration terms in the roll dynamics of Model 4 may be replaced by a roll moment induced by the tire forces. The consequence of such a substitution is that the plant description changes, since this portion of the roll moment is now being expressed in the force inputs. Therefore, the eigenvalues of the plant are changed.

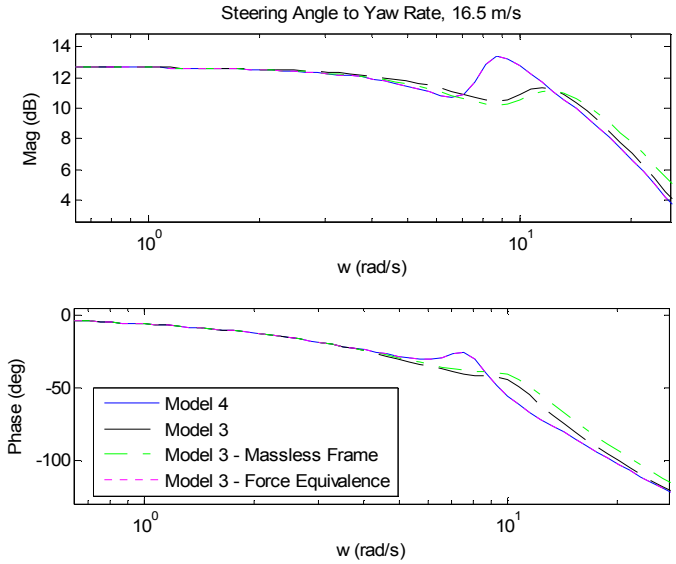

Figure **3.4**: Comparison Between Model 4 and Model 3 Under Varying Assumptions

This is shown explicitly in Figure 3.4, which shows the yaw rate response of the Tracer with modified suspension characteristics. The values for roll stiffness and damping were changed to 38,000 N-m/rad and 1050 N-m-s/rad, respectively, to highlight the effect of assumption on the dynamic response. It is shown that by simply making the assumption that the frame is massless causes very little change in Model 3. However, by equating the lateral tire forces with the total acceleration of the vehicle resulted in the natural frequency decreasing by 2.5 rad/s from the original model. This change also results in the overall damping of the model decreasing, with the resonant peak of Model 4 being approximately 2 dB greater than the original version of Model 3. It is clear that Model 4 and the final version of Model 3 match almost exactly in the yaw response.

3.7 Concluding Remarks

As stated previously, although a great number of vehicle models involving roll have been found in the literature, only a handful were found to be both easily reproducible and applicable to our study. Of those that were selected for further study, we can see that each of them produces unique results due to the various assumptions made during their derivations. Chapter 4 will discuss in detail the experimental validation of the equations presented here.

[1] C. R. Carlson and J. C. Gerdes, "Optimal Rollover Prevention with Steer-by-Wire and Differential Braking," presented at Proceedings of the 2003 ASME International Mechanical Engineering Congress and Exposition (IMECE), Washington D.C., 2003.

[2] H.-J. Kim and Y.-P. Park, "Investigation of robust roll motion control considering varying speed and actuator dynamics," *Mechatronics*, 2003.

[3] S. Mammar, "Speed Scheduled Vehicle Lateral Control," presented at Proceedings of the 1999 IEEE/IEEJ/JSAI International Conference on Intelligent Transportation Systems, 1999.

[4] D. Hyun, R. Langari, and J. Ochoa, "Vehicle Modeling and Prediction of Rollover Stability Threshold for Tractor-Semitrailers," presented at Proceedings of the 5th International Symposium on Advanced Vehicle Control (AVEC), Ann Arbor, Michigan, 2000.

[5] V. Krishnaswami, "A Regularization Approach to Robust Variable Structure Observer Design Applied to Vehicle Parameter and State Estimation," presented at Proceedings of the 1998 American Control Conference, Philadelphia, Pennsylvania, 1998.

[6] S. Ikenaga, F. L. Lewis, J. Campos, and L. Davis, "Active Suspension Control of Ground Vehicle based on a Full-Vehicle Model," presented at Proceedings of the 2000 American Control Conference, Chicago, Illinois, 2000.

[7] S. Kueperkoch, J. Ahmed, A. Kojic, and J.-P. Hathout, "Novel Vehice Stability Control Using Steer-By-Wire and Inedependent Four Wheel Torque Distribution," presented at Proceedings of the 2003 ASME International Mechanical Engineering Congress, Washington D.C., 2003.

[8] R. Fenton, G. Melocik, and K. Olson, "On the steering of automated vehicles: Theory and experiment," *IEEE Transactions on Automatic Control*, vol. 21, pp. 306--315, 1976.

[9] D. E. Williams and W. M. Haddad, "Nonlinear control of roll moment distribution to influence vehicle yaw characteristics," *IEEE Transactions on Control Systems Technology*, vol. 3, pp. 110-116, 1995.

[10] R. Eger, "Rollover Simulations Based on a Nonlinear Model," *Society of Automotive Engineers*, vol. 1321, pp. 1-7, 1998.

[11] R. Eger and U. Kiencke, "Modeling of rollover sequences," *Control Engineering Practice*, vol. 11, pp. 209-216, 2003.

[12] J. Darling and L. R. Hickson, "Experimental study of a prototype active anti-roll suspension system," *Vehicle System Dynamics*, vol. 29, pp. 309-329, 1998.

[13] S.-W. Oh, H.-C. Chae, S.-C. Yun, and C.-S. Han, "The Design of a Controller for the Steer-by-Wire System," *JSME International Journal, Series C*, vol. 47, pp. 896-907, 2004.

[14] N. Rosam and J. Darling, "Development and simulation of a novel roll control system for the Interconnected Hydragas(R) Suspension," *Vehicle System Dynamics*, vol. 27, pp. 1-18, 1997.

[15] T. J. Wielenga, "A Method For Reducing On-Road Rollovers Anti-Rollover Braking," vol. (none), (none), Ed., (none) ed. Detroit, Michigan: (none), 1999, pp. 87-98.

[16] W. Manning, D. Crolla, M. Brown, and M. Selby, "Coordination of Chassis Control Systems for Vehicle Motion Control," presented at Proceedings of the 5th International Symposium on Advanced Vehicle Control (AVEC), Ann Arbor, Michigan, 2000.

[17] K. Kitajima and H. Peng, "Control for Integrated Side-Slip, Roll, and Yaw Controls for Ground Vehicles," presented at Proceedings of the 5th International Symposium on Advanced Vehicle Control (AVEC), Ann Arbor, Michigan, 2000.

[18] D. J. Cole, "Evaluation of design alternatives for roll-control of road vehicles," presented at Proceedings of the 5th International Symposium on Advanced Vehicle Control (AVEC), Ann Arbor, Michigan, 2000.

[19] J. K. Sprague and S.-P. Liu, "Automated Stability Analysis of a Vehicle in Combined Pitch and Roll," presented at Proceedings of the 2002 ASME International Mechanical Engineering Congress and Exposition (IMECE), New Orleans, Louisiana, 2002.

[20] B.-C. Chen and H. Peng, "Differential Braking Based Rollover Prevention for Sport Utility Vehicles with HIL Evaluations," *Vehicle System Dynamics*, vol. 36, pp. 359-389, 2001.

[21] R. S. Sharp and D. Pan, "On the design of an active roll control system for a luxury car," *Proceedings of the Institution of Mechanical Engineers, Part D (Journal of Automobile Engineering)*, vol. 207, pp. 275-284, 1993.

[22] K. T. Feng, Han-ShueTan, and M. Tomizuka, "Decoupling Steering Control for Vehicles Using Dynamic Look-Ahead Scheme," presented at Proceedings of the 5th International Symposium on Advanced Vehicle Control (AVEC), Ann Arbor, Michigan, 2000.

[23] K.-T. Feng, H.-S. Tan, and M. Tomizuka, "Automatic Steering Control of Vehicle Lateral Motion with the Effect of Roll Dynamics," presented at Proceedings of the 1998 American Control Conference, Philadelphia, Pennsylvania, 1998.

[24] S. Takano, M. Nagai, T. Taniguchi, and T. Hatano, "Study on a vehicle dynamics model for improving roll stability," *Japanese Society of Automotive Engineers Review*, vol. 24, pp. 149-156, 2003.

[25] J. H. Ginsberg, *Advanced Engineering Dynamics*, 2nd ed. New York, NY: Cambridge University Press, 1998.

[26] R. C. Hibbeler, *Engineering Mechanics: Dynamics*, 8th ed. Upper Saddle River, NJ: Prentice - Hall, 1998.

[27] S. Mammar, V. B. Baghdassarian, and L. Nouveliere, "Speed Scheduled Vehicle Lateral Control," presented at Proceedings of the 1999 IEEE/IEEJ/JSAI International Conference on Intelligent Transportation Systems (Cat. No.99TH8383), 1999.

Chapter 4

Vehicle Instrumentation and Measurements

This chapter will present a detailed description of the vehicle's data acquisition system, sensors, and initial parametric measurements. The first section will provide an overview of the instrumentation and setup. An overview of the general architecture and system design will first be given, followed by a description of each sensor interfaced with the system. This will include the principle of operation for each sensor, sensor mounting, and calibration methods used. Performance issues for each sensor are also discussed.

The second section will discuss an alternate set up of the vehicle's instrumentation that was attempted in order to solve the shortcomings encountered with the current system. A comparison between the two configurations will be provided and conclusions drawn.

4.1 Vehicle Instrumentation and Setup

All of the equipment described below was used on the 1992 5-door Mercury Tracer test vehicle at the Pennsylvania Transportation Institute's (PTI) test track in State College, PA. It should be noted that the instrumentation is not vehicle specific and may be readily used for experimentation in any vehicle.

4.1.1 Data Acquisition System

Shown in red in Figure 4.1, the data acquisition system (DAQ) used in this study is based upon the Texas Instruments TMS320C6713 Digital Signal Processor (DSP) Developers Kit. The kit includes a circuit board with a C6713 class DSP that includes address and data-bus headers that allow easy interfacing with the processor. Custom daughter cards developed by Dan Block at the Control Systems Instructional Laboratory at the University of Illinois at Urbana-Champaign are interfaced with the DSK to provide the following capabilities:

- 8 Digital I/O's
- 4 Analog I/O's, -10/+10 volt range
- 2 RS-232 (Serial) Ports
- I2C Data Bus (6 ports)

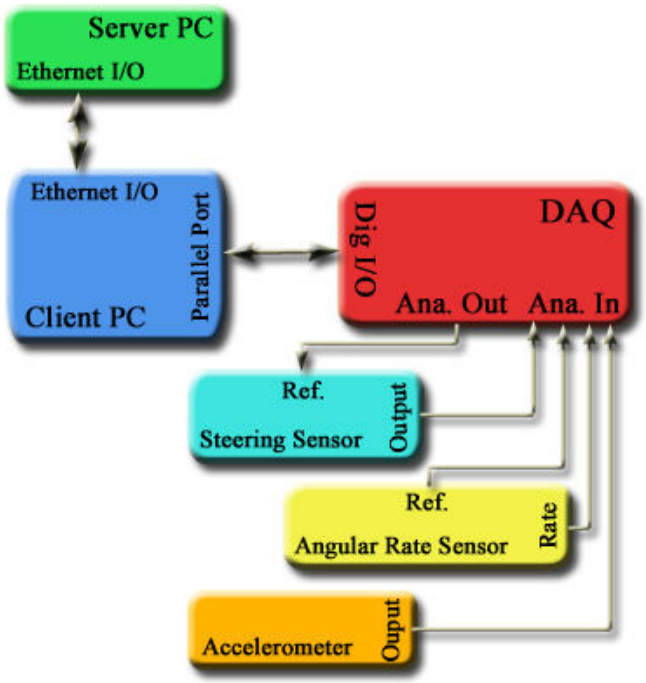

Figure 4.1: Data Acquisition and Sensing Architecture

The device drivers included with the kit allow the board to be programmed in standard C-code through the programming environment known as Code Composer Studio (CCS) developed by Texas Instruments. Using this software, the DSP was set up to continuously poll for requested data while simultaneously reading the sensors. Tests have shown that data from all of the sensors may be sampled at rates exceeding 1000 samples per second, though for this study a sample rate of 200Hz was used, since the highest input frequency sampled was approximately 5Hz. Such a sampling rate avoids aliasing, provides high fidelity data, and reduces disk file size significantly.

The digital I/O lines were set up in such a manner as to allow simple yet efficient communication between the acquisition hardware and the host computer via the parallel port. The client PC, colored blue in Figure **4.1**, has a 400 Mhz Pentium® III processor and runs the Wincon® software package developed by Quanser Consulting. This software provides a real-time kernel to run "underneath" the resident Windows operating system to ensure that data is both requested and collected from the associated hardware at the required intervals with only microsecond latency. Such software is required for this task to ensure that the flow of data is not preempted by the operating system – a critical factor in the control architecture of a motor vehicle.

Data is then communicated to the server (coded green) through an Ethernet line using standard TCP/IP protocol where it is recorded and plotted in real-time. Although this is currently accomplished via a physical connection between the client and server, future work beyond this study is considering the use of wireless Ethernet protocols to simultaneously send commands to, and collect data from, the vehicle without actually being inside of it.

The sensor interface is accomplished graphically on the server using the MATLAB® SIMULINK® environment. One shortcoming of the Wincon® kernel is that it is not readily made to interface with custom hardware such as what was used in this study. Therefore, with the help of Dan Block, custom device drivers were developed that interfaced the Client and the DAQ through the parallel port. Communication between the Server and the Client is handled by Wincon® and is a built-in feature of this software.

One major advantage of this setup is that not only can the data be read in real-time, but any calibration functions, controller gains, etc. may be tuned in real-time. This feature allows for the quick verification and adjustment of calibration functions prior to performing vehicle tests. Similar capability on more widely used commercial software (dSpace, for example) would easily cost roughly an order-of-magnitude more than that of the current system setup.

4.1.2 Steering Angle Sensors

A requirement for all of the sensors was that they had to be failsafe against a power failure. This implies that on power-up, the DAQ must be able to report accurate measurements from the sensors without the need to return any part of the vehicle to a "home" position. As a result it was decided that linear string potentiometers would be used to measure the steering angle of the vehicle. Not only do these sensors satisfy the above requirement, but they were readily available from PTI and were simple to interface when compared to alternative options such as an absolute encoder for the steering wheel.

4.1.2.1 Description of Steering Sensor

String potentiometers were first developed for NASA in the late 1960's for use in aircraft testing, as there was a need for accurate sensing devices that had flexibility in their mounting options. They are now found frequently in automotive testing applications such as monitoring the movements of a crash dummy in testing (such as the THOR Alpha and Advanced crash dummies used by NHTSA [1]), recording the deformation of points in the interior cabin of a vehicle in a crash [2], and monitoring suspension, gas pedal, and brake pedal travel [3] in addition to monitoring the steering angle [3, 4].

A string potentiometer works the same as a regular potentiometer with the exception that the resistance is varied by the actuation of a cable. This cable is tensioned with a constant-torque spring that serves to both prevent the cable from sagging and to allow it to retract into the base housing. The housing itself provides considerable protection to the sensor against water and dust.

Figure 4.2: String Potentiometer Used for Steering Angle Measurement

A typical circuit diagram of a potentiometer is shown in Figure 4.3. A reference voltage is placed across pins 1 and 3, with the sensor output being indicated by the voltage across pins 2 and 3. As the string translates, the angle theta of the potentiometer

changes, which alters the resistance between pins 2 and 3 and in turn causes a change in voltage. By monitoring the voltage change across these pins, the position of the cable may be deduced. Further information on the operating principles behind potentiometers may be found in Ernest Doeblin's book on page 212 [5].

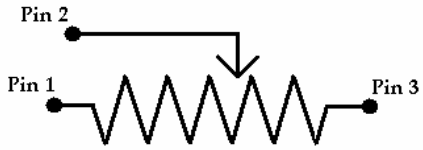

Figure 4.3: Typical Potentiometer Circuit Diagram

4.1.2.2 Steering Sensor Mounting

In order to provide redundancy, two string potentiometers were used. The cable of one was directly affixed to the driver's side of the steering arm, and the other was attached to the passenger side. The bases of the units were mounted to a custom frame that was bolted to the undercarriage of the vehicle. The position of the mount provides a clear, straight pathway for each of the potentiometer cables. The mount itself is constructed from 1" box steel to ensure rigidity.

The frame was designed such that it would mount to preexisting holes in the undercarriage. These holes were tapped to accommodate the mounting fixture. In order to ensure that the bolts will not loosen over time, a lock nut and washer was used on the threaded side, and a lock washer sandwiched between regular washers was used on the opposing side.

4.1.2.3 Steering Sensor Calibration

Slip plates were used to calibrate the steering sensors. These plates are typically used to determine if a car needs to have its front end aligned by comparing the left and right steering angles for a given displacement of the steering wheel. They also allowed for the creation of a calibration curve for the string potentiometers.

Figure 4.4: Wheel Angle Slip Plates

A reference voltage of +5v was output through one of the DAQ's analog outputs, and one of the analog inputs was used to read the voltage across the potentiometer. In order to determine the voltage corresponding to a zero steering angle, the car was driven straight for approximately 400m on flat, level pavement. The voltage on the potentiometers was averaged over this period. The car was then raised on jacks and the wheels were turned until the voltage corresponding to a zero steering angle was reached.

The measured voltage across each potentiometer was recorded at 5 degree intervals and plotted. Shown in Figure 4.5 and Figure 4.6, it is clear that the sensors do indeed follow a linear trend with an R^2 of 0.998 for the potentiometer on the driver's side

and an R^2 of 0.9993 for the one on the passenger side. Since both sensors demonstrated such linearity and a limited number of analog inputs were available, it was decided that only the driver-side sensor would be utilized, with the passenger-side sensor existing as a ready-made backup.

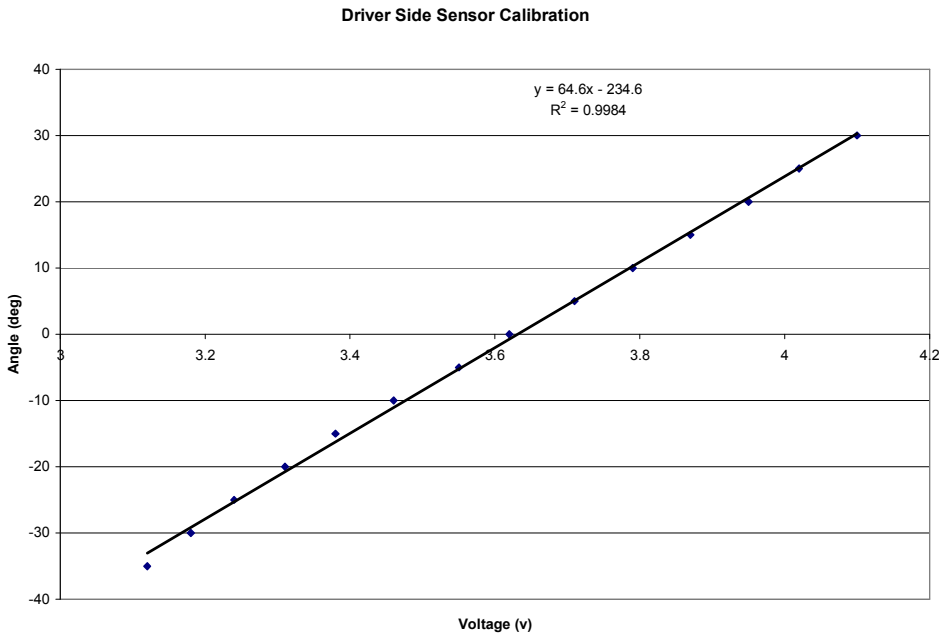

Figure **4.5**: Driver Side Steering Sensor Calibration Curve

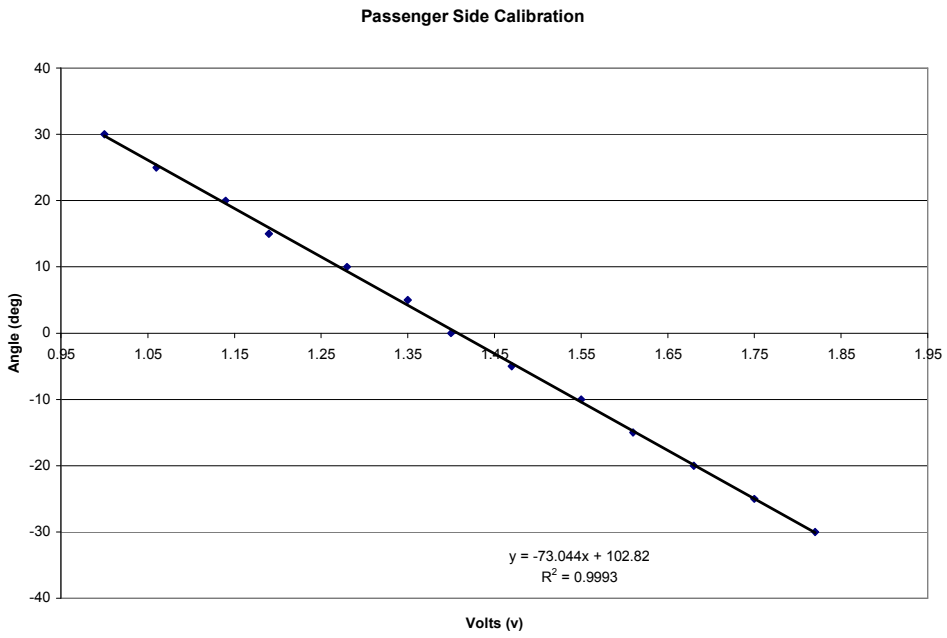

Figure 4.6: Passenger Side Steering Sensor Calibration Curve

4.1.2.4 Known Steering Sensor Issues

The only issues encountered with the string potentiometers are occasional spikes in the readings and the need to check the calibration frequently. While the former seems to occur simultaneously on all of the sensors, indicating an issue with the DAQ, it has a negative impact on the predictive ability of the models. The data is not filtered in real-time since filtering introduces a phase-lag in the measurements. The solution currently being implemented is to compare the current value to the previous value. If the difference is greater than a specified threshold, then the previous value is used for the current time step.

Minor adjustments must be made to the calibration curve on a regular basis. While the values have changed by less than 1% over approximately three months, the resulting difference in accuracy is considerable. Fortunately no inaccuracies have been found in the slope of the calibration curves, merely in the zero voltage, and so are easy to correct.

4.1.3 Yaw/Roll Rate Sensor

In order to determine the angular rate of the vehicle about the vertical axis, a Bosch yaw rate sensor (model MMR.01) was used. Power-on reset for this sensor was not a concern, as it does not give any absolute measurements, only angular rate. This sensor was also used to determine the roll rate of the vehicle. While the sensor is equipped with a lateral accelerometer, it was not used due to inaccuracies found in its sensing capabilities.

4.1.3.1 Description of the Rate Sensor

Shown in Figure 4.7, the yaw rate sensor is not very different from a traditional fly-ball governor. The sensor consists of two eccentric masses that are each allowed to traverse linearly along a track. Springs ensure that the travel of the masses is related to the centrifugal acceleration acing upon them. This distance is converted into a voltage, which is read from the sensors analog output pins.

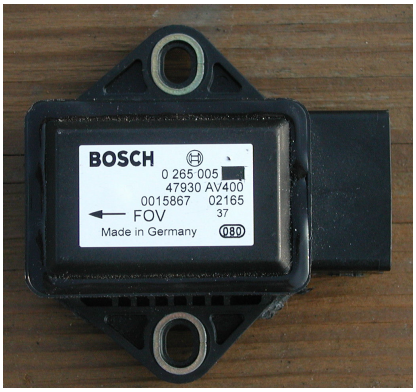

Figure 4.7: Angular Rate Sensor

The sensor outputs a reference voltage from which the calibration curve is derived. By subtracting off this voltage from the yaw rate signal, a more accurate reading may be obtained. For this reason, the yaw rate sensor requires two analog inputs.

4.1.3.2 Rate Sensor Mounting

Following the determination of the vehicles center of gravity (CG), the rate sensor was placed as close to its location as possible. The nearest accessible location, shown in Figure 4.8, is approximately 0.33m in the negative x direction from the location of the CG. Given the proximity of the sensor to the axis of rotation, it was not deemed necessary to apply a coordinate transformation to the measurements.

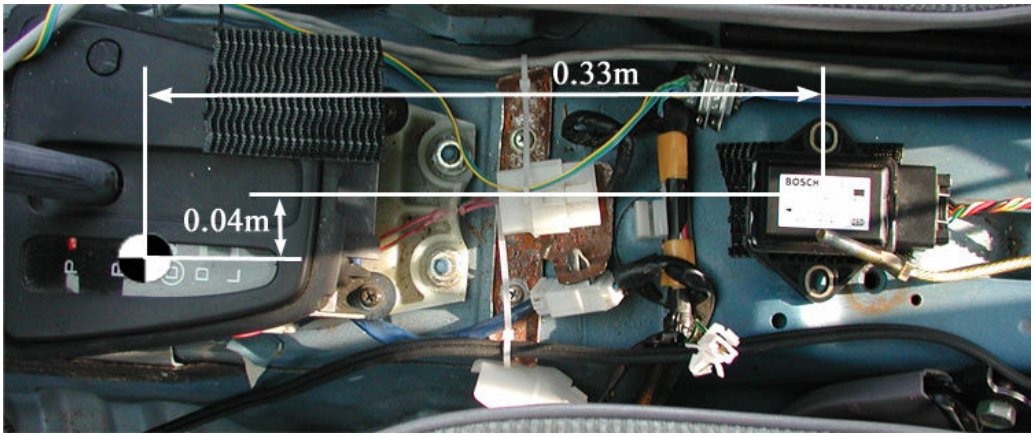

Figure 4.8: Location of the Angular Rate Sensor Relative to the Vehicle CG

Physically, the rate sensor is mounted to the vehicle's console by means of self-locking mushroom-head adhesive-backed strips, with a holding force of 18 pounds per square inch of surface area contact. This material was chosen to mount the sensor since it provides a rigid mounting surface that is both non-permanent and does not require any drilling which may damage vehicle control components.

Roll rate was measured by mounting the rate sensor to a piece of 90 degree angle aluminum. The base of the mount was then attached to the console utilizing the interlocking mushroom-head strip. Mounting of the sensor in this manner presented no noticeable loss in rigidity.

4.1.3.3 Rate Sensor Calibration

The calibration curve for the sensor was provided by Bosch in accompanying documentation provided with it. The relationship between the output voltage of the sensor and the angular rate is linear, with a maximum angular velocity of ±1.75 rad/s

(±100 deg/s). This is well within the range of values expected to be encountered in an automobile. The calibration of the sensor was tested by recording the yaw rate while stationary and again while traversing a circular path of known radius at a known speed. The only adjustment required was to eliminate a steady-state bias to the sensor of +0.012 rad/s.

4.1.3.4 Known Rate Sensor Issues

The rate sensor will occasionally give a non-zero reading when the vehicle is not in motion. It is therefore recommended that any evaluation of the sensors calibration be done while the vehicle is in motion in order to ensure correct sensor operation.

4.1.4 Lateral Accelerometer

The final sensor in the data acquisition architecture is an accelerometer. Like all of the previous sensors, a power-off reset will have no ill effect on this sensor or its accuracy. The range of the accelerometer used in this study is ±2g. This range is suitable for vehicle testing as the linearity conditions specified in Chapter 2 dictate that the lateral acceleration should not exceed 0.4g's.

4.1.4.1 Description of Accelerometer

Shown in Figure 4.9, it follows the typical construction of a non-piezoelectric accelerometer. A small mass on the interior is allowed to be displaced in the direction of

motion and is balanced by a spring and damper. The principle of operation is very similar to the rate sensor. Further information may be found in Doeblin's book on page 324 [5].

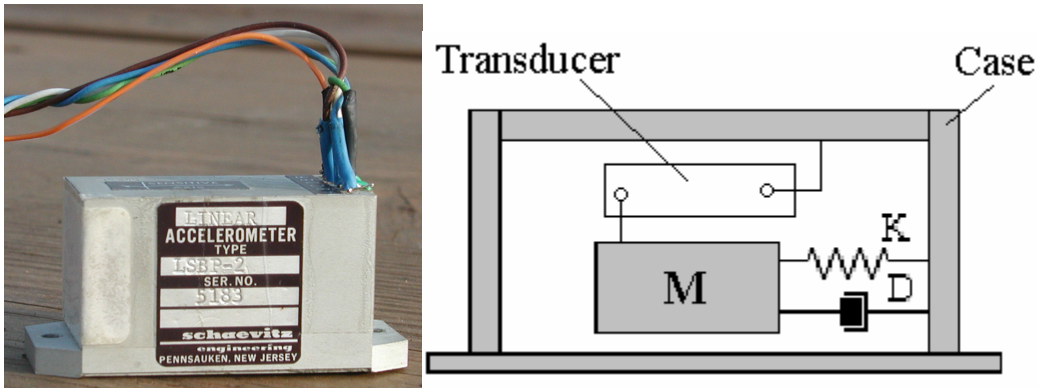

Figure 4.9: Accelerometer

4.1.4.2 Accelerometer Mounting

As with the rate sensor, the accelerometer was mounted in close proximity to the CG. As is indicated in Figure 4.10 the distance between the two is very small in relation to the dimensions of the vehicle. Therefore, no coordinate transform was necessary to correct the data. The sensor was affixed to a mounting plate on the vehicle using non-permanent high-rigidity putty.

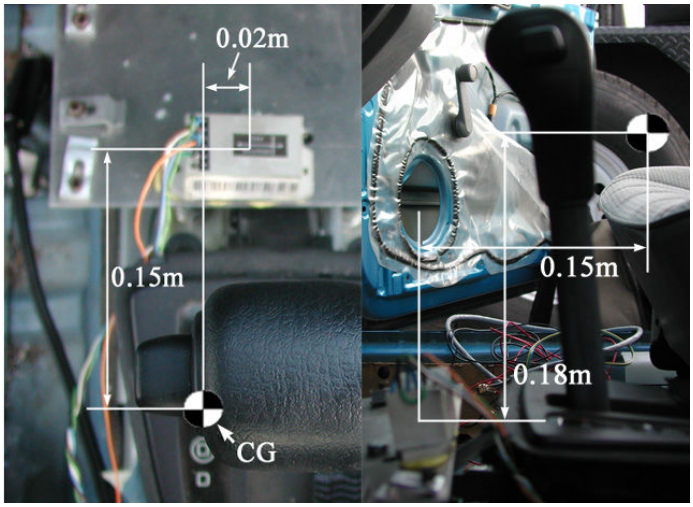

Figure 4.10: Accelerometer in relation to the vehicle CG

Like the self-interlocking strips, the putty material securely mounts the sensor to the vehicle chassis. Unlike the adhesive backing of the strips, it does not permanently bond with the casing of the sensor. This was a key concern as the sensor was temporarily on loan from the Department of Mechanical and Nuclear Engineering at PSU. Additionally, vibration-absorbing pads were placed in between the mount and the vehicle frame in an attempt to dampen some of the mechanical noise imparted to the sensor.

4.1.4.3 Accelerometer Calibration

The manual supplied with the sensor contained the slope and intercept values for the linear calibration curve between voltage and acceleration. This curve was tested by placing the sensor on a stationary, level surface and checking that the sensor reported zero g's of acceleration and by holding it vertically and checking for an acceleration of 1 g. The sensor reported the correct value in both situations.

Once the sensor was mounted in the vehicle, the angular offset of the mounting needed to be determined. A test similar to that performed by the angular rate sensor was executed, whereby the vehicle was driven around a circle of known radius at a constant known speed. In such steady state situations, the centrifugal acceleration acting upon a body is equal to:

$$a_{y,global} = \frac{U^2}{R} \tag{4.1}$$

where R is the radius of the turn. However, as pointed out by Wheeler et. al. [6] the acceleration felt by an observer in a body-fixed frame is:

$$a_{y,body-fixed} = a_{y,global} - Ur \tag{4.2}$$

Given the relationship that, in a steady state turn:

$$r = \frac{U}{R} \tag{4.3}$$

the lateral acceleration felt by an observer in the body-fixed vehicle frame under steady state turning conditions should be zero. Therefore, Eq. **4.2** was used to adjust the lateral acceleration readings such that the lateral acceleration in the body-fixed coordinate frame was recorded.

By performing a series of steady-state turning tests at various speeds and in both positive and negative directions, the steady-state offset of the sensor was determined to be +0.9 m/s^2. Following the addition of this correction factor and correcting for the centripetal acceleration acting on the vehicle, the system reported approximately zero lateral acceleration for all steady state turns the vehicle was able to perform without sliding.

4.1.4.4 Known Accelerometer Issues

The most apparent problem with the accelerometer was noise. The instrument itself is very sensitive, having a resolution of ±0.001g. As a result all of the vibrations of the vehicle are recorded including high frequency vibrations such as engine noise. Therefore all steady-state measurements are very noisy and require post-processing in order to determine the actual measured value. Such an issue is not uncommon when using accelerometers in vehicle dynamic analysis and has been found to be an issue in other works such as in [7].

Another more significant problem with the use of the accelerometer is the possibility of incorrect mounting. As discussed above, tests were performed to determine the angular offset associated with the accelerometer's mounting. However, this correction factor may contain some error. Since the experiments were performed under steady state conditions, the vehicle sprung mass will exhibit a constant roll angle. This roll angle alters the readings of the lateral accelerometer since a gravitational component of acceleration is introduced into the data. As a result, the correction factor will only apply under steady-state turning situations, for that specific radius (30.5m in this case). This limitation is a direct result of the roll angle of the vehicle being related to the lateral acceleration of the vehicle and the axial cross-coupling induced by it.

The only way to properly determine the orientation of the sensor with respect to the vehicle coordinate frame is by using a multi-axis sensor such as an Inertial Measurement Unit (IMU). Further discussion of this issue is given in the following section, as cross-axis coupling of dynamics became a significant issue in data collection.

Further examination of both the effect of roll dynamics on sensor measurement and the influence of noise on data processing will be examined further in Chapter 5.

A final error in the use of the accelerometer comes from the use of Eq. **4.2** when converting the measurements from a global to a body-fixed reference frame. This equation is highly dependent on velocity. Since velocity is not currently measured and there is no cruise control in the vehicle, the accuracy of this equation strongly depends on the speed of the vehicle being held constant.

4.2 Alternate Vehicle Instrumentation Setup

Not only does the roll motion of the vehicle influence the measurement of lateral acceleration, but also it influences yaw and roll rate. As shown in Figure **4.11**, it is seen that a roll angle induced on the vehicle will indeed cause the sensors to take measurements in a coordinate frame other than the tangential frame in which the equations of motion pertain. Imperfection in the sensors mounting may cause an artificial additional rotation about the y-axis, further affecting the measurements.

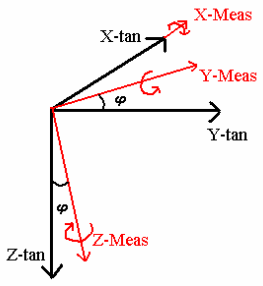

Figure **4.11**: Roll Effects on Vehicle Measurements

In an attempt to address the issue with incorrect axis alignment and cross-coupling of sensor readings, a Crossbow IMU (VGX model) was used. A key feature of the IMU is that it is capable of determining the roll and pitch angle of the unit with respect to a tangential coordinate plane. This is accomplished through a two-step process: First, shown in Figure 4.12, the high-bandwidth rate sensors are integrated continuously over time. However, due to inaccuracies in the rate sensors the answer will tend to drift from the true value after a matter of a few seconds. Second, the integration drift is corrected by utilizing the relatively low-bandwidth accelerometers.

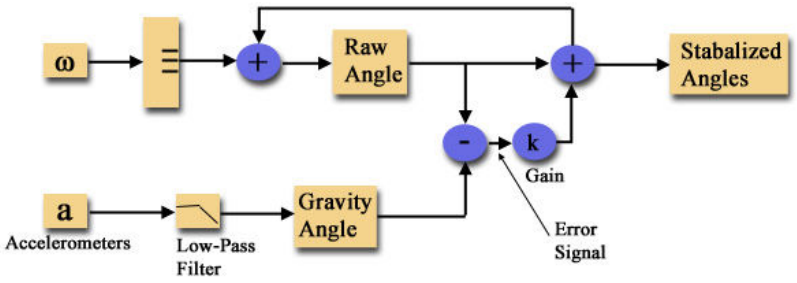

Figure 4.12: Method Employed By Crossbow to Determine the Global Roll and Pitch Angles of the Vehicle

If the sensing system relied too heavily on the rate gyros, errors would occur as a result of integration. Likewise if reliance was placed too heavily on the accelerometers, the data acquisition rate would be too slow. By striking a balance between the two, an accurate solution may be acquired at high data rates. It is important to note that the degree to which one selects appropriate bandwidth is application dependent, and must be tuned for optimum performance and the application at hand.

The angles reported by this IMU follow the standard Euler angle rotation. Therefore, by defining the roll angle as φ and the pitch angle as θ the measured data may be converted to measurements in the tangential coordinate frame by

$$\begin{bmatrix} \omega_{x,\tan} \\ \omega_{y,\tan} \\ \omega_{z,\tan} \end{bmatrix} = \begin{bmatrix} \cos\theta & 0 & \sin\theta \\ 0 & 1 & 0 \\ -\sin\theta & 0 & \cos\theta \end{bmatrix} \begin{bmatrix} 1 & 0 & 0 \\ 0 & \cos\phi & -\sin\phi \\ 0 & \sin\phi & \cos\phi \end{bmatrix} \begin{bmatrix} \omega_{x,meas} \\ \omega_{y,meas} \\ \omega_{z,meas} \end{bmatrix} \quad \textbf{4.4}$$

and:

$$\begin{bmatrix} a_{O_V,x,\tan} \\ a_{O_V,y,\tan} \\ a_{O_V,z,\tan} \end{bmatrix} = \begin{bmatrix} \cos\theta & 0 & \sin\theta \\ 0 & 1 & 0 \\ -\sin\theta & 0 & \cos\theta \end{bmatrix} \begin{bmatrix} 1 & 0 & 0 \\ 0 & \cos\phi & -\sin\theta \\ 0 & \sin\theta & \cos\phi \end{bmatrix} \begin{bmatrix} a_{O_V,x,meas} \\ a_{O_V,y,meas} \\ a_{O_V,z,meas} \end{bmatrix} \quad \textbf{4.5}$$

The addition of the Crossbow IMU to the data acquisition system required the use of one of the two available serial ports. This modified structure is shown in Figure **4.13**.

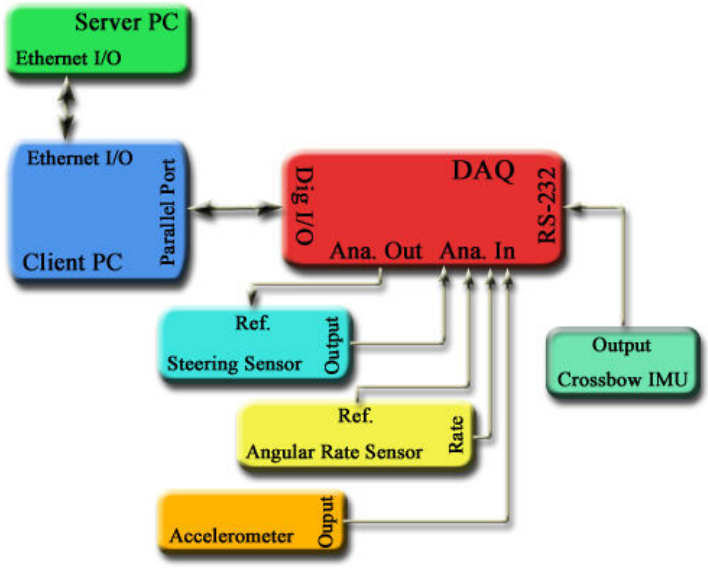

Figure **4.13**: Data Acquisition and Sensing Architecture with the Crossbow IMU

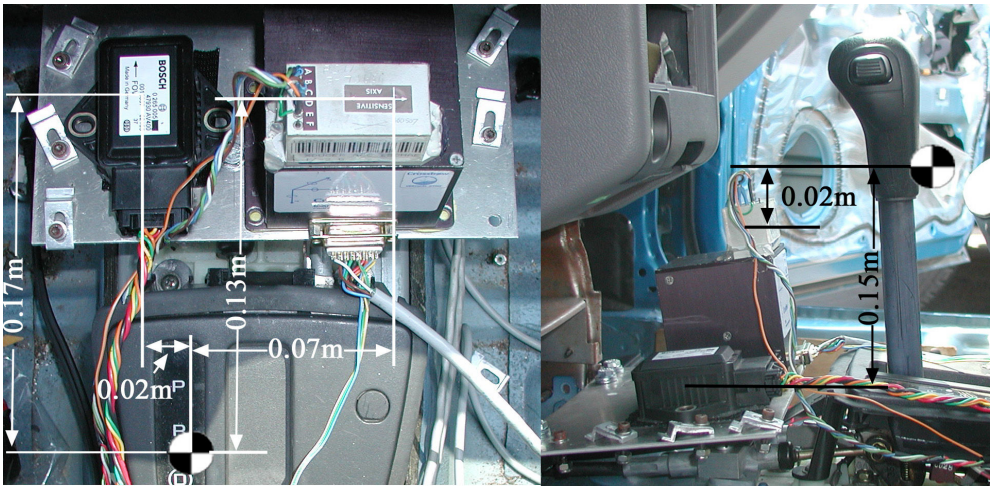

Figure 4.14: Sensor Mounting Following the Addition of the Crossbow IMU

4.2.1 Comparison between Sensing Systems

A series of tests were performed whereby data was collected from all of the sensors simultaneously and the data was compared. In order to provide an objective comparison, the sensors were mounted as shown in Figure 4.14 so that they were all subjected to similar mounting offsets. The first test performed involved driving the test vehicle about a 30.5m radius circle at 8.9 m/s in both directions in order to show if the two systems reported the same measurements under steady-state conditions. The results are shown below.

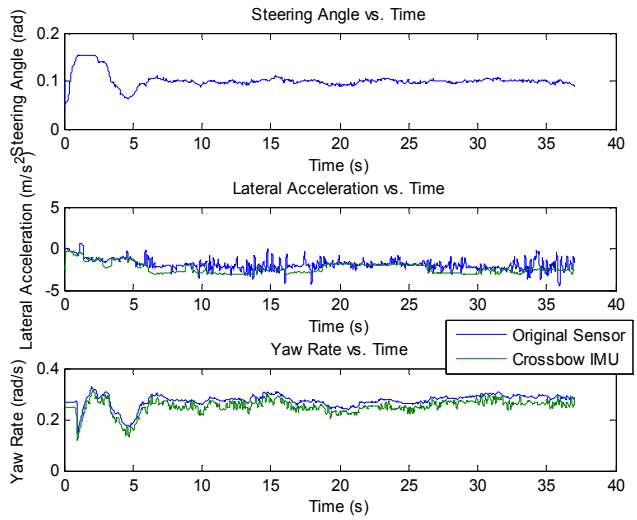

Figure **4.15**: Data Comparison, Turning Circle, 8.9 m/s, Clockwise

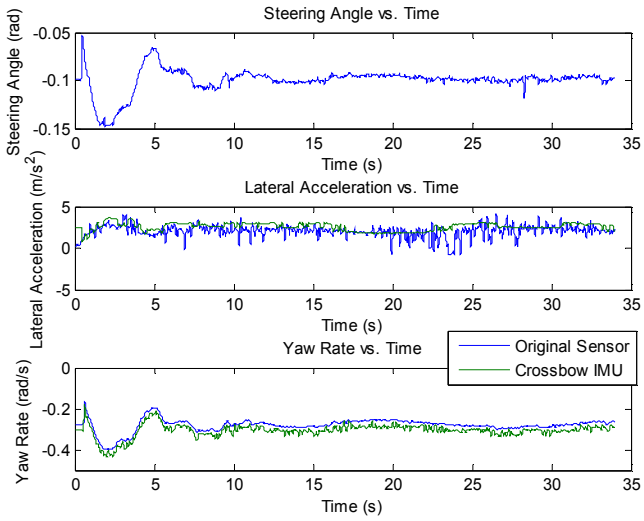

Figure **4.16**: Data Comparison, Turning Circle, 8.9 m/s, Counterclockwise

Both Figure **4.15** and Figure **4.16** indicate that both the IMU and the original sensors report nearly identical measurements under steady state conditions. Additionally the lateral acceleration recorded by the IMU is smoother than output from the accelerometer. This is likely due to the low-pass filter indicated in Figure **4.12**.

The next series of tests involved cyclic oscillation of the vehicle with a fixed steering amplitude. A low frequency test at 0.5 Hz and a high frequency test at 2.5 Hz were executed in order to compare the transient behavior of the sensors. The results of the low frequency test are shown in Figure **4.17**. Regarding the lateral acceleration, an apparent phase lag exists between the accelerometer and the IMU. This may also be a result of the low-pass filter placed on the output of the IMU's accelerometers. In the yaw response, minor differences arise in the magnitude of the data.

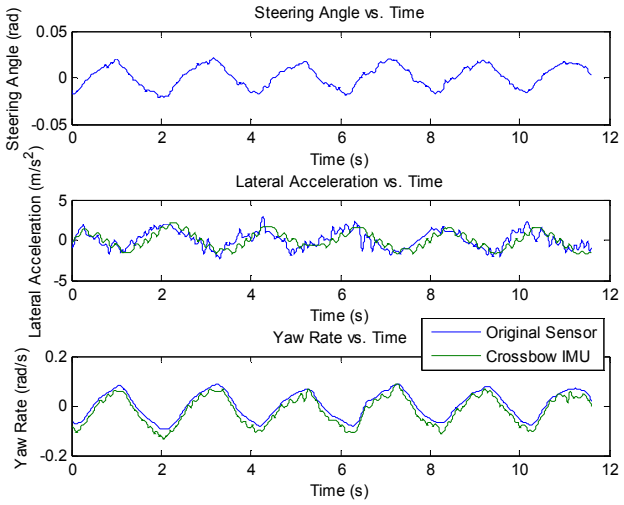

Figure **4.17**: Data Comparison, Low Frequency Oscillation (0.5Hz), 22.4 m/s

The results of the high frequency test shows disagreement between the sensor systems. Figure **4.18** reveals that while the yaw response still exhibits behavior similar to that shown at low frequencies, the IMU shows almost no response in regards to lateral acceleration. However, since the data from the accelerometer was not a sine wave of consistent amplitude and frequency as expected, a new set of tests was performed.

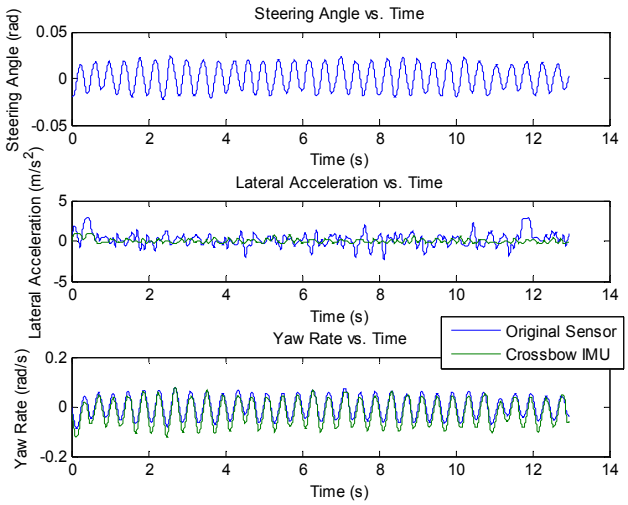

Figure **4.18**: Data Comparison, Low Frequency Oscillation (2.5Hz), 22.4 m/s

The next series of tests performed are nearly identical to the cyclic oscillations described above. The key difference is that the speed of the tests was decreased from 22.4 m/s to 8.9 m/s. At higher speeds, the dynamics of the vehicle are easily excited. However, the limited space on the test track restricts the number of cycles that may be performed. Additionally, at higher speeds it is easier to exceed the linear bounds of the models and great care must be taken to keep the input amplitude low enough to maintain reasonable lateral accelerations (less than 0.3 g) while still remaining consistent in the steering input.

By executing the tests at low speeds, not only can a large number of oscillations be performed but there is more leeway in the input amplitude that may be used. Therefore, the tests will be performed at 8.9 m/s at 0.67 Hz and 2.5 Hz. The lateral acceleration results of the low frequency tests are shown in Figure **4.19**. Examination of the data shows that while the phase of measurements between the two sensor systems

matched well, the IMU shows significant undershoot on the lower bound of the sine wave.

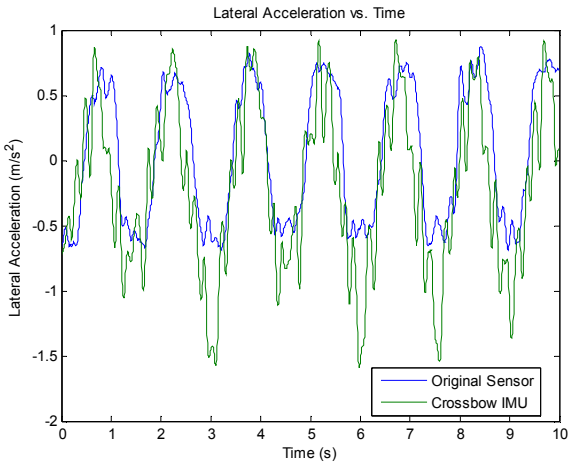

Figure **4.19**: Data Comparison, Lateral Acceleration, 0.67Hz, 8.9 m/s

The higher frequency test results largely agreed with those shown in Figure **4.20** whereby the IMU measures significantly lower amplitude than the accelerometer. Additionally, the phase of the IMU seems to be off as well. This is consistent with the effects of a low-pass filter. In contrast, the accelerometer clearly captures the dynamics of the vehicle, exhibiting a clear sinusoidal structure with a measured frequency of 2.50 Hz.

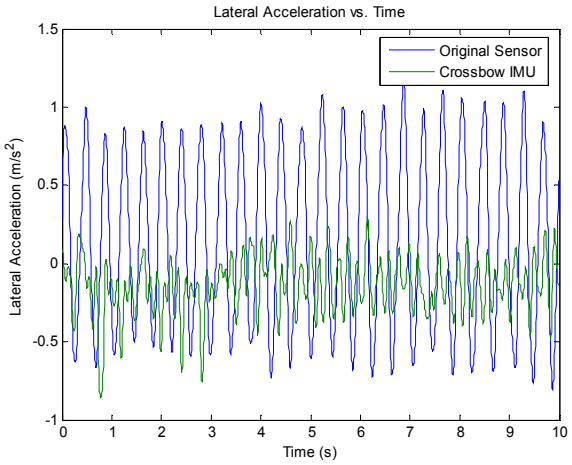

Figure **4.20**: Data Comparison, Lateral Acceleration, 2.5Hz, 8.9 m/s

4.2.2 Evaluation of Hybrid Sensing Architecture

Since the effects of the low-pass filter inhibit the IMU's measurement of the dynamics of the vehicle, a final hybrid configuration was attempted. Since the IMU primarily relies upon the rate sensors in order to determine the roll and pitch angles of the unit during high frequency maneuvers, it was hypothesized that these angles could be used to correct the measurements obtained from the original, non-IMU sensors in off-line corrections.

As shown in Eq. **4.5**, in order to correct the lateral acceleration measured in the rotated frame (shown in red in Figure **4.11**), all three acceleration components in that frame are required. Since it was determined that the IMU's accelerometers could not be used, a different approach was required. An alternate representation is illustrated by

Figure 4.21 and looks at the orientation of the accelerometer in the y-z plane only. The vectors indicated in the figure have the following definitions:

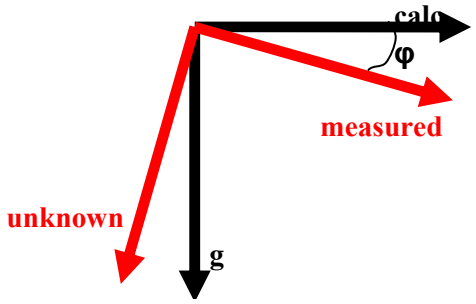

Figure 4.21: Alternate Coordinate Frame Representation for Lateral Acceleration Measurement

- calc: the true lateral acceleration of the vehicle
- measured: the lateral acceleration measured by the sensor
- g: gravity
- φ: roll angle of the vehicle indicated by the IMU
- unknown: an unknown orthogonal vector to the one that is measured

Note that in order for this representation to be accurate the vehicle must be on relatively level terrain as well from the assumption that gravity is always orthogonal to the lateral acceleration of the vehicle. If the vector *unknown* were known, a simple rotation by the angle φ would be all that was required. However, since this quantity is not known the following formulation was used instead.

From Figure 4.21, the first equation required to solve for the vector *calc* is:

$$calc = measured \cdot \cos(\phi) - unknown \cdot \sin(\phi) \qquad 4.6$$

The second equation comes from vector math. The norm of a vector defined by two orthogonal vectors will always be the same, regardless of the orientation of the unit basis vectors defining the vector. In other words, rotation does not change the norm of orthogonal vectors. This relationship gives:

$$\sqrt{g^2 + calc^2} = \sqrt{meas^2 + unknown^2} \tag{4.7}$$

Solving Eq. 4.7 for *calc* results in:

$$calc = \sqrt{meas^2 + unknown^2 - g^2} \tag{4.8}$$

Since the angle φ is known, Eq. 4.6 will be used to obtain an expression for *unknown*. Solving for *unknown* yields:

$$unknown = \frac{meas \cdot \cos(\phi) - calc}{\sin(\phi)} \tag{4.9}$$

Substituting Eq. 4.9 into Eq. 4.8 gives:

$$calc = \sqrt{meas^2 + \left(\frac{meas \cdot \cos(\phi) - calc}{\sin(\phi)}\right)^2 - g^2} \tag{4.10}$$

Utilizing the symbolic solver in MATLAB, an explicit expression for *calc* may be found in terms of *g*, φ, and *meas*. This expression is:

$$calc = \frac{-2 \cdot meas \cdot c(\phi) \mp 2 \cdot \sqrt{meas^2 \cdot c^2(\phi) - s^4(\phi) \cdot g^2 + meas^2 \cdot s^2(\phi) + g^2 \cdot s^2(\phi) - meas^2}}{2 \cdot (s^2(\phi) - 1)} \tag{4.11}$$

where ∓ refers to when *meas* has a positive or negative value, respectively (note the difference in sign). Simplification of Eq. 4.11 yields:

$$calc = \frac{-2 \cdot meas \cdot \cos(\phi) \pm signum(\cos(\phi)) \cdot \sqrt{1 - \cos(\phi)^2} \cdot |g|}{2 \cdot (\sin^2(\phi) - 1)} \tag{4.12}$$

where ± corresponds to a positive and negative value of *meas*, respectively.

In order to avoid cross-axis coupling with the rate sensor measurements, the local roll rate and pitch rate measurements from the IMU are combined with the yaw rate measurement from the Bosch sensor. A standard coordinate transformation is then

applied to these values as specified by Eq. **4.4**, with the measured components of angular velocity forming the input vector.

The first maneuver performed to test the hybrid architecture was a lane change maneuver executed at 15.6 m/s. The vehicle was first brought up to speed and made a straight-line approach to the lane change testing area of the test track. This area consists of a single solid yellow line painted on flat terrain that indicates a lane change from the right lane to the left lane, and then back again.

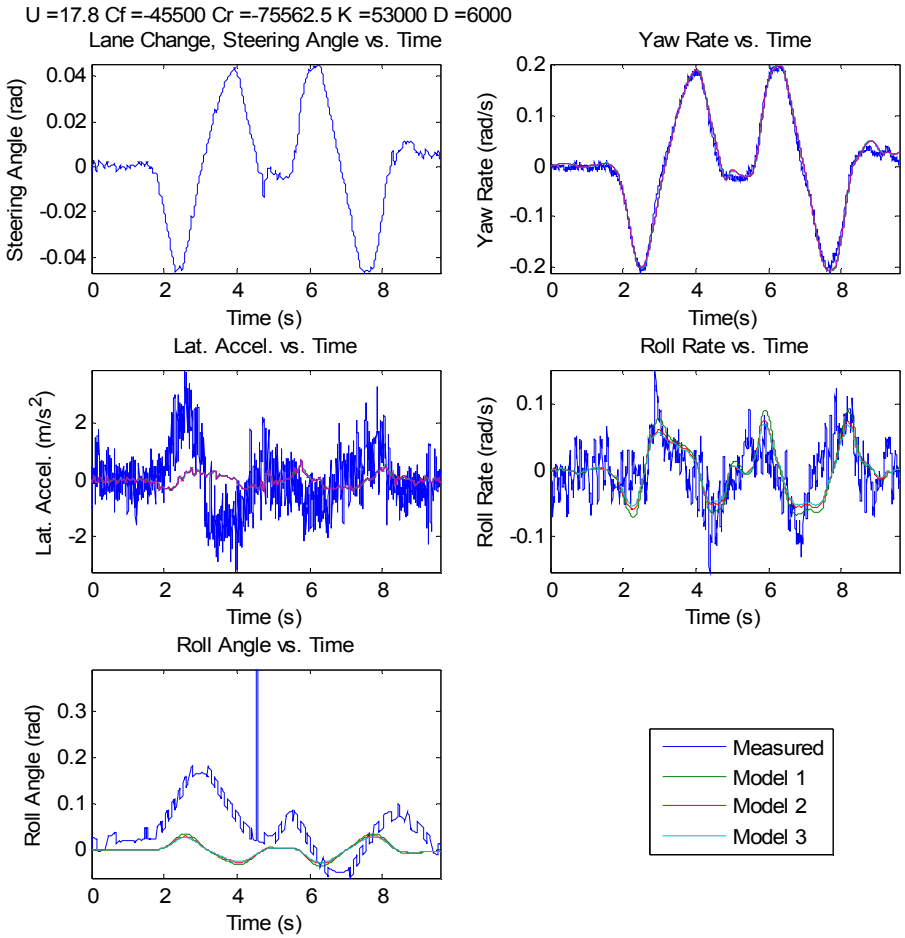

Figure **4.22**: Hybrid Sensing Architecture Test, Lane Change, 17.8 m/s

In order to gain a sense of the accuracy of this set up, the data was compared to the predicted response of Models 1 – 4. The parameters used were determined in previous experiments which are detailed in Chapter 5. From the results in Figure **4.22** it is seen that the models match both the measured yaw rate and the roll rate well. However, significant error exists between the measured and predicted values for both lateral acceleration and roll angle.

Although previous measurements for lateral acceleration are known to contain a bias error due to the influence of gravity and variations in longitudinal speed, the difference between the measured and predicted values in this test is significant. However, the differences between the measured and predicted roll angles are more indicative of the problem with the hybrid system: inaccuracies in the global roll and pitch angles determined by the IMU. While the measured and the predicted roll rates match well qualitatively, the roll angles differ by an order of magnitude. Given that both the initial measured roll angle and the predicted values are nearly zero, this result would suggest an error in the IMU's estimation of vehicle roll angle. This error in roll angle estimation directly results in the errors so clearly seen in the measured lateral acceleration, as this angle is used to correct the lateral acceleration for axial cross coupling.

The second and final test performed on the hybrid system was a step response at 8.9 m/s. The vehicle was brought to speed, driven along a straight path, and then a step input of approximately 0.095 rad. executed. As with the previous test the measured data was compared to the response predicted by Models 1 – 4. The results are shown below in Figure **4.23**.

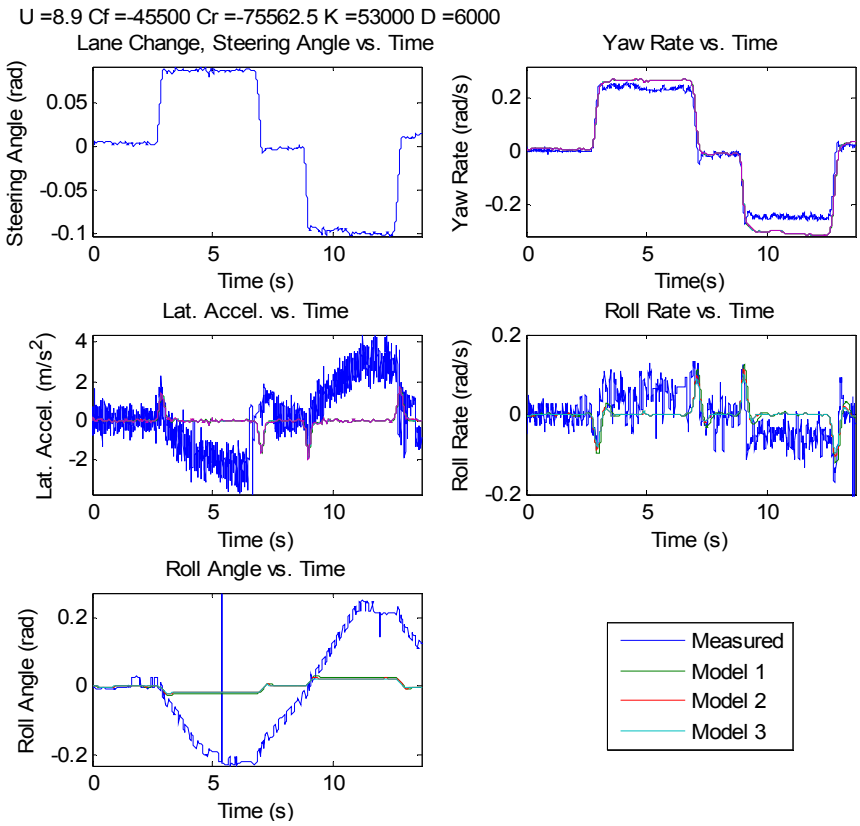

Figure **4.23**: Hybrid Sensing Architecture Test, Lane Change, 8.9 m/s

The behavior of the IMU's roll angle response confirms the inaccuracies in its estimation of that parameter. Even if the predicted roll angle is incorrect, the measured value should come to steady state in approximately the same amount of time. The measurements do not even make physical sense, as they suggest that following a step input the vehicle takes approximately four seconds to reach a steady state roll angle of ±0.2 rad. Much like the data for the lane change maneuver, this roll angle error translates directly to the drift seen in the measured lateral acceleration, as the angle is being used to correct this state for axial cross coupling.

As a result of these findings it was decided that the original sensing architecture outlined in Section **4.1** would be used. It should be noted that the IMU itself may have

been damaged as it has been used in previous crash-related tests at PTI. Future work will involve the use of a new IMU in conjunction with a differential global positioning system (DGPS). A similar comparison will be performed between the DGPS system and the current instrumentation in order to better determine its accuracy.

[1] *Thor Alpha User's Manual*: National Highway Traffic Safety Administration Biomechanics Research Center, 2001.

[2] G. C. Rains and M. A. Van Voorhis, "Quasi Static and Dynamic Roof Crush Testing," National Highway Traffic Safety Administration, Final Report VRTC-82-0197/VRTC-86-0391, June 1998.

[3] A. T. Marriott, F. M. Condos, J. A. Garba, D. C. Griffin, A. C. Kanner, M. V. Koffman, and A. Y. Lee, "Variable Dynamic Testbed Vehicle Study," Jet Propulsion Laboratory, California Institute of Technology, Final Report JPL D-11266, vol. III, August 30 1994.

[4] P. Hingwe, J.-Y. Wang, M. Tai, and M. Tomizuka, "Lateral Control of Heavy Duty Vehicles for Automated Highway System: Experimental Study on a Tractor Semi-trailer," California PATH Program, Institue of Transportation Studies, University of California, Berkeley, Working Paper UCB-ITS-PWP-2000-1, January 2000.

[5] E. O. Doeblin, *Measurement Systems, Application and Design*, 4th ed. New York, New York: McGraw-Hill, 1990.

[6] M. Wheeler, and Shoureshi, R., "A Fuzzy Driver on the Handling Track," *Transactions of the American Society of Mechanical Engineers (ASME)*, vol. 118, pp. 380-386, 1996.

[7] P. Stewart, J. C. Zavala, and P. J. Fleming, "Automotive drive by wire controller design by multi-objective techniques," *Control Engineering Practice*, pp. 257-264, 2005.

Chapter 5

Experimental Model Validation

This chapter will present the results of the experiments performed to determine which model (or models) represent the measured data to the greatest degree of accuracy. The chapter will be divided into three primary sections: determination of vehicle parameters, frequency domain model fitting, and time domain model fitting. Each of the two validation methods – time domain and frequency domain – offers some advantages over the other, and these will be discussed in further detail in their respective sections.

By using both frequency and time domain model fitting methods, a "best-fit" will be achieved by varying only a limited number of parameters in the models: the cornering stiffness, roll damping, and roll stiffness parametric values. These parameters were chosen due to their relatively large amount uncertainty when compared with more certain and easily measured or readily available values such as mass, inertia, and CG location.

5.1 Determination of Vehicle Parameters and Inertial Properties

This section describes the procedures and experiments used to obtain initial estimates on the following vehicle parameters:

- Mass
- Location of Vehicle CG, which entails:
  - Axle-to-CG Distances, l_f and l_r
  - Height of CG from Ground
  - Distance from side of vehicle to CG, e
- Inertial Properties (I_{xx}, I_{zz}, and I_{xz})

- Sprung Mass
- Roll Stiffness and Roll Damping
- Cornering Stiffness – governing relationship between C_f and C_r

5.1.1 Determination of Mass Center

The first step in the determination of the vehicle's center of gravity (CG) was to measure the total mass of the Mercury Tracer. This was accomplished by lowering the vehicle onto a set of four scales – one on each tire. The results are shown in Figure 5.1.

Vehicle length L and track width e were determined by measuring the distance between the tire centers with a tape measure. Combining these measurements with the weight distribution of the vehicle, the location of the vehicle CG may be determined by proportionality. These relationships are:

$$l_f = \left(1 - \frac{W_{front}}{W_{car}}\right) \cdot L \qquad 5.1$$

$$l_r = L - l_f \qquad 5.2$$

$$e = \left(1 - \frac{W_{right}}{W_{car}}\right) \cdot t \qquad 5.3$$

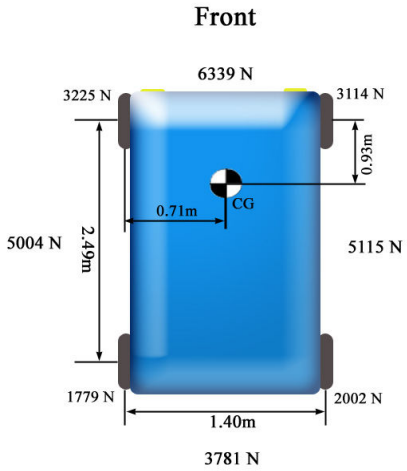

Figure 5.1: Vehicle Weight Distribution and CG Location – X-Y Plane

The measured location of the CG and vehicle dimensions are nearly identical to those obtained by NHTSA for a 1998 Mercury Tracer [1]. A comparison between the values in the NHTSA database and the values obtained by direct measurement on the 1996 Mercury Tracer is shown in Table 5.1. While there is a difference of approximately 10% in the mass, the location of the CG in the X-Y plane is nearly identical. Given this fact, the CG height obtained by NHTSA for the 1998 Mercury Tracer was used in this study.

The margin of error between the CG locations is so minimal that it suggests that the mass distribution between the two models is equally similar. Therefore, it was decided that the values from the NHTSA database would be used as an initial estimate of inertial parameters.

Additionally, the errors in the inertia values provided by NHTSA are reported to be ± 1%. These values were obtained using the Vehicle Inertia Measurement Facility (VIMF) developed by S.E.A Limited, located in Columbus, Ohio. The facility utilizes

methods similar to those described by Dixon [2] (pages 17-31) to determine the location of the vehicle CG and find the inertial properties. However, extensive error analysis was performed on the system, an analysis which gives rise to the accuracy of inertial measurement. It is generally regarded as the most accurate facility available in the United States to determine vehicle inertial parameters [1].

Table 5.1: Comparison Between Measured Values and NHTSA Database Values

Parameter	NHTSA Value	Measured Value	Deviation from NHTSA Value (%)
m (kg)	1224	1106	9.64
L (m)	2.494	2.49	0.20
l_f (m)	0.927	0.93	0.32
l_r (m)	1.567	1.56	0.51
t (m)	1.43	1.40	2.10

5.1.2 Roll Stiffness and Damping

There is no publicly available database of vehicle roll stiffness and damping coefficients. While some methods have recently been proposed to obtain these parameters dynamically [3], there is no established procedure for doing so. Therefore, an initial estimate was obtained using the following procedure:

- The vehicle begins at rest on a flat surface, and the data-acquisition system continuously measures roll rate.
- The vehicle is then forcibly oscillated about its roll axis. This oscillation is maintained for an undefined period but one that is sufficient for reaching steady-state response to the sinusoid excitation of input
- Force input is terminated at an extreme angular displacement, and the vehicle is allowed to come to rest.

- The data is then analyzed by comparing the vehicle to an inverted pendulum (shown in Figure **5.2**).
- Initial conditions are obtained from the recorded data, with roll obtained from the integration of the recorded roll rate (shown in Figure **5.3**).

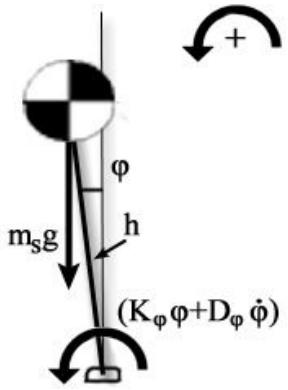

Figure **5.2**: Free-Body Diagram of Inverted Pendulum Model for Roll Parameter Estimation

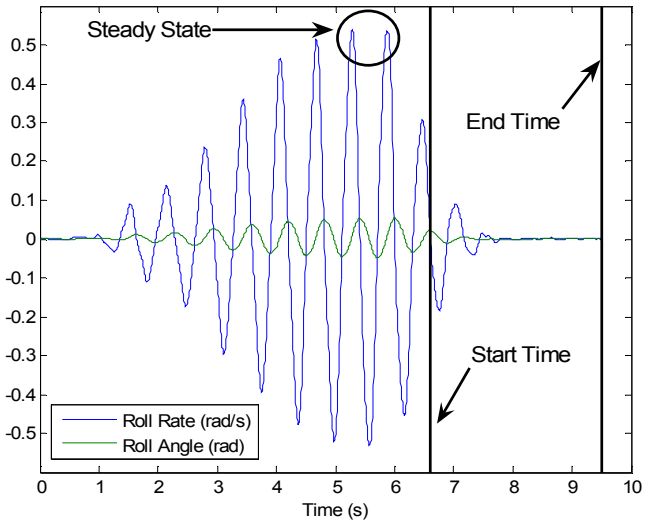

Figure **5.3**: Roll Response Test Data

By summing moments about the base of the pendulum in Figure 5.2 a second order model is obtained for the system. This is described by:

$$\ddot{\phi} = -\frac{D_\phi}{I_{pendulum}}\dot{\phi} - \frac{K_\phi - m_s \cdot g}{I_{pendulum}}\phi \qquad 5.4$$

with $I_{pendulum}$ being defined by the parallel axis theorem as:

$$I_{pendulum} = m_s \cdot h^2 \qquad 5.5$$

The data between time t = 6.605s and t = 9.5s was used for the model fit. Examination of the data at t = 6.605s gives the initial conditions of $\dot{\phi}_0 = 0.002214\,\text{rad/s}$ and $\phi_0 = 0.02179\,\text{rad}$. The free response was simulated as shown in Figure 5.4.

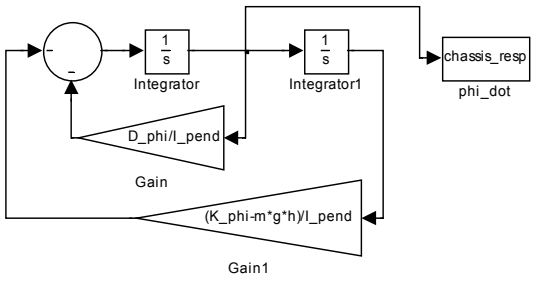

Figure 5.4: Suspension Free Response Simulation – Inverted Pendulum Model

Manual parametric variation of the sprung mass, roll stiffness, and roll damping resulted in the following values:

- Roll Stiffness: 32,000 N/rad
- Roll Damping: 1050 N-s/rad
- Sprung Mass: 825 kg

The resulting model fit, shown below in Figure 5.5, shows fairly accurate results for the first half of the simulation. This accuracy rapidly degenerates as the simulation proceeds. This is likely due to factors such as non-linear damping characteristics that

occur near zero suspension velocity as in [4], as well as the likely occurrence of lateral motion of the suspension. Lateral suspension displacement would imply that energy from the roll mode is transferred to lateral motion and this behavior is suggested by the roll data recorded. This comes from the data in the second half of the simulation exhibiting behavior characteristic of systems higher than second order. However, further experimentation would need to be executed to determine if this is the case. Either of these factors would invalidate the model as the suspension would no longer resemble an axle supported by a linear spring and damper at either end.

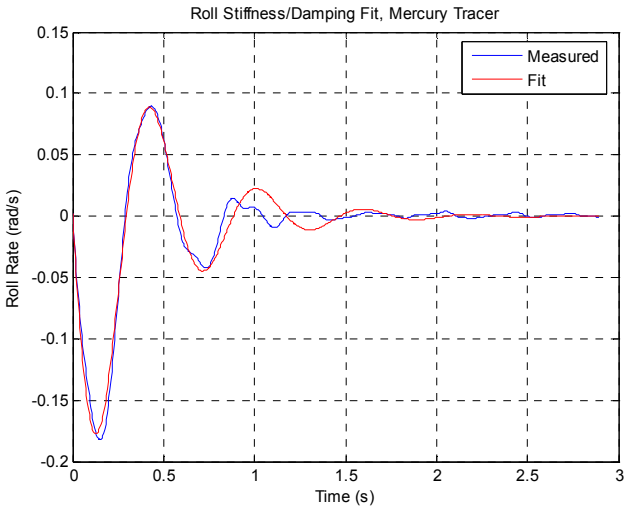

Figure **5.5**: Roll Stiffness and Damping Model Fit Results

Despite these shortcomings, it was decided that the values obtained from the fit were accurate enough to be used as initial parameter values. Further refinement of them will be discussed in the proceeding sections where experimental validation is used to test these initial parameter fits.

5.1.3 Experimental Determination of Understeer Gradient

As discussed in Section 2.2, the understeer gradient of a vehicle is a constant indicating the additional amount of steering (measured per g of lateral acceleration in the global frame) necessary to maintain a steady-state turn negotiated at increasingly larger velocities. This is expressed mathematically by:

$$\delta_f = \frac{L}{R} + K_{us} \cdot a_{y,global} \qquad 5.6$$

where K_{us} is the understeer gradient and $a_{y,global}$ is the lateral acceleration of the vehicle. Finding this constant not only gives insight into the behavior of a vehicle, but it also provides a relationship between the front and rear cornering stiffnesses, which are difficult to measure, and the weight on the front and rear tires, which are easy to measure. This relationship is shown below in Eq. 5.7.

$$K_{us} = \frac{W_r}{2 \cdot C_f} - \frac{W_f}{2 \cdot C_r} \qquad 5.7$$

The sensors required for determining the understeer gradient of the vehicle are a steering angle sensor and either an accelerometer or a yaw rate sensor. For this experiment, the existing sensors on the vehicle were used. The Tracer was driven at 6.7, 8.9, and 11.2 m/s around a 30.5m radius circle. At speeds below 6.7 m/s, it was difficult for the driver to maintain constant speed and for speeds in excess of 11.2 m/s the vehicle exceeded the linear bounds of lateral acceleration. Therefore, only three data points were used. Further experimentation will require a turning circle of larger radius, which is currently unavailable.

In order to limit the error in the measurement of lateral acceleration, the yaw rate of the vehicle was recorded and the lateral acceleration was determined by the relationship:

$$a_{y,global} = \frac{U \cdot r}{g} \qquad \textbf{5.8}$$

For each test, the vehicle was driven around the test circle for approximately sixty seconds and the recorded steering angle and yaw rate were averaged. By plotting the additional steering angle required to make the turn for a given speed (defined by Eq. **5.9**) vs. the associated lateral acceleration as was done in Figure **5.6**, the understeer gradient is easily found by taking the slope of a best fit line.

$$\delta_{f,additional} = \delta_f - \frac{L}{R} \qquad \textbf{5.9}$$

Table **5.2**: Tabulated Data from Understeer Gradient Experiments

Velocity (m/s)	Lateral Acceleration (g)	Additional Steering Angle (rad)
6.7	0.140	0.025
8.9	0.263	0.030
11.2	0.379	0.036

Understeer Gradient = 0.045 rad/g

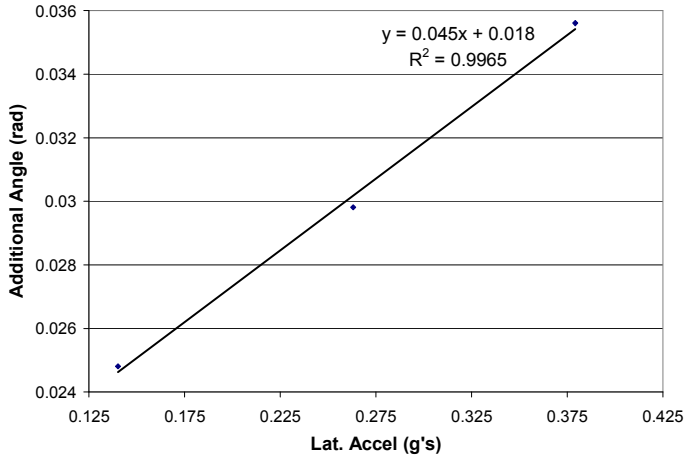

Figure 5.6: Additional Steering Angle vs. Lateral Acceleration

The results shown in Figure 5.6 suggest that it is reasonable to assume that the measured understeer gradient of 0.045 rad/g has a high degree of accuracy. Using this value in conjunction with Eq. 5.7, a relationship between the front and rear cornering stiffness values is obtained by relating front to rear cornering stiffnesses in terms of understeer gradient and vehicle weight. This relationship is enforced later in estimating cornering stiffness.

5.2 Frequency Domain Model Fitting

5.2.1 Bicycle Model Fit – Manual Parametric Variation

In order to determine the validity of the models used in this study, they were first compared in the frequency domain. The frequency response test involved inputting sinusoidal steering inputs at evenly spaced frequencies varying between 0.67 Hz and 3.33 Hz. Frequencies below 0.67 Hz were omitted due to limited space on the test track, and

higher frequencies were omitted as a result of physical limitations of the driver. To maintain constant frequency and phase, the sinusoidal steering input was synchronized to a digital metronome. Additionally, witness marks on the steering wheel were used to ensure consistency in amplitude. Nineteen frequencies were used to create each frequency response, and data was recorded at two speeds: 8.9 and 16.5 m/s.

The dynamic frequency response of the vehicle was recorded in the yaw rate, roll rate, and lateral acceleration states. At each frequency, a sinusoid was fit to the recorded steering input by using a nonlinear fitting routine that minimized sum-of-squares error between measured data and a best-fit sine wave. From the best fit sine wave, the frequency, amplitude, and phase angle of the input signal was obtained. A similar fit was then performed on the output data; however, in performing the fit of the output, the frequency was not allowed to be a free parameter but was fixed at the input frequency. With sinusoid fits for the input and output signals, the frequency response was readily determined.

As mentioned previously the cornering stiffness, roll stiffness, and roll damping parameters will be varied in order to determine a best fit match. In order to simplify the process, Model 1 was fit to the frequency response data such that values for the front and rear cornering stiffness' could be obtained. These values were then applied to Models 2 – 4 where the roll stiffness and roll damping parameters were varied.

Solving Eq. **5.7** for C_r, the relationship:

$$C_r = \frac{W_f \cdot C_f}{W_r - 2 \cdot K_{us} \cdot C_f} \qquad \textbf{5.10}$$

will be used to determine the corresponding rear cornering stiffness values as the front cornering stiffness is varied between -22,750 and -113,750 N/rad. The effects of this variation on Model 1 in both lateral acceleration and yaw rate are shown in Figure **5.7** for both speeds.

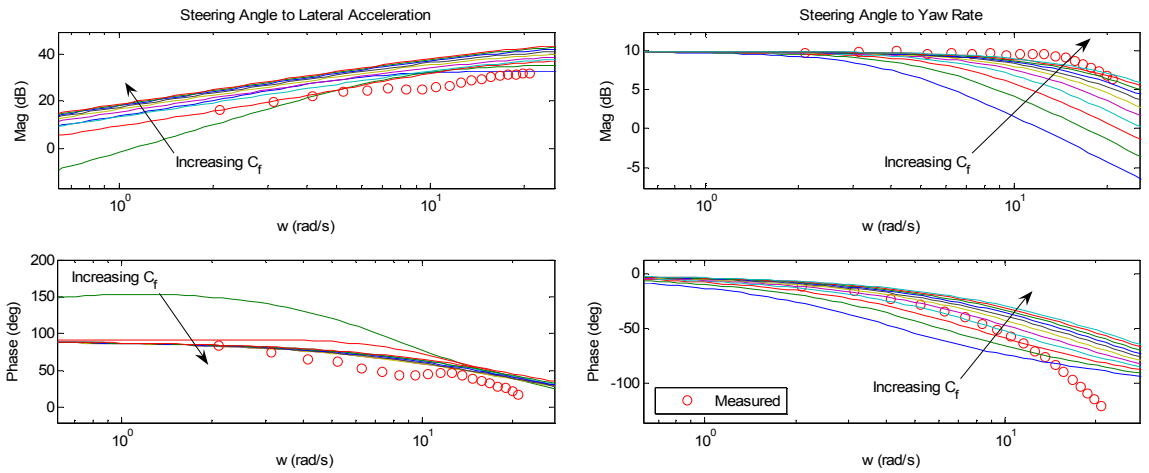

Figure **5.7**: Parametric Variation, C_f, Model 1, 8.9 m/s

From Figure **5.7**, the most apparent effect of the cornering stiffness values is that higher values result in a greater DC gain of the vehicles response in lateral acceleration and an increased bandwidth in the yaw rate response. It may be seen from Figure **5.7** that there is no particular set of cornering stiffness parameters that causes the models to match the measured output, particularly in the phase of the yaw rate response. For lateral acceleration, there is a match at low frequencies for a front cornering stiffness value of C_f = -40,950 N/rad (red), and a match at higher frequencies for a value of C_f = -50,050 (blue). Phase also seems to match fairly closely with all values of cornering stiffness above C_f = -31,850 N/rad (dark green). However, Model 1 does not show the drop in

both phase and magnitude that occurs at approximately 9 rad/s. This behavior would suggest the existence of unmodeled dynamics that are not included in the bicycle model.

Examination of the yaw response in Figure **5.7** shows significantly different results than the lateral acceleration response in regards to matching with the above cornering stiffness values. While it would initially appear that high cornering stiffness values match the measured data for the magnitude, none of them match the break frequency that occurs in the measured data at approximately 15 rad/s. Additionally, none of the variations matches the shape of the measured phase. Similar disagreement is seen in both lateral acceleration and yaw rate appear in the 16.5 m/s test shown in Figure **5.8**. The exception is that the front cornering stiffness value of C_f= -40,950 N/rad matches the magnitude of the yaw rate response very well.

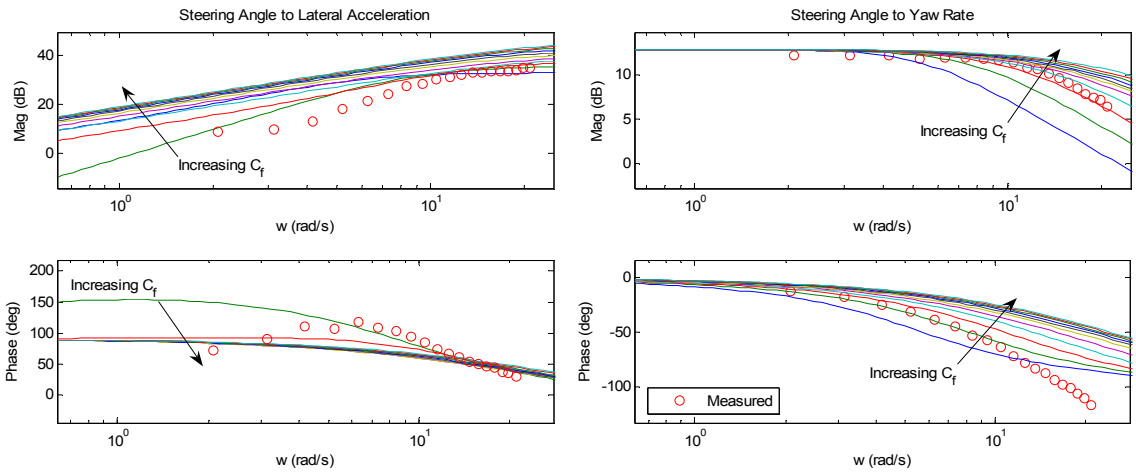

Figure **5.8**: Parametric Variation of C_f, Model 1, 16.5 m/s

In summary, a front cornering stiffness of C_f= -40,950 N/rad showed good matching at low frequencies for lateral acceleration in both magnitude and phase in the 8.9 m/s test. It also showed excellent matching in yaw response magnitude for all

frequencies tested at 16.5 m/s. Additionally, a front cornering stiffness of C_f= -50,050 N/rad showed good matching at high frequencies for both magnitude and phase in the 8.9 m/s test. Therefore, a front cornering stiffness value of C_f= -45,500 N/rad was chosen for further investigation, as it is a compromise between the two. Solving Eq. **5.10** gives a corresponding rear cornering stiffness of C_r = -75,560 N/rad. Figure **5.9** shows the predicted yaw response at 16.5 m/s using the parameters specified by Table **5.3**.

Table **5.3**: Parameters from initial bicycle model fit

Parameter	Value	Units
m	1,100	kg
Wf	6,339	N
Wr	3,781	N
I_{zz}	1,850	kg-m^2
lf	0.93	m
lr	1.56	m
Cf	-45,500	N/rad
Cr	-75,560	N/rad

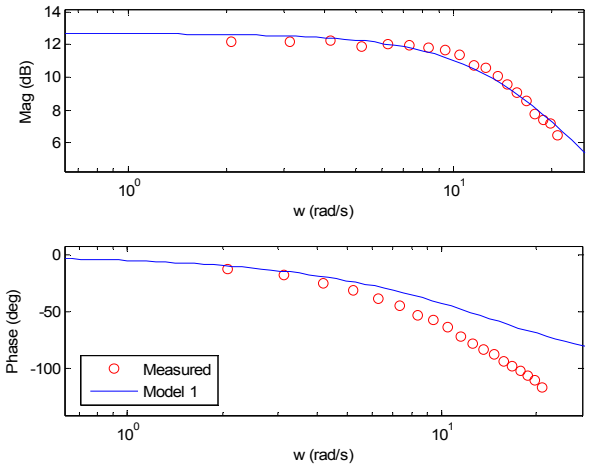

Figure **5.9**: Measured Frequency Response From Steering Angle to Yaw Rate, Model 1, 16.5 m/s, No Tire Lag

It has been shown in literature [5] that a delay effect occurs in tire force generation, a phenomenon known as tire lag. This effect is known to have a significant influence on the phase portion of the yaw rate response, whereby the vehicle exhibits more lag than predicted [5]. The measured experimental data in Figure **5.9** clearly exhibits more lag than is predicted by the bicycle model, suggesting that tire lag may be present. Tire lag is also known to be velocity dependent, i.e. the vehicle must travel a certain distance in order for the tire forces to reach steady state. The tire-lag phenomenon is commonly modeled as a first order system with zero steady-state gain and is introduced as a feed-forward term. Such a model is introduced in this study using a model described by:

$$\frac{\delta_f^*}{\delta_f} = \frac{1}{\tau \cdot s + 1} \qquad \textbf{5.11}$$

with δ_f being the steering input at the tire generated by the driver and δ_f^* being the effective steering input entering the bicycle model. Here τ is defined as:

$$\tau = \frac{D_{ss}}{U} \qquad \textbf{5.12}$$

where D_{ss} is the distance required for the tire to reach steady state. Note that τ is inversely proportional to forward velocity, and hence more noticeable for the relatively low-speed driving studied in this work (~30 mph).

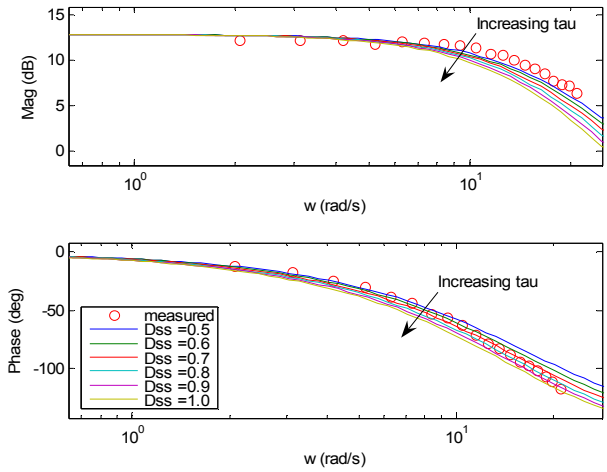

Figure **5.10**: Frequency Response From Steering Angle to Yaw Rate, Varying D_{ss}, Model 1, 16.5 m/s

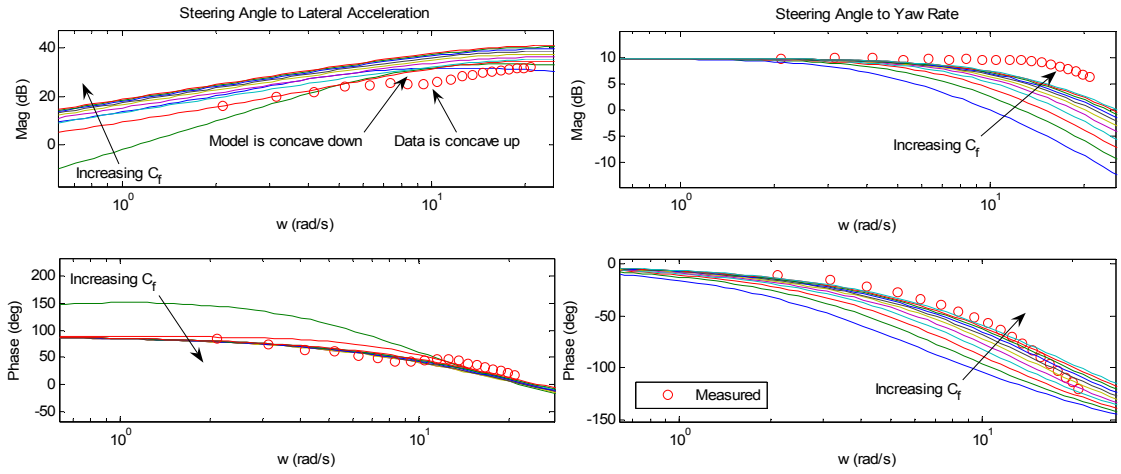

Figure **5.11**: Parametric Variation of C_f, model 1, 8.9 m/s, tire lag included

Typical values of D_{ss} in the literature are between 0.5m and 1m [5]. By varying the tire-lag dynamics of the bicycle model (Model 1) and utilizing the parameters specified in Table **5.3**, it was found that a value of 0.6m fit the measured data quite well in both magnitude and phase (Figure **5.10**). The above variations were repeated with the tire lag model in place and are shown in Figure **5.11**.

Examining the measured lateral acceleration response, the data in Figure **5.11** indicates that a front cornering stiffness value of -41,000 N/rad (red) matches reasonably well at both lower and higher frequencies for magnitude, with a slight overshoot in phase for lower and middle frequencies. Additionally, at approximately 10 rad/s Model 1 is slightly concave down, while the data is concave up. Such a drop in magnitude observed in the experimental data suggests that the energy is going into a different mode than just those included in Model 1 (the bicycle model), for example into roll.

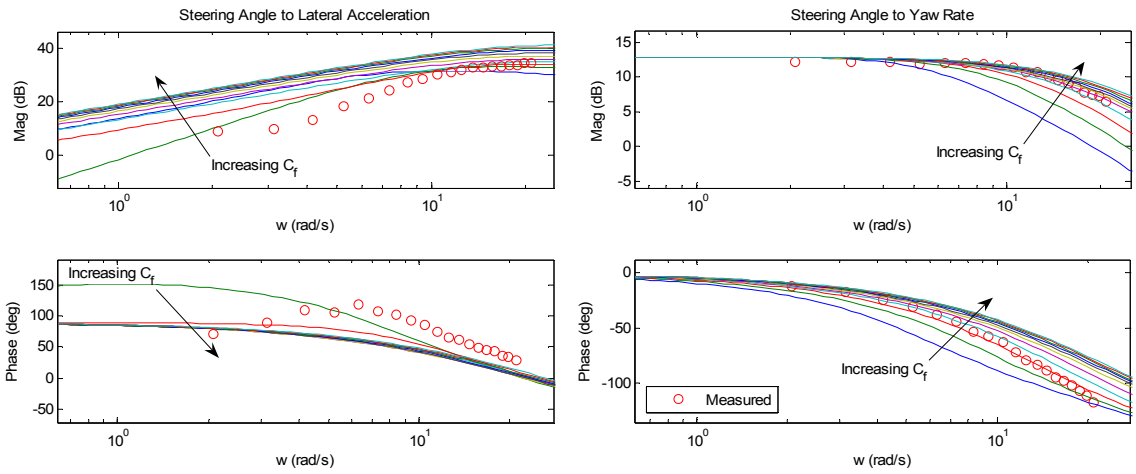

Figure **5.12**: Parametric Variation of C_f, Model 1, 16.5 m/s, Tire Lag Included

In contrast, this same value for C_f only matches at higher frequencies in Figure **5.12** in magnitude, and does not phase at any frequency. It also suggests that no variation of C_f will match the measured data taken at 16.5 m/s as well as it matches the data taken at 8.9 m/s for lateral acceleration.

A final observation taken from the 16.5 m/s test is that the measured data taken at frequencies slower than 8 rad/s does not appear to follow the general trend of the predicted response at all. While one possible cause of this is parametric uncertainty, it is

more likely that the error lies in the data itself. This effect is not readily apparent at lower speeds and is also completely repeatable among trials. Such conditions suggest that it is caused by a dynamic effect that is not being modeled.

The observed results for yaw rate are rather different. At 8.9 m/s, the same approximate value of C_f (again shown in red) shows very poor matching in both magnitude and phase. Additionally, all variations have significant error at mid- to high-range frequencies in magnitude. At 16.5 m/s, a C_f value of -41,000 N/rad matches the phase well, while a C_f value of -50,000 N/rad gives good matching in yaw magnitude.

In summary, while the addition of a tire lag model allowed for significantly better matching in the phase of the yaw response, the overall results were similar to the analysis performed without tire lag. As a result a front cornering stiffness value of C_f = -45,500 N/rad and a rear cornering stiffness value of C_r = -75550 N/rad were chosen as target values for further evaluation. All of the parameters obtained thus far are summarized in Table 5.4 and will be used to fit the roll models. The values for roll stiffness (K_φ) and roll damping (D_φ) are highlighted to indicate that they are initial estimates and will be allowed to vary.

Table 5.4: Parameters to be used in roll model fit

Variable	Value	Units		Variable	Value	Units
m	1030	kg		l_f	0.93	m
W_f	6339	N		l_r	1.56	m
W_r	3781	N		l	1.4	m
m_s	825	kg		h	0.52	m
I_{zz}	1850	kg-m^2		C_f	-45500	N/rad
I_{yy}	1705	kg-m^2		C_r	-76650	N/rad
I_{xx}	375	kg-m^2		K_φ	33000	N*m/rad
I_{xz}	72	kg-m^2		D_φ	1050	N*m*s/rad^2
K_{us}	0.045	rad/g				

5.2.2 Roll Model Fit – Manual Parametric Variation

Figure 5.13 shows the frequency response of Model 2. The parameters for this fit are defined in Table 5.4, with the roll stiffness and roll damping values determined experimentally in Section 5.1.2. While Figure 5.13 shows that the general trends of the roll models agree with Model 1, significant differences occur at the natural frequency of 10.2 rad/s at 8.9 m/s and 8.1 rad/s at 16.5 m/s. This frequency is shifted by about 2 rad/s between Model 4 and Models 2 and 3. This shift in frequency is a direct result of the assumption that the lateral tire forces are equal to the lateral acceleration of the vehicle, and is discussed in detail in Section 3.6.

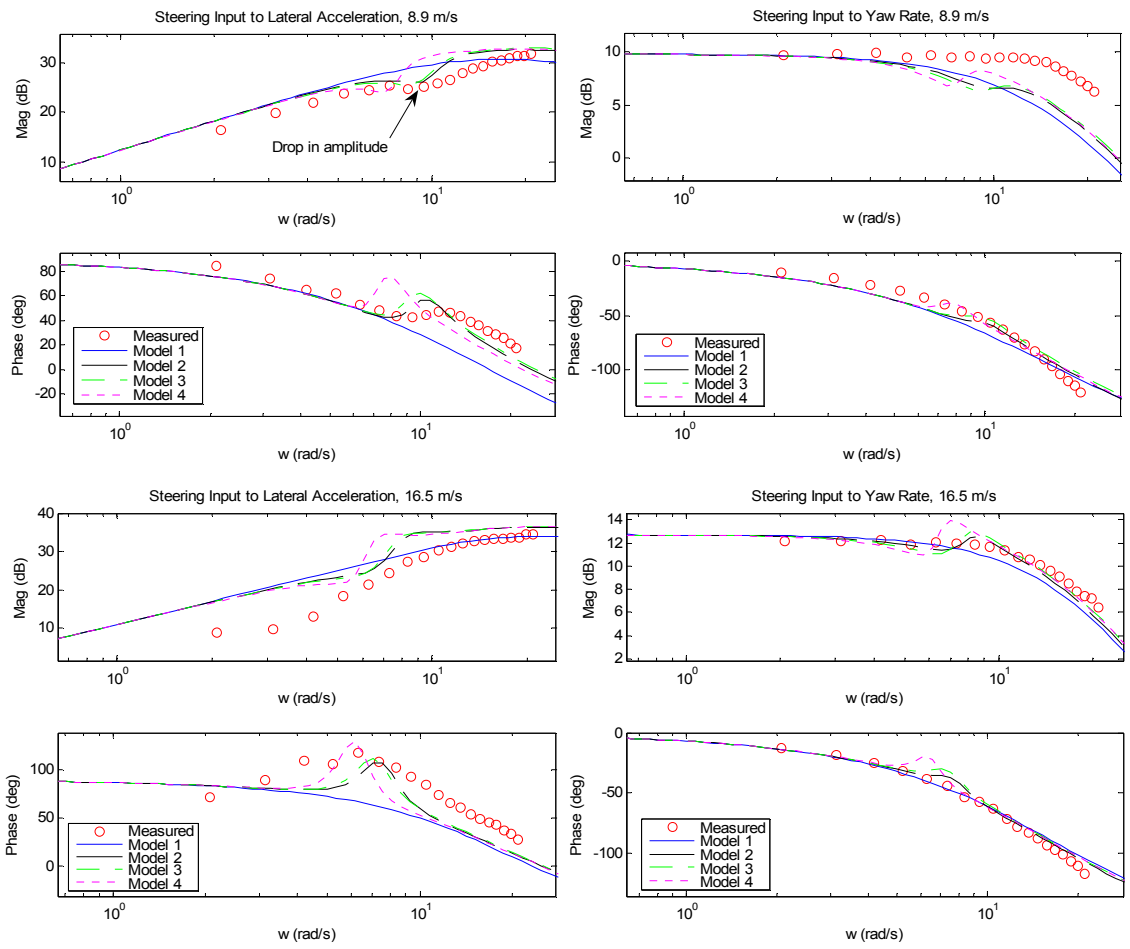

Figure **5.13**: Frequency Response Using Initial Values for Roll Parameters, Planar Dynamic Modes

As shown in Figure **5.13**, the lateral acceleration response at 8.9 m/s matches very well with the addition of roll dynamics. It also agrees with the observation made previously that there is a drop in the magnitude response not captured by Model 1 at approximately 9 rad/s. However, at 16.5 m/s, the shape of the measured response is not matched by any of the models, with significant model-data disagreement in both DC gain and natural frequency.

Further insight is obtained by examining the yaw response. While the models predict an underdamped response, the data in the 8.9 and 16.5 m/s trials indicate a response that is well damped. Aside from this discrepancy, the models match the phase well in both trials, match the magnitude well in the 16.5 m/s trial, and match the DC gain well in the 8.9 m/s trial. This matching combined with the likelihood of errors existing in the lateral acceleration data as discussed in Section **4.1.4.4** (i.e. axial cross-coupling and mechanical noise) suggests that errors may also exist in the values of roll stiffness and damping obtained experimentally.

Figure **5.14** shows a comparison in frequency response between the measured and predicted roll rate response at two speeds: 8.9 m/s and 16.5 m/s. In both trials, it is clear that the data indicates significantly more roll damping as well as a higher natural frequency than predicted by the model. Much like in the planar dynamic modes, Models 2 and 3 show similar responses, with Model 4 exhibiting a natural frequency approximately 2.5 rad/s lower. Model 4 also has a slightly greater gain and a more abrupt phase shift.

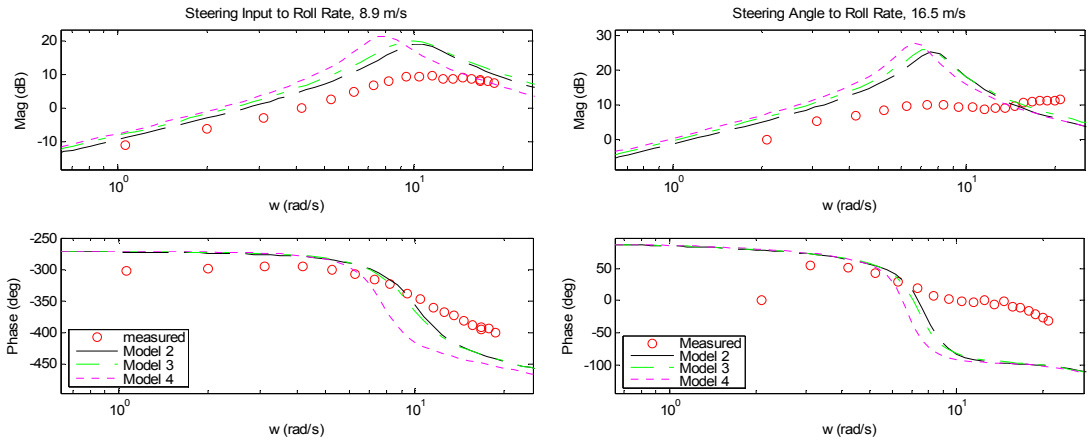

Figure **5.14**: Frequency Response Using Initial Values for Roll Parameters, Roll Rate

While differences exist between each of the roll models, they are not significant enough to show the individual effects of parametric variation on them here. Therefore for brevity, the remainder of this section will focus on Model 2 as it contains the most detailed description of the vehicles dynamics and closely matches the behavior of Model 3.

Figure **5.15** shows the response of Model 2 change as K_ϕ is varied from 25,000 N/rad to 70,000 N/rad in increments of 5,000 N/rad. Here it may be seen that while an increase in roll stiffness is required for good model fitting, the measured response peaks at different frequencies for each speed – 11.5 rad/s for the 8.9 m/s trial and 7.3 rad/s for the 16.5 rad/s trial. Considering this, the predicted response at 8.9 m/s with a roll stiffness of 60,000 N/rad (gold line) approximately matches the peak at 11.5 rad/s. In the 16.5 m/s trial, the peak occurring at 7.3 rad/s is approximately matched by a roll stiffness of 30,000 N/rad (dark green line).

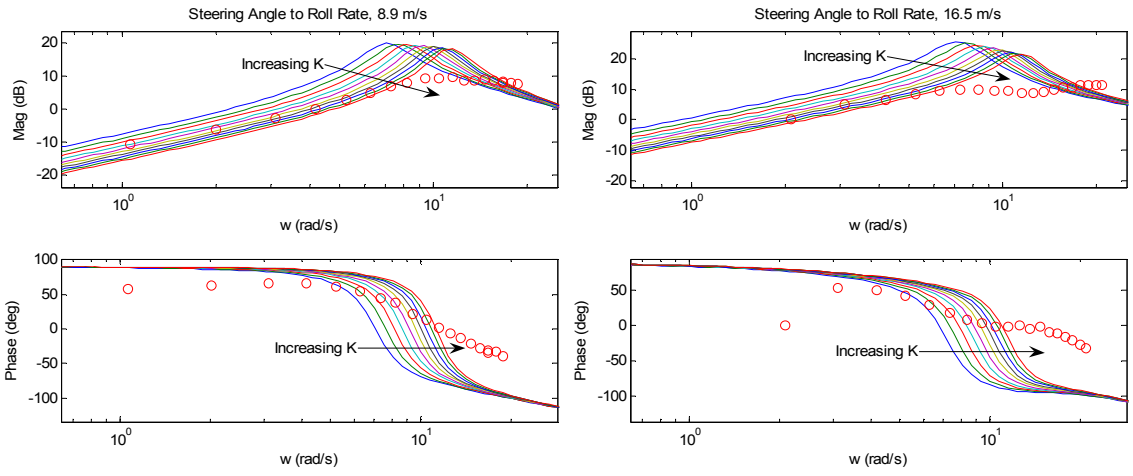

Figure **5.15**: Parametric Variation of K_ϕ, Model 2, Roll Rate

A similar discrepancy arises in regards to roll damping. In Figure **5.16**, D_ϕ is varied from 3,000 N-rad/s to 11,100 N-rad/s in 900 N-rad/s increments. Note that the lower bound was chosen based upon the above findings that the yaw response was very well damped. Here it is seen that the predicted response approximates the shape of the measured data in the 8.9 m/s trial with a roll damping of 3,900 N-rad/s (dark green line). For the 16.5 m/s data, a damping value of 8,400 N-rad/s (gold line) causes the predicted response to approximate the shape of the measured data.

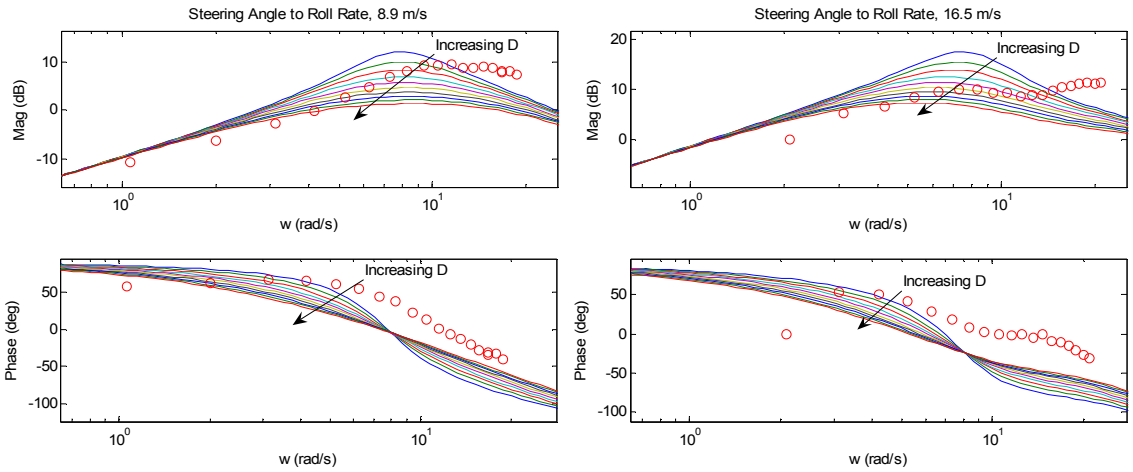

Figure **5.16**: Parametric Variation of D_ϕ, Model 2, Roll Rate

By examining Figure **5.15** and Figure **5.16** and considering all of the roll models, it was found that a roll stiffness of 53,000 N/rad and a roll damping rate of 6,000 N-rad/s provided a very good match for the roll rate of both trials. This fit is shown in Figure **5.16**. The only significant model-mismatch is seen in the 16.5 m/s trial, where the data begins to diverge from the predicted magnitude gain at approximately 13 rad/s, and the measured phase diverges from the predicted values at approximately 9.5 rad/s. The effect has been shown to be repeatable, and is believed to be a problem with data

collection and not with the individual models, as the behavior does not make physical sense. As a result of the preceding analysis, the final set of parameters was defined to be those listed in Table **5.5** and are used to create the lateral acceleration fits shown in Figure **5.18** and the yaw rate fits shown in Figure **5.19**.

Table **5.5**: Final Vehicle Simulation Parameters from Frequency Domain Fit

Variable	Value	Units	Uncertainty	How it was determined
m	1030	kg	5%	Measured
W_f	6339	N	5%	Measured
W_r	3781	N	5%	Measured
m_s	825	kg	5%	Model Fit[2]
I_{zz}	1850	kg-m^2	5%	Model Fit[1]
I_{yy}	1705	kg-m^2	5%	NHTSA database
I_{xx}	375	kg-m^2	5%	NHTSA database
I_{xz}	72	kg-m^2	5%	NHTSA database
l_f	0.93	m	5%	Measured[1]
l_r	1.56	m	5%	Measured[1]
l	1.4	m	5%	Measured1
h	0.52	m	5%	NHTSA database
K_φ	53000	N*m/rad	10%	Model Fit[2]
D_φ	6000	N*m*s/rad^2	10%	Model Fit[2]
C_f	-45500	N/rad	10%	Model Fit[2]
C_r	-76650	N/rad	10%	Model Fit[2]
K_{us}	0.045	rad/g	5%	Experimentally Determined

[1] - Indicates that the value is within 5% of the NHTSA database value.
[2] - Indicates that the value is not published in a readily available public database.

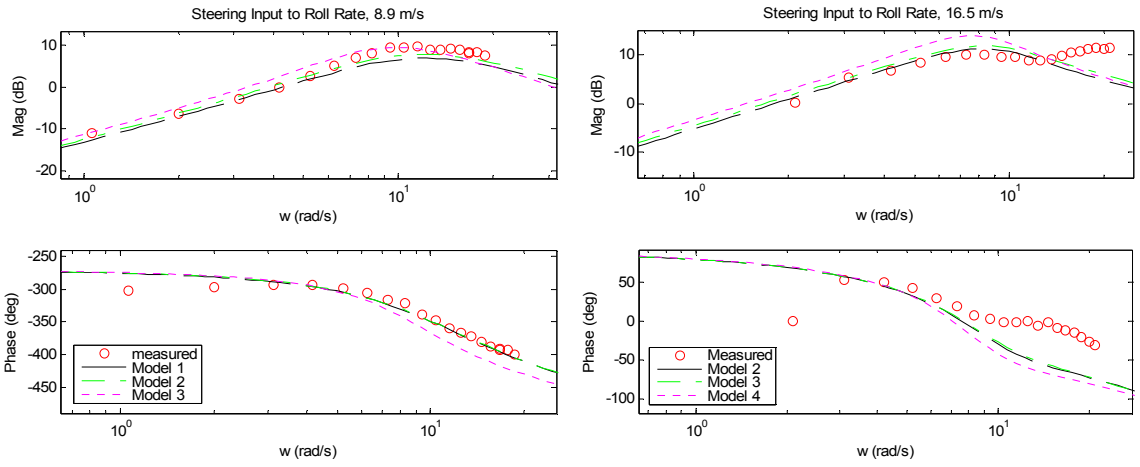

Figure **5.17**: Parametric Variation Results, Steering Angle to Roll Rate

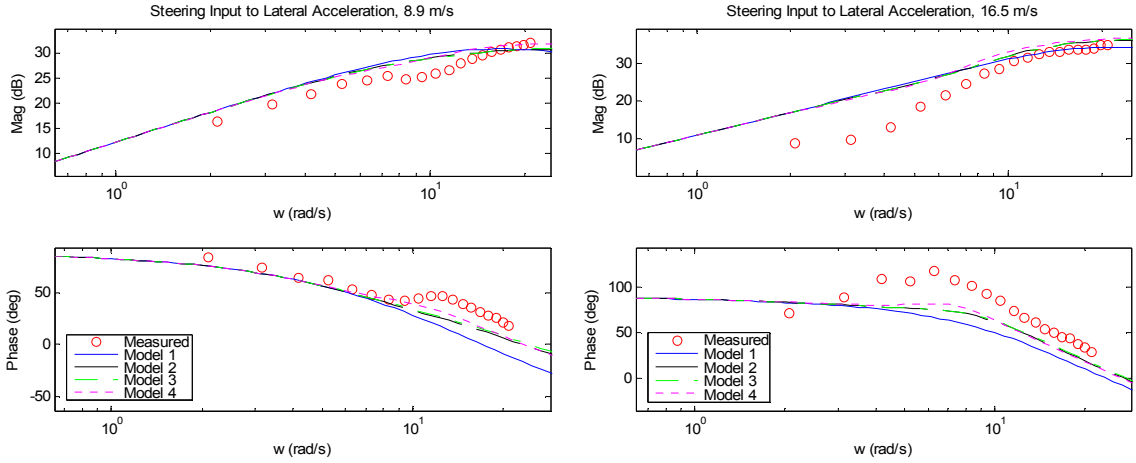

Figure **5.18**: Parametric Variation Results, Steering Angle to Lateral Acceleration

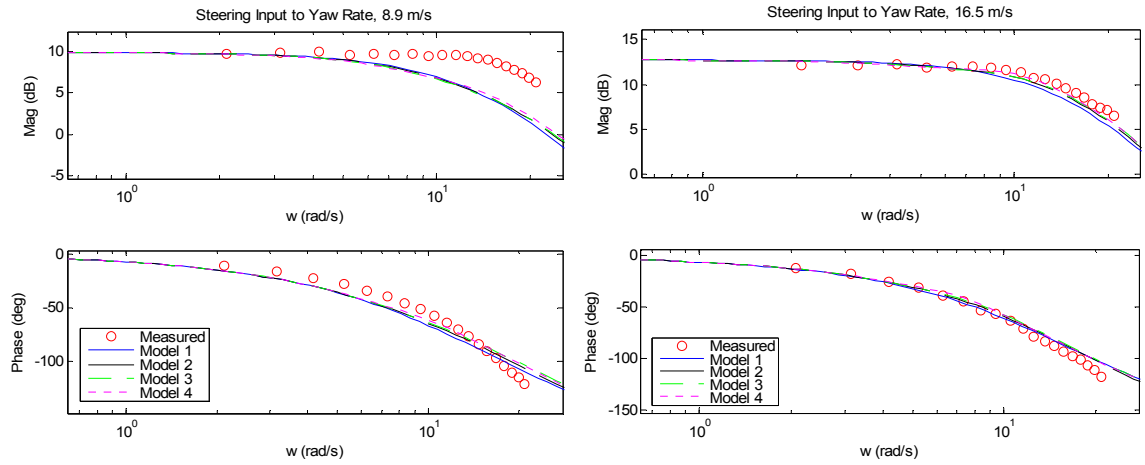

Figure **5.19**: Parametric Variation Results, Steering Angle to Yaw Rate

5.2.3 Investigation of Error in Lateral Acceleration Data

As mentioned in the previous section and detailed in Section **4.1.4.4**, it is hypothesized that the error in the frequency response data exhibited between the

predicted response and the measured response at lower frequencies primarily comes from either (1) a poor signal-to-noise ratio or (2) axial cross-coupling due to vehicle roll angle. These two effects will be studied below.

5.2.3.1 Investigation of the Effect of Poor Signal-to-Noise Ratio

The effect of sensor noise on the resulting data points is easily checked by inspection. Lateral acceleration data for the 5.25 rad/s data point (Figure **5.20**) and the 6.28 rad/s data point (Figure **5.21**) are shown below.

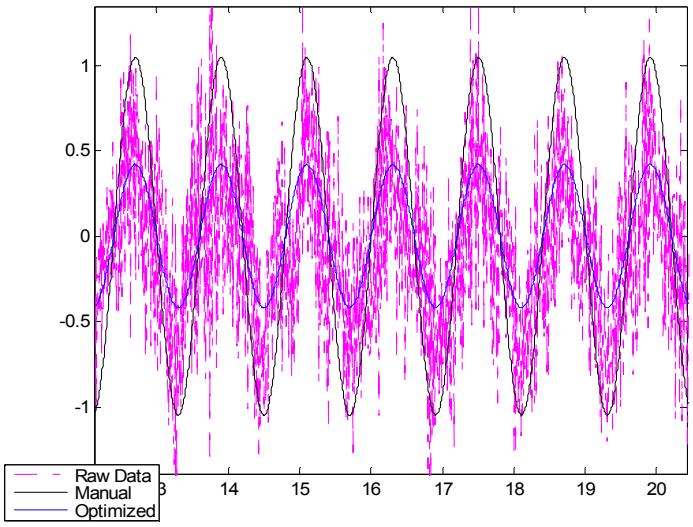

Figure **5.20**: Lateral Acceleration Data Segment, 5.25 rad/s

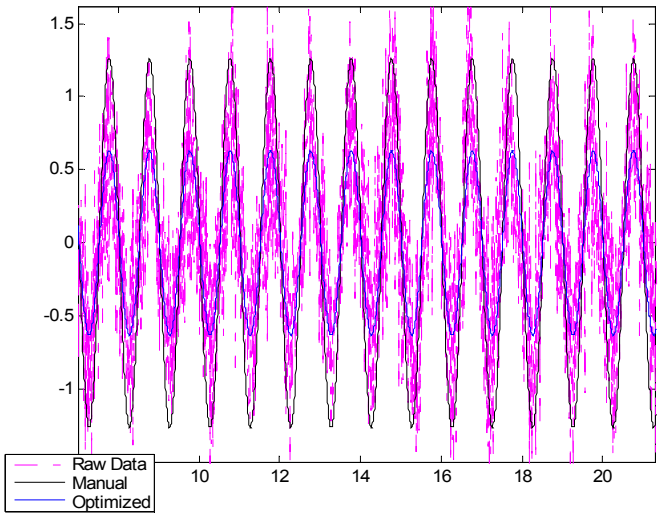

Figure **5.21**: Lateral Acceleration Data Segment, 6.28 rad/s

In both figures, the raw data is shown, with the fit obtained from the Simplex-based algorithm overlaid on top of it. It is clear that this cosine wave is generally correct in regards to frequency and phase, but the amplitude appears to be significantly lower than is indicated by the data. In the case of the data point at 1.05 rad/s, the actual data is nearly indistinguishable from the noise (Figure **5.22**).

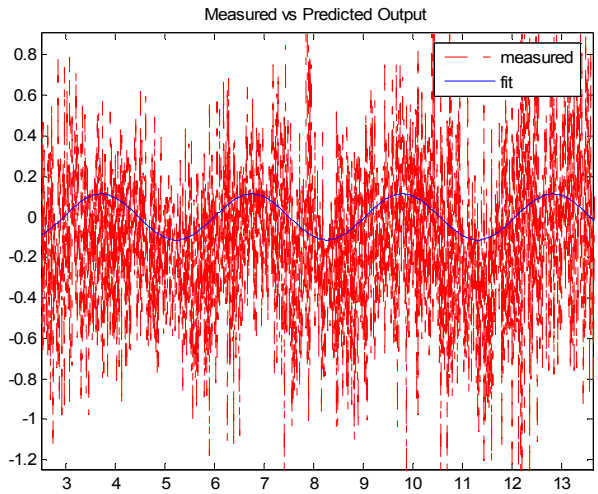

Figure **5.22**: Lateral Acceleration Data Segment, 1.05 rad/s

Since such an effect is not seen at higher frequencies where the lateral acceleration dynamics are more readily excited, it was therefore hypothesized that at lower frequencies the poor signal-to-noise ratio is indeed causing significant error in the amplitude portion of the measured response. A quick test of this hypothesis involved manually fitting the amplitude of the response for the data points between 4.2 rad/s and 9.4 rad/s, inclusive, and plotting the results. A side-by-side comparison between the simplex-based method and a simple manual amplitude fit is shown below in Figure **5.23**, with Figure **5.20** and Figure **5.21** showing examples of the manual fit performed on two specific data points.

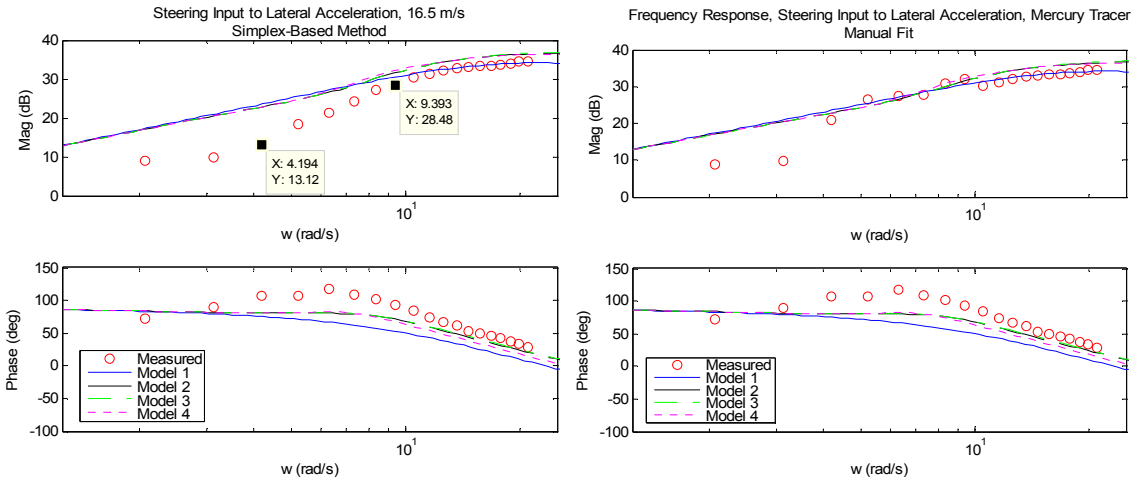

Figure **5.23**: Comparison Between Simplex-Based and Simplex-Based with Manual Amplitude Adjustment Methods.

While it is clear that the Simplex-based method is very sensitive to a poor signal-to-noise ratio, manually adjusting the amplitudes of the data points is neither repeatable nor practical. Therefore a more refined approach was developed. This method is outlined as follows:

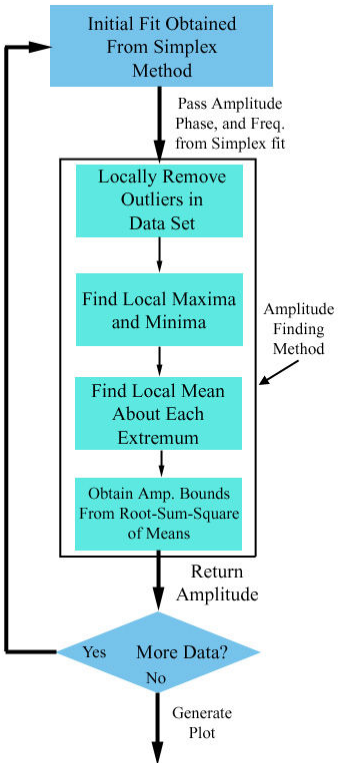

Figure **5.24**: Flow Chart, Custom Amplitude Solving Method

As indicated by the flow chart, the amplitude-finding function is called following the execution of the Simplex-based method. The frequency, phase, and amplitude obtained from the initial fit are passed to the amplitude-finding function along with the data set to be analyzed.

The first step the function performs is to traverse the data and remove outliers locally. An outlier is defined as a data point lying three or more standard deviations from the mean. If the current data point being considered is an outlier when compared to the surrounding data, its value is replaced by that of the previous data point. The decision to use the local mean and local standard deviation as opposed to global values was made as

a result of previous trials, where global values caused significant problems when considering sinusoidal.

The next step is to determine the location of each local maxima and minima in the data set. From the initial data supplied by the Simplex-based method, data is approximated by the function:

$$f(t) = a \cdot \cos(\omega \cdot t + \phi) \qquad \textbf{5.13}$$

where a is the initial amplitude, ω is the frequency, and φ is the phase angle. In order to find the approximate locations of the local maxima and minima, the derivative is taken to be:

$$\frac{df}{dt} = -\omega \cdot a \cdot \sin(\omega \cdot t + \phi) \qquad \textbf{5.14}$$

which is equal to zero when:

$$\omega \cdot t + \phi = n \cdot \pi \qquad \textbf{5.15}$$

where n is any positive integer. Solving for t, the location of the local maxima and minima in the data set may be found. This results in the equation:

$$t_{extrema} = \frac{(n \cdot \pi - \phi)}{\omega}, 0 \le t_{extrema} \le t_{\max} \qquad \textbf{5.16}$$

An example of the results of the function at this point is shown in Figure **5.25**. It is clear that the data about the extrema (indicated in red) may not necessarily be the true value of the peak or trough. Therefore the mean value about each point will be taken. The range taken into consideration is based upon the frequency of the sample, whereby

higher frequency data has a smaller search window and low frequency data has a larger one.

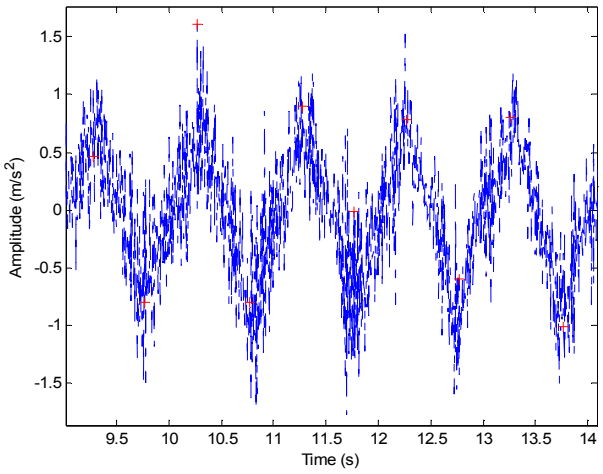

Figure **5.25**: Preliminary Results of Amplitude-Finding Function, 6.28 rad/s

$$t_{window} = \frac{0.25 \cdot \pi}{\omega} \qquad \textbf{5.17}$$

Using this data, positive and negative amplitude bounds were determined by taking the root-sum-square of the local means determined previously. The root-sum-square was used instead of the mean so as to weight data points of greater magnitude more than points of lesser magnitude. From these bounds, the amplitude of the cosine wave is readily determined.

As an example, the amplitude-finding method outlined above is applied to an example system defined by Eq. **5.18**, and the results are shown below in Figure **5.26**. Note that in the example system, the local extrema are located correctly and the upper and lower amplitude bounds (indicated by the black lines) correctly indicate unit amplitude.

$$\cos\left(6.28 \cdot t + 0.52\right) \qquad \textbf{5.18}$$

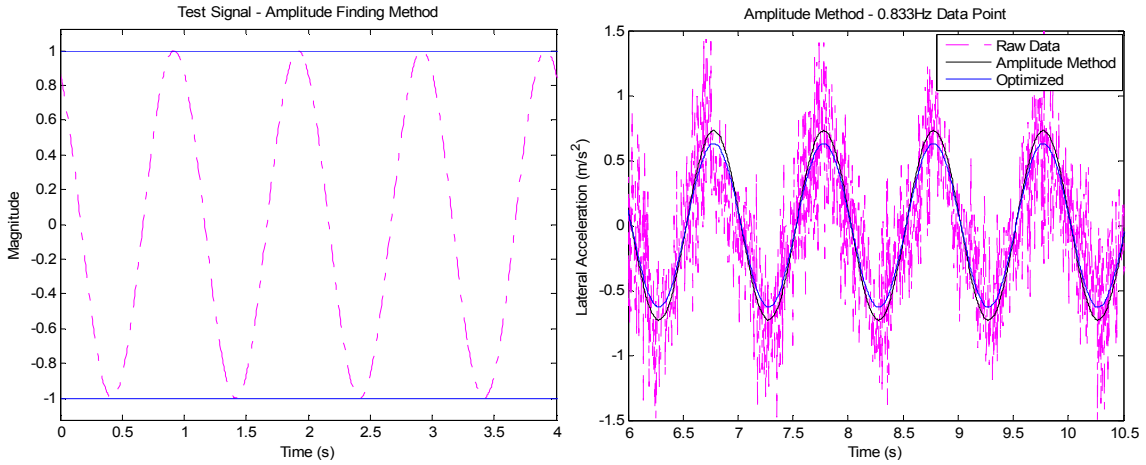

Figure **5.26**: Results of the Amplitude-Finding Method on Test Signal and 0.833Hz Data Point

Applying this method to the lateral acceleration frequency response, it is shown by Figure **5.27** that there is indeed an improvement in the matching of the data in the range attempted manually. It is also interesting to note that the amplitude-finding method has virtually no effect on the first two data points. This indicates that while the new method is indeed less sensitive to a low signal-to-noise-ratio, the quality of the low frequency data points is indeed poor and they should be discarded.

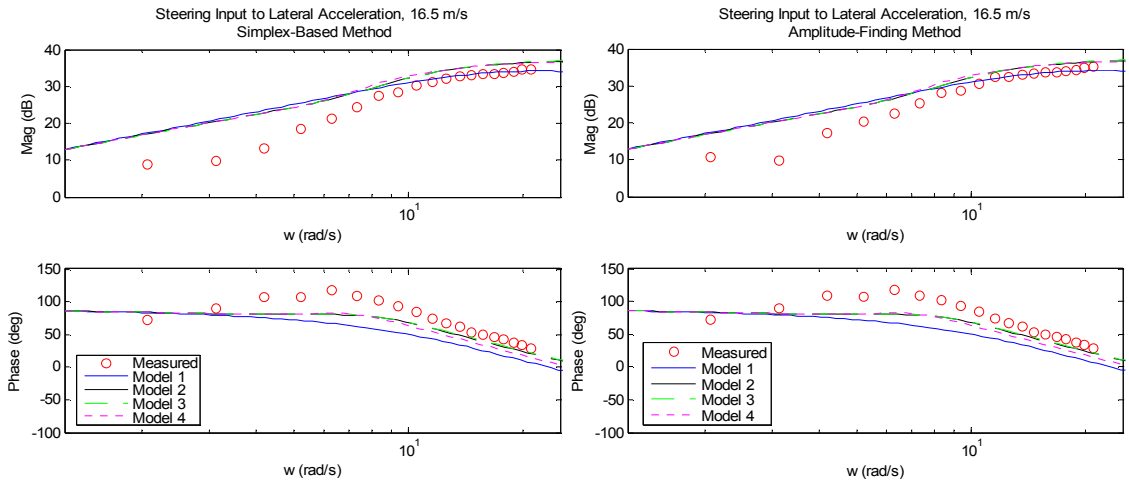

Figure 5.27: Results of the Amplitude-Finding Method on the Lateral Acceleration Response.

5.2.3.2 Investigation into the Effect of Axial Cross-Coupling

Further improvement may be found when investigating the effect of axial cross coupling on the measurements taken by the accelerometer. To illustrate this effect, a simulation was created to replicate the effect of a sensor being mounted above the roll axis, as is the case with the test vehicle. To accomplish this, a series of inputs having a frequency, amplitude, and phase equal to the data points in the above test were generated. Two outputs were then recorded – the model response (i.e. the response at the origin) and the response recorded by a sensor mounted above the roll axis.

After recording the outputs, the data was then processed using the Simplex-based method. Note that this method will return correct results when there is a high signal-to-noise ratio. In the case of the simulated outputs, there is no noise associated with the data. Additionally, Model 3 was used in this test due to its simplicity and accuracy in

modeling the measured roll rate of the vehicle. The results are shown below in Figure **5.28**.

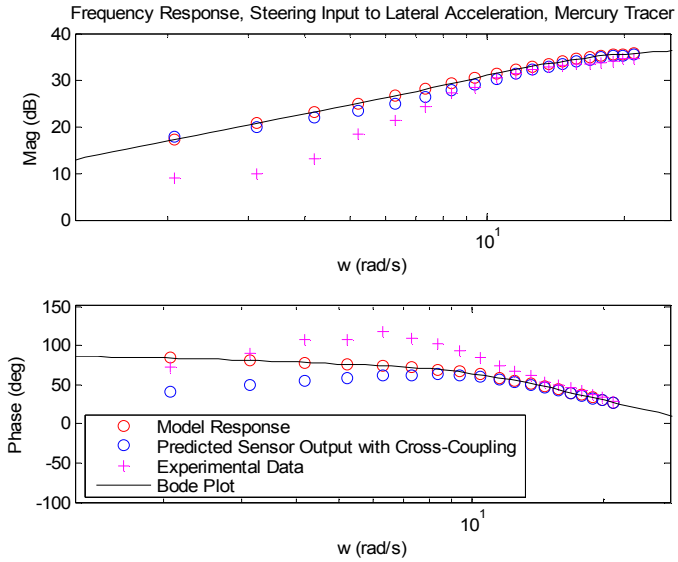

Figure **5.28**: Simulation Results for Axial Cross-Coupling Test.

While the effect of axial cross-coupling on the magnitude portion of the response is not very large, it has a clear effect on the phase of the response. By adding the difference between the model response and the predicted sensor output, a correcting vector may be obtained for both phase and magnitude so that the frequency response may be examined as if it had been taken without axial cross-coupling. Applying these corrections to the data obtained from the amplitude-finding method, a comparison between the original data and the corrected data shows significant improvement and is shown below in Figure **5.29**.

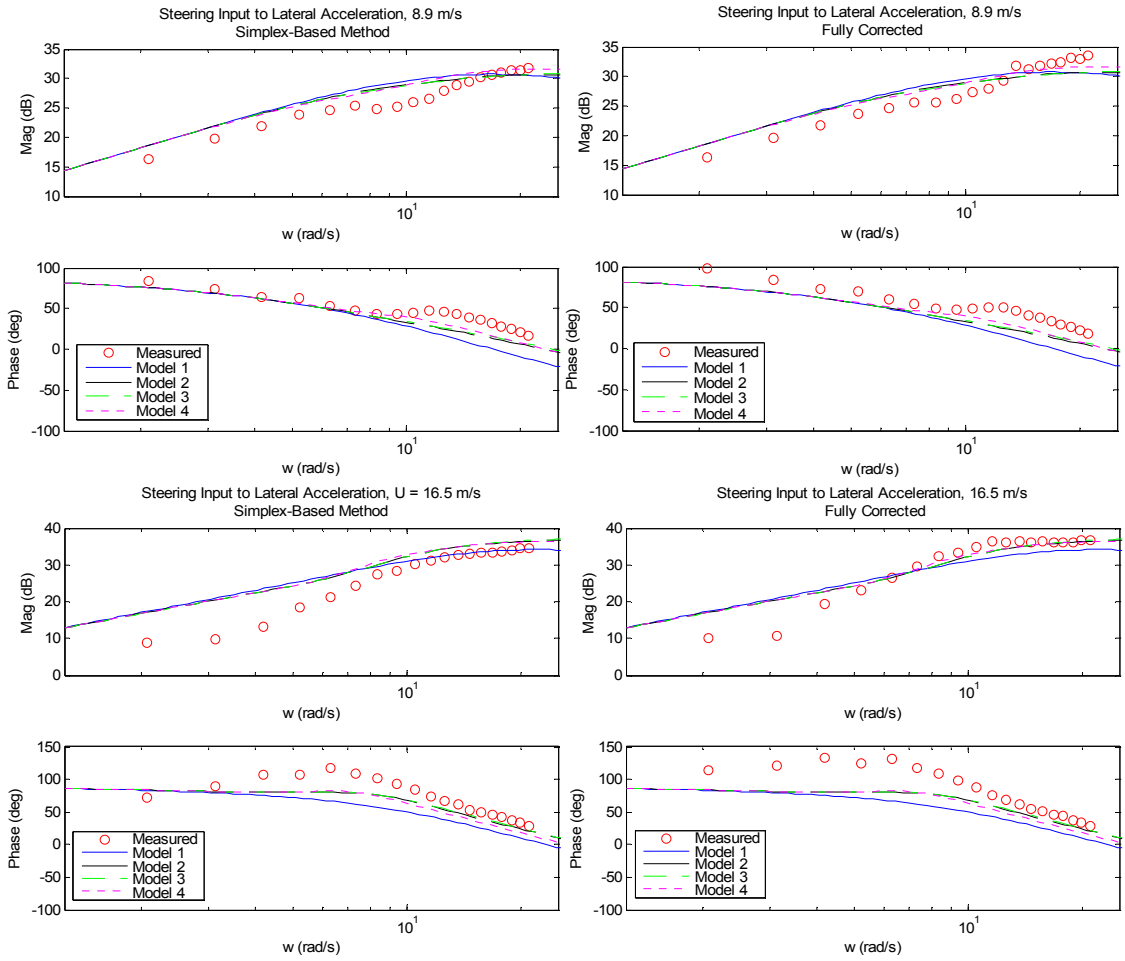

Figure **5.29**: Corrected Lateral Acceleration Response

Note that if the initial two data points are excluded, then the fit would be significantly better. This improvement will likely continue to increase as speed increases. This will not only cause the signal-to-noise ratio to drop as it is easier to excite the system dynamics, but the effect of vehicle roll angle on the sensor measurements will continue to increase. As a result of these findings, it is highly recommended that better sensors such as an IMU capable of determining the absolute roll, pitch, and yaw angles of the sensor, be obtained for future testing. Only in this manner can corrections be applied in real-time and are not model-dependent.

5.3 Time Domain Model Fitting

This section will detail the model fitting results in the time domain. First a discussion on the predictive capabilities of the models in the time domain will be given based on the parameters obtained from the frequency domain model fitting procedures. A new set of parameters will then be found by fitting the models in the time domain and examining the resulting fit in the frequency domain. The maneuvers chosen for analysis are a lane change and a step response, and were chosen as they are commonly used to validate models in literature [6-11].

5.3.1 Time Domain Results Utilizing Frequency Domain Fit Parameters

In order to obtain a more intuitive understanding of the model fit obtained by the frequency response tests, time response data was taken. The first maneuver performed was a step response (Figure **5.30**). The vehicle was driven forward at a constant speed of 8.9 m/s for an unspecified period of time. A step input of approximately 0.095 rad front wheel angle was then executed and the resulting vehicle response was recorded. Note that, due to the current limitations in data collection, the roll rate data was obtained during a separate trial, and thus has a slightly different steering command associated with it.

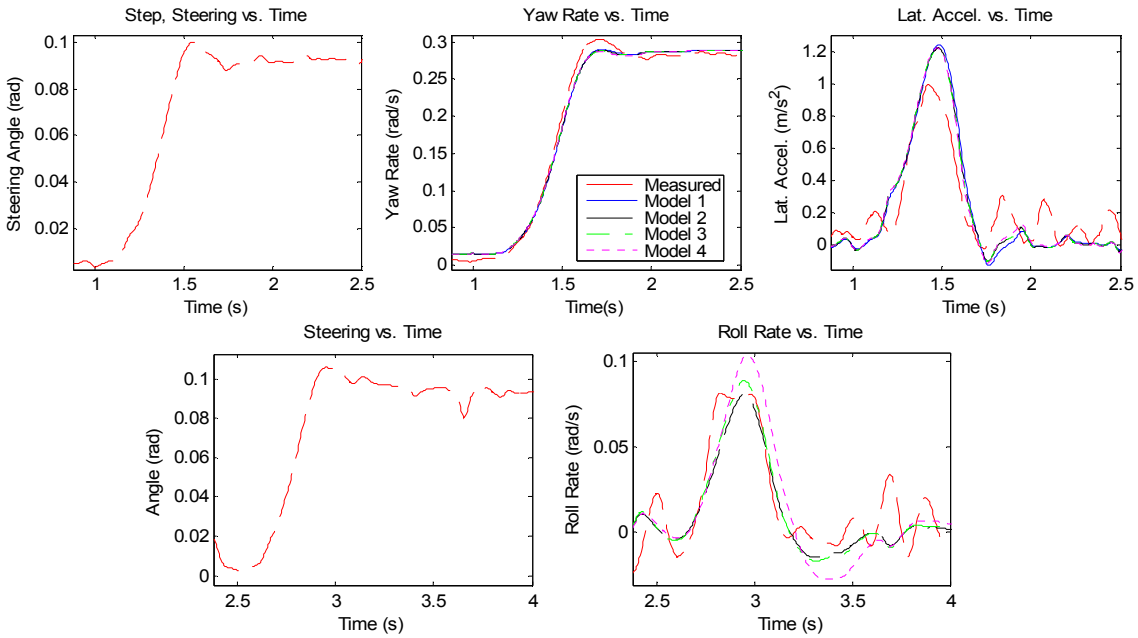

Figure **5.30**: Step Response, Mercury Tracer, 8.9 m/s, Frequency Domain Fit Parameters

The predicted yaw response of all of the models is nearly identical and matches the measured response well. The lateral acceleration response is also similar to the trends seen in the frequency response data, with all of the models producing a response of greater magnitude than the measured response. Some phase error can also be seen in lateral acceleration. The roll rate matches reasonably well, with the predicted magnitude of Model 2 matching the measured peak, Model 3 exceeding it by 11% and Model 4 by 31%. Additionally, Model 4 appears to have less damping than Models 2 and 3.

The next time-domain experiment was a lane change maneuver whereby the vehicle moved from the right lane to the left lane, and then back to the right lane (Figure **5.31**). To conduct this test, the vehicle was brought up to a constant speed of 17.8 m/s and was made to follow a reference line specifying the maneuver painted on the

test track surface. The results from the lane change maneuver were similar to those from the step response maneuver.

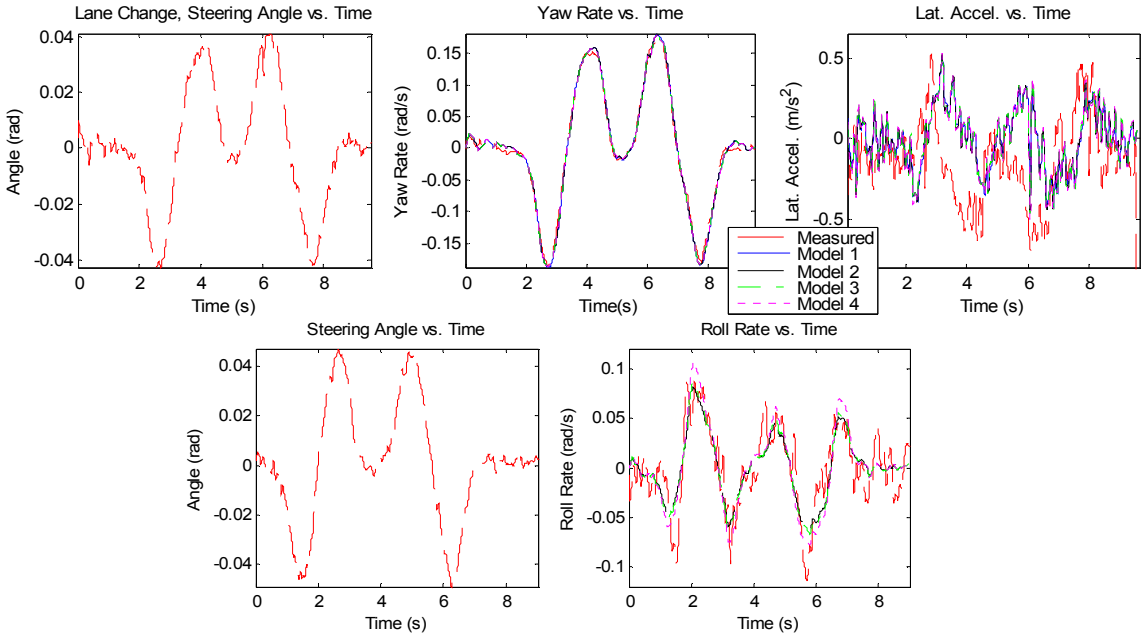

Figure **5.31**: Lane Change, Mercury Tracer, 17.8 m/s, Frequency Domain Fit Parameters

The yaw response again matches well. The roll rate response is also reasonable for all of the models, with Model 4 again appearing to be less damped than Models 2 and 3 and showing increased magnitude in the response. This is again likely due to the massless frame assumption.

There is poor model matching observed again in lateral acceleration, and this is far more evident with the lane change maneuver. Much like the frequency response data for this state, there is a mismatch in both the magnitude and phase of the data. As stated previously, this is likely due to influence of gravity on the lateral accelerometer as a result of vehicle roll angle, mechanical noise, and slight speed variations influencing the correction factor to change the measurements from global to body-fixed coordinates.

5.3.2 Model Fitting Using Time Domain Data

In the previous tests, it was shown that the time response data agreed with the findings of the frequency response data. Such an observation is expected, as the frequency domain represents the response of a plant to the complete range of inputs that it will encounter. However, many (if not most) vehicle chassis dynamic models are fit in the time domain. The question as to whether model fitting in the time domain gives a better fit than model fitting in the frequency domain was then posed.

In an attempt to answer this, the models were fit to the time response data shown above using manual parametric variation. The values obtained are listed in Table 5.6, with the resulting step response fit shown in Figure 5.32 and the lane change maneuver in Figure 5.33.

Table 5.6: Parameters Obtained from Time Domain Model Fitting

Parameter	Value from Time Domain Fit	Value from Frequency Domain Fit
C_f	-22,750 N/rad	-45,500 N/rad
C_r	-19,958 N/rad	-75,563 N/rad
K_φ	38,000 N/rad	53,000 N/rad
D_φ	5,000 N-s/rad	6,000 N-s/rad

At first glance, it would appear as if the parameters found are good matches comparable to those obtained in the frequency domain fits of Figures 5.17 - 5.19 (whose time-domain fits are shown in Figures 5.30 - 5.31), with the exception that the predicted step response is slightly slower than the measured. However, the model parameters identified in the time domain show poor matching in the frequency domain.

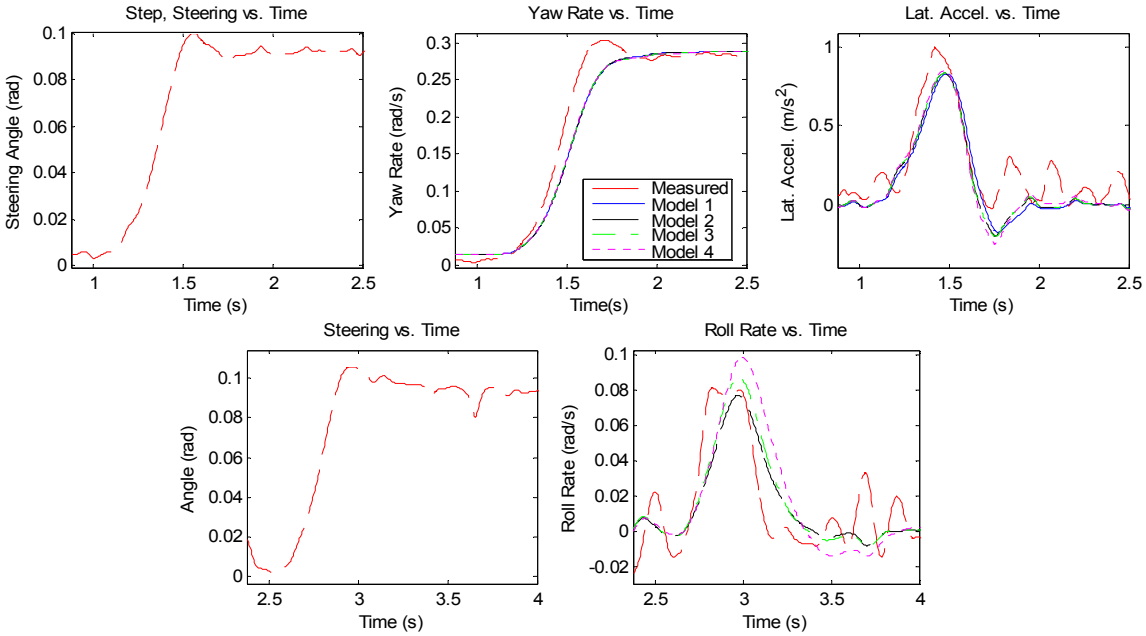

Figure **5.32**: Step Response, Mercury Tracer, 8.9 m/s, Time Domain Fit Parameters

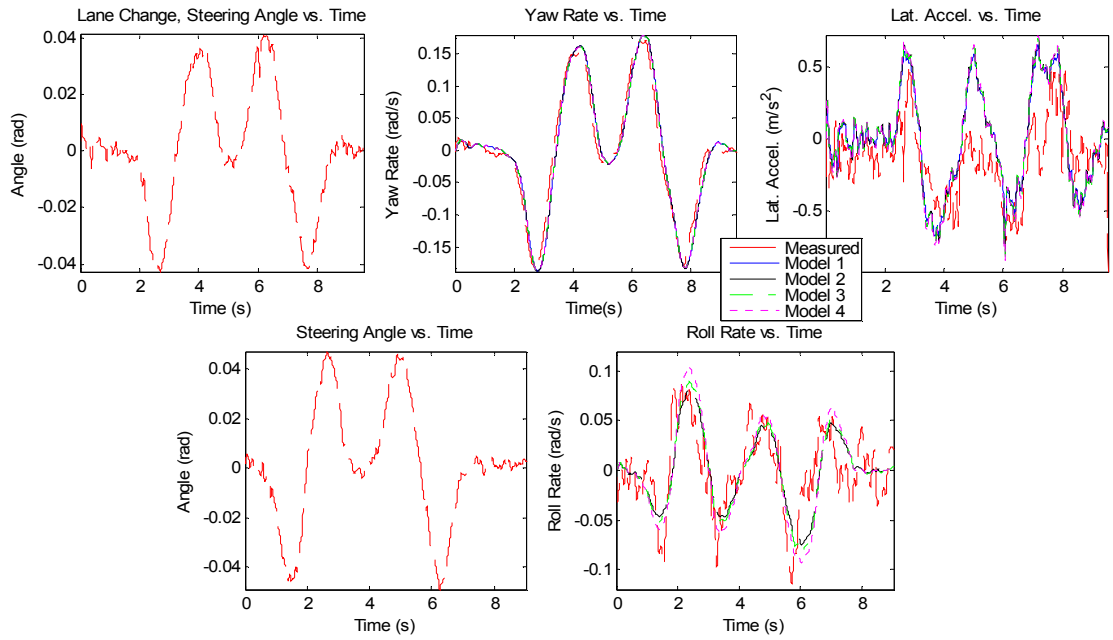

Figure **5.33**: Lane Change, Mercury Tracer, 17.8 m/s, Time Domain Fit Parameters

Figures **5.34** - **5.36** show that these parameters result in poor model matching in all of the states in the 16.5 m/s trial. Additionally, with the exception of the lateral acceleration magnitude, there is slightly worse matching with the 8.9 m/s trial data as well. This suggests a serious shortcoming of using time response data for model validation, as it might appear that not all of the input frequencies are excited in a single maneuver. It is yet unclear as to whether time domain signals intentionally made rich in frequency content, e.g. chirp inputs, work better. Again, these tests are ongoing.

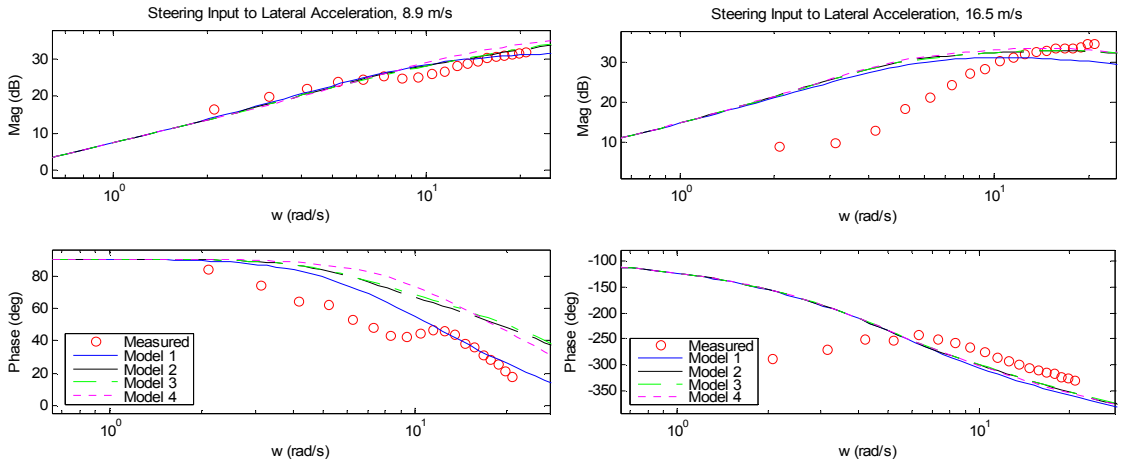

Figure **5.34**: Frequency Response, Steering Input to Lateral Acceleration, Time Domain Fit Parameters

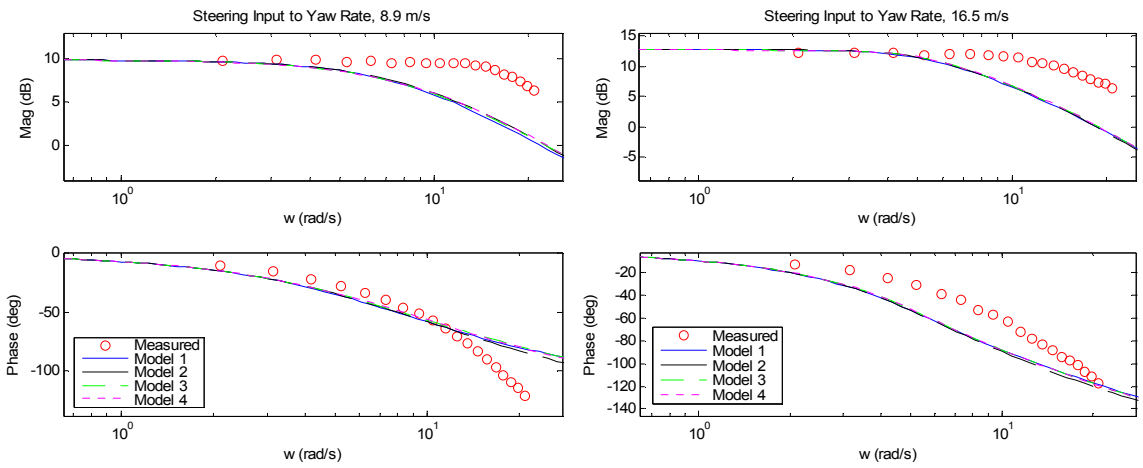

Figure **5.35**: Frequency Response, Steering Input to Yaw Rate, Time Domain Fit Parameters

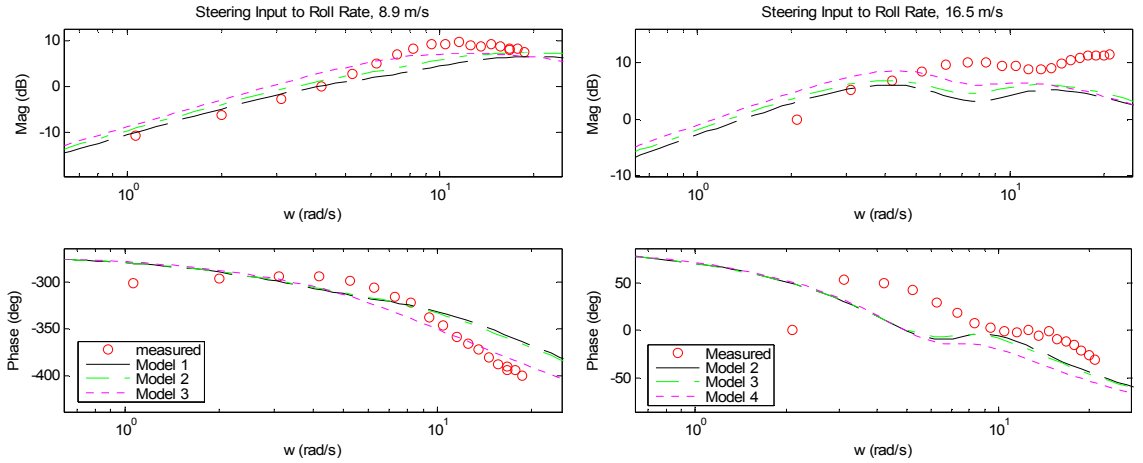

Figure **5.36**: Frequency Response, Steering Input to Roll Rate, Time Domain Fit Parameters

5.4 Concluding Remarks on Model Fitting Results

Experimental results indicate that some models might appear to be a slightly better match than others, but that model-to-model differences are largely secondary to questions of whether fits should be obtained in time or frequency domains. The results indicate that in the absence of frequency response data, extra care must be taken when attempting to determine vehicle parameters against time response data since system excitation may not be sufficient, even with step-response inputs. Future work will examine the use of other time response maneuvers such as the chirp response and the standard NHTSA maneuvers to determine the reliability of model fitting against these when compared to model fitting in the frequency domain.

In light of the model fitting results, Model 3 will be used for the control analysis in the remainder of this work. While Model 2 shows slightly better model matching capabilities, the differences are negligible when compared to the added simplicity of Model 3. Such a tradeoff is found in other works as well, such as in the case of the work by Huang et. al. [12]. While Model 4 is again simpler than Model 3, its reduced model matching capabilities as a result of its simplifying assumptions make it a poorer candidate for controller synthesis.

[1] G. J. Heydinger, R. A. Bixel, W. R. Garrott, M. Pyne, J. G. Howe, and D. A. Guenther, "Measured Vehicle Inertial Parameters - NHTSA's Data Through November 1998," *Society of Automotive Engineers*, 1999.

[2] J. C. Dixon, *Tires, Suspension, and Handling*, 2nd ed. Warrendale, PA: The Society of Automotive Engineers (SAE), 1996.

[3] J. Ryu, E. J. Rossetter, and J. C. Gerdes, "Vehicle Sideslip and Roll Parameter Estimation using GPS," presented at AVEC 2002: 6th International Symposium on Advanced Vehicle Control, Hiroshima, Japan, 2002.

[4] G. J. Heydinger, M. K. Salaani, W. R. Garrott, and P. A. Grygier, "Vehicle dynamics modelling for the National Advanced Driving Simulator," *Proceedures of the Institution of Mechanical Engineers Part D: Automobile Engineering*, vol. 216, pp. 307-318, 2002.

[5] G. J. Heydinger, W. R. Garrott, J. P. Chrstos, and D. A. Guenther, "Dynamic Effects of Tire Lag on Simulation Yaw Predictions," *Journal of Dynamic Systems, Measurement and Control, Transactions of the ASME*, vol. 116, pp. 249-256, 1994.

[6] B.-C. Chen and H. Peng, "A Real-time Rollover Threat Index for Sports Utility Vehicles," presented at Proceedings of the 1999 American Control Conference, San Diego, California, 1999.

[7] B.-C. Chen and H. Peng, "Rollover Prevention for Sports Utility Vehicles with Human-In-The-Loop Evaluations," presented at Proceedings of the 5th International Symposium on Advanced Vehicle Control (AVEC), Ann Arbor, Michigan, 2000.

[8] K. Kitajima and H. Peng, "Control for Integrated Side-Slip, Roll, and Yaw Controls for Ground Vehicles," presented at Proceedings of the 5th International Symposium on Advanced Vehicle Control (AVEC), Ann Arbor, Michigan, 2000.

[9] S. Kueperkoch, J. Ahmed, A. Kojic, and J.-P. Hathout, "Novel Vehicle Stability Control Using Steer-by-Wire and Independent Four Wheel Torque Distribution," presented at Proceedings of IMECHE, Washington, D.C., 2003.

[10] S.-W. Oh, H.-C. Chae, S.-C. Yun, and C.-S. Han, "The Design of a Controller for the Steer-by-Wire System," *JSME International Journal, Series C*, vol. 47, pp. 896-907, 2004.

[11] S. Takano, M. Nagai, T. Taniguchi, and T. Hatano, "Study on a vehicle dynamics model for improving roll stability," *Japanese Society of Automotive Engineers Review*, vol. 24, pp. 149-156, 2003.

[12] J. Huang, J. Ahmed, A. Kojic, and J.-P. Hathout, "Control Oriented Modeling for Enhanced Yaw Stability and Vehicle Steerability," presented at Proceedings of the American Control Conference, Boston, Massachusetts, 2004.

Chapter 6

Rollover Prevention Methods by a Steer-by-Wire System

The preceding sections have shown that the model presented by Kim and Park [1] (Model 3) is capable of accurately modeling both the planar and roll dynamics of a vehicle for moderate maneuvers. Additionally, given its low order and simplicity, the model is also well suited for control synthesis. This chapter will focus on using Model 3 to investigate control strategies to mitigate untripped single-vehicle rollover.

The chapter is organized as follows: the first section will develop a methodology to determine whether or not a vehicle is likely to slide prior to rollover. In the event that the vehicle will roll prior to sliding, the approximate speed and input frequency to induce such a condition will be reported. The second and third sections will respectively explore open-loop filtering techniques and closed-loop control methods for rollover prevention. These methods will be developed under the assumption that they are being implemented in a vehicle utilizing a steer-by-wire system.

6.1 A Method for Determining the Existence of a Slide-Before-Roll Condition

When examining a vehicle's dynamics in an emergency evasive maneuver on a flat roadway with no external collisions, three possible events may occur. The first and most desirable is that the situation is dealt with safely, with the driver maintaining complete control of the vehicle and avoiding the obstacle. The second is less desirable,

where the tires saturate and begin to slide at some point in the emergency maneuver. When this occurs, the driver can lose control over the vehicle and may not be able to effectively deal with the situation. The third possible event, possibly preceded by tire saturation, is when the vehicle rolls over during the evasive maneuver. Rollover is by far the worst possible event that could occur since the possibility of survival is the lowest.

In the following analysis, the last two possible events will be investigated. While it is impossible to determine a priori a driver's emergency response, road conditions, vehicle setup, etc., it is possible using linear analysis and simple assumptions to determine if the vehicle is likely to slide before it rolls. Such an approach is of critical importance, as it allows for the off-line determination of a vehicle's propensity to rollover in a dynamic situation. Since the method is off-line, it avoids the extensive trial-and-error experimentation currently performed by NHTSA and others.

Development of the wheel-lift prediction method is outlined as follows:

1. Find the dynamic relationship between steering angle and tire slip.
2. Using the results from (1) and knowledge of nonlinear tire behavior, determine the steering angle at which tire saturation occurs as a function of input frequency
3. Solve for the dynamic relationship between steering angle and roll moment induced by the suspension.
4. Combining the results from (2) and (3), the roll moment acting on the vehicle at the point of tire saturation may be solved for as a function of input frequency.
5. Determine a roll moment threshold for wheel-lift by performing a force balance on the wheels.

6. Apply this limit to (4) and determine at what speed the vehicle crosses this threshold.
7. Alternatively, use the results from (3) and (5) to determine the minimum steering angle at which wheel lift occurs.
8. Compare the steering angle at which the tires saturate (2) to the steering angle at which the wheels lift (7) as a function of frequency. This will indicate when wheel-lift is likely to occur before tire saturation.

The first step to determine whether or not a vehicle will slide before rolling is to examine the dynamic input-output relationship between steering angle and tire slip angle. Recall the definitions for front and rear slip angle used in Model 3, where:

$$\alpha_f = \delta_f - \frac{V + l_f r}{U} + \frac{\partial \alpha_f^*}{\partial \phi}\phi \qquad \textbf{6.1}$$

defines the slip angle of the front tire and:

$$\alpha_r = \frac{l_r r - V}{U} + \frac{\partial \alpha_r^*}{\partial \phi}\phi \qquad \textbf{6.2}$$

defines the slip angle of the rear tire. The transfer functions for steering input to front and rear tire slip may be readily found using the standard state-space to transfer function formula:

$$\frac{Y(s)}{U(s)} = c \cdot (s \cdot I - A)^{-1} \cdot b + d \qquad \textbf{6.3}$$

which is derived from the standard state-space representation described by:

$$\begin{aligned} \dot{x} &= A \cdot x + b \cdot u \\ y &= c \cdot x + d \cdot u \end{aligned} \qquad \textbf{6.4}$$

The plant description *A* and the input vector *b* may be found in Appendix **A.2**. The output vector *c* and the feedthrough vector *d* are obtained by examining Eq. **6.1** and Eq. **6.2**. For the front slip angle, the output equation is defined as:

$$y_{\alpha_f} = \begin{bmatrix} -\frac{1}{U} & -\frac{l_f}{U} & \frac{\partial \alpha_f^*}{\partial \phi} & 0 \end{bmatrix} \cdot \begin{bmatrix} V \\ r \\ \phi \\ \dot{\phi} \end{bmatrix} + [1] \cdot \delta_f \qquad \textbf{6.5}$$

Similarly, the output equation for the rear slip-angle is defined as:

$$y_{\alpha_r} = \begin{bmatrix} -\frac{1}{U} & \frac{l_r}{U} & \frac{\partial \alpha_r^*}{\partial \phi} & 0 \end{bmatrix} \cdot \begin{bmatrix} V \\ r \\ \phi \\ \dot{\phi} \end{bmatrix} + [0] \cdot \delta_f \qquad \textbf{6.6}$$

The magnitude portion of the bode plots of the resulting transfer functions are shown below. Figure **6.1** and Figure **6.2** compare the response of the bicycle model, Model 3, and Model 3 without the influence of roll steer for the front tire and rear tires, respectively, at 16.5 m/s. Here the effect that both roll dynamics and roll steer have on the tire slip, and hence the force generating abilities of the tires, may be seen. It should be noted that the effect of roll steer on vehicle response could not readily be seen when examining the vehicle states of lateral velocity, lateral acceleration, yaw rate, roll rate, or roll angle. Figure **6.3** and Figure **6.4** show the bode plots of steering input to front and rear slip angle as speed is varied. Unless otherwise noted, the parameters used to generate the proceeding graphs are for the 1996 Mercury Tracer test vehicle. These are shown below in Table **6.1** for reference.

Table **6.1**: Vehicle Parameters for 1996 Mercury Tracer

Variable	Value	Units	Variable	Value	Units
m	1030	kg	l	1.4	m
m_s	825	kg	h	0.52	m
I_{zz}	1850	kg-m^2	C_f	-45500	N/rad
I_{xx}	375	kg-m^2	C_r	-76650	N/rad
I_{xz}	72	kg-m^2	K_φ	53000	N*m/rad
l_f	0.93	m	D_φ	6000	N*m*s/rad
l_r	1.56	m			

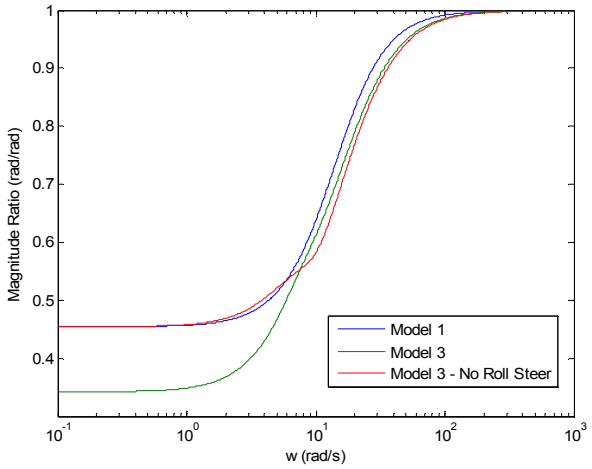

Figure **6.1**: Magnitude Response of Steering Input to Front Slip Angle, 16.5 m/s

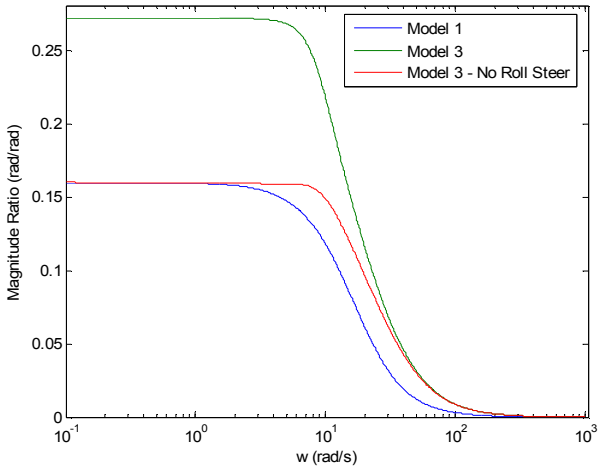

Figure **6.2**: Magnitude Response of Steering Input to Rear Slip Angle, 16.5 m/s

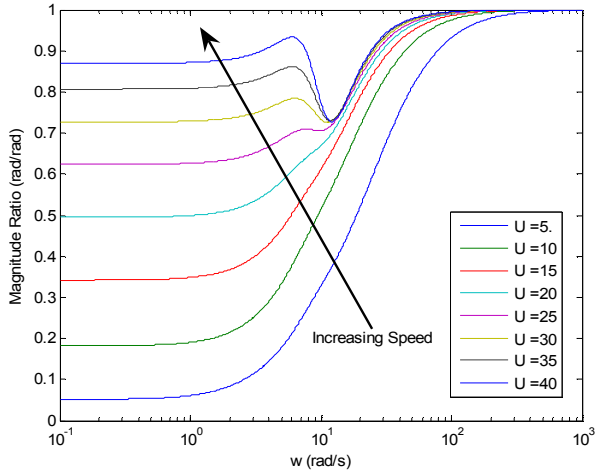

Figure **6.3**: Magnitude Response of Steering Input to Front Slip Angle, Speed Varied

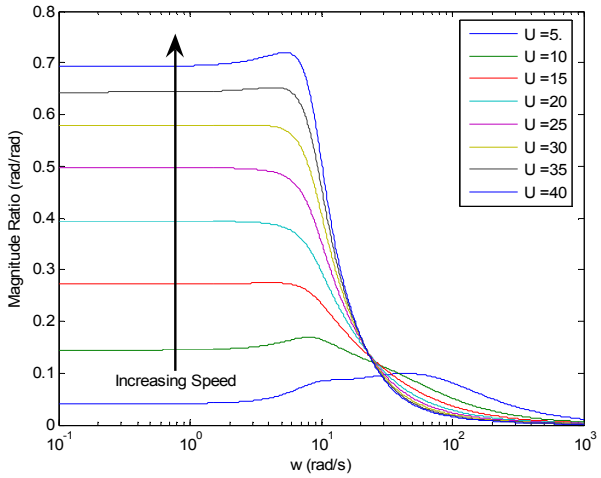

Figure **6.4**: Magnitude Response of Steering Input to Rear Slip Angle, Speed Varied

In reality a vehicle's tires cannot produce arbitrarily large forces, and will saturate or peak in their force production capability at some finite amount of tire slip. It has been shown by Dixon in [2] (page 96) that tire saturation generally begins to occur at a slip angle of approximately 0.09 rad (~5 deg). The figures above define the relationship between steering input and tire slip, assuming linear system dynamics. What should be clear from both the figures as well as their derivation is that the tire slip dynamics are governed by eigenvalues of the vehicle chassis behavior. This is an important insight since chassis dynamics are likely to be slow compared to the time periods at which the tire is likely to enter saturation. The time required for transient dynamics of the tire is therefore assumed to be quite small relative to the vehicle's motion. In other words, one can *approximate* the nonlinear tire behavior with a linear model of tire behavior that remains linear up to the point of loss of adhesion. After this point, the tire will be sliding and the transition to sliding will be so quick as to be not likely affected by, or coupled to, the chassis motion.

There is some conservatism if one uses the linear models to predict skid before roll. The linear tire approximation will predict tire forces at the point of sliding to be much higher than would be seen in a vehicle, and hence the excitation of the vehicle will be predicted to be much higher than would be observed experimentally. A comparison between the linear and nonlinear tire forces may be obtained by using the formulation described by Pajenka and is shown in Figure **6.5**. Further details on this nonlinear tire model are beyond the scope of this work, and will therefore not be discussed.

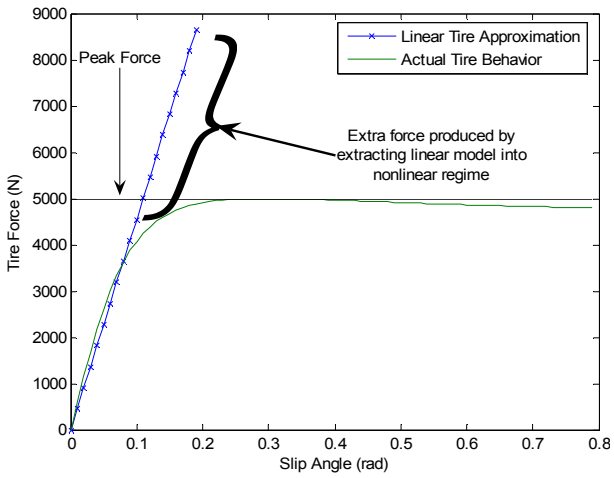

Figure **6.5**: Comparison Between Linear and Nonlinear Tire Models, Front Tire, Mercury Tracer.

Because of this increased excitation, the chassis models will over-predict excitation of the vehicle in roll at the point of tire saturation. Predicted roll angles and rollover forces at the time of skidding will be higher than would actually occur. Thus for larger steering inputs, predicted skidding occurs later, and predicted roll occurs sooner, than would be seen in practice. Hence, if one predicts a vehicle to safely skid before roll using these linear models and tire approximations, then the true vehicle will be quite unlikely to rollover prior to skidding.

To solve for the minimum steering input necessary to induce tire saturation, the following method is used: First, the magnitude ratio of the above figures may be represented symbolically as:

$$Ratio = \frac{\alpha(\omega)}{\delta_f(\omega)} \tag{6.7}$$

Knowing this ratio and the point of tire saturation, one can solve for the minimum steering angle at which the front and rear tires saturate at each frequency by:

$$\delta_{f,sat,front} = \frac{\delta_f}{\alpha_f} \cdot \alpha_{\max} \tag{6.8}$$

for the front tires, and:

$$\delta_{f,sat,rear} = \frac{\delta_f}{\alpha_r} \cdot \alpha_{\max} \tag{6.9}$$

for the rear tires. Here $\alpha_{\max}$ is the maximum slip angle before tire saturation (specified above), $\delta_{f,sat,front}$ is the minimum steering angle at which the front tires will saturate, and $\delta_{f,sat,rear}$ is the minimum steering angle at which the rear tires will saturate. These values are of critical importance in determining when a vehicle will slide since they provide an indication as to when the tires will saturate based upon driver input. Once tire saturation occurs, they can no longer produce an increased amount of cornering force to accommodate the driver's steering command and the vehicle begins to slide. Application of Eq. **6.8** and Eq. **6.9** to the data in Figure **6.3** and Figure **6.4** provides the minimum steering amplitude for a sinusoidal input at which tire saturation occurs at each frequency e.g. skidding. Steering inputs below this amplitude will excite the vehicle much like the linear dynamics models, whereas inputs above this amplitude will be largely mitigated

and will actually result in *less* forces on the tire and vehicle, and hence *less* excitation. This results in a smaller reaction torque from the suspension. This relationship is shown in Figure **6.6** for the front tires and Figure **6.7** for the rear tires.

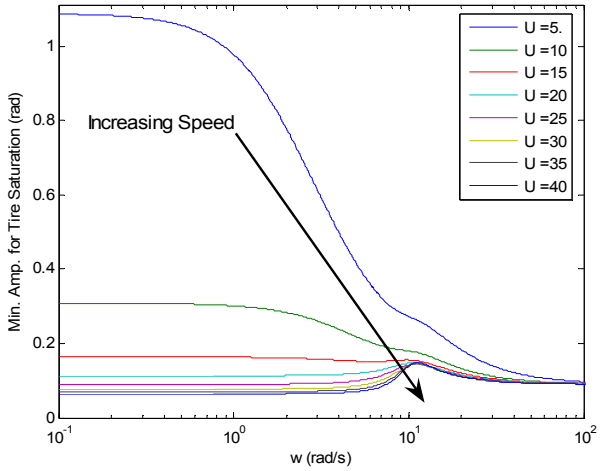

Figure **6.6**: Minimum Steering Angle for Front Tire Saturation vs. Input Frequency, Speed Varied

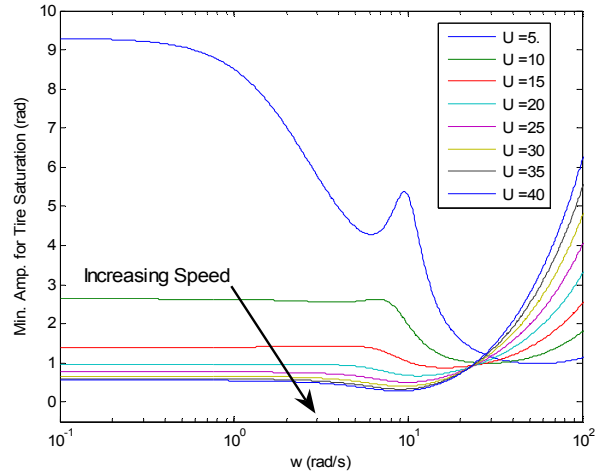

Figure **6.7**: Minimum Steering Angle for Rear Tire Saturation vs. Input Frequency, Speed Varied

The first important observation is that the front tires appear to saturate before the rear tires. This makes sense since directional control of the vehicle is being modified by front steering input. Additionally, there are benefits from a safety standpoint since it would be more desirable to lose directional control before loosing directional stability (which occurs during rear-wheel saturation). This safety tradeoff is the reason why brakes are typically designed such that the front brakes lock before the rear.

The second important observation is that as input frequency increases, the minimum steering angle to saturate the front tires levels off to approximately 0.09 rad, or $\alpha_{\max}$, while the minimum steering angle required to saturate the rear tires tends towards infinity. The reason for this may be seen by examining Eq. **6.1** and Eq. **6.2**. As frequency increases, the response of the vehicle states (i.e. *V, r,* and φ) approaches zero. Therefore as frequency increases, the slip angle on the front tires approaches δ_f, and the rear slip angle approaches zero.

The next step in determining whether or not a vehicle will roll before it slides is to determine the ratio of steering input to restoring moment. The restoring moment comes from the suspension components. This moment is directly related to whether or not the wheels of the vehicle will lift off of the ground. The ratio of steering input to restoring moment is found by using the output equation:

$$y_{restoring} = \begin{bmatrix} 0 & 0 & K_\phi & D_\phi \end{bmatrix} \cdot \begin{bmatrix} V \\ r \\ \phi \\ \dot{\phi} \end{bmatrix} + [0] \cdot \delta_f \qquad \textbf{6.10}$$

The magnitude portion of the frequency response is shown by Figure **6.8**.

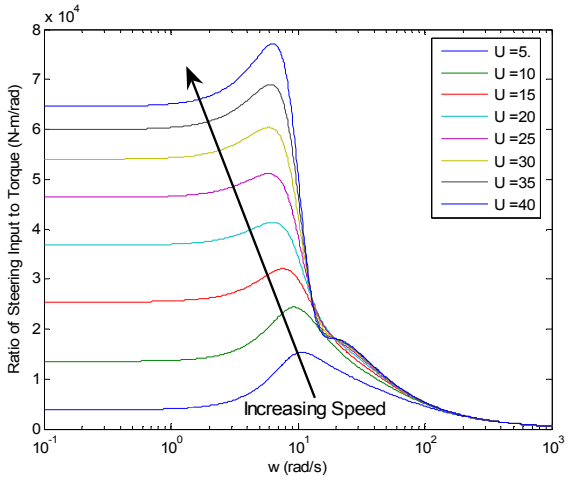

Figure **6.8**: Steering Input to Restoring Moment

Recognizing that the ratio indicated in Figure **6.8** may be represented symbolically as:

$$Ratio(\omega) = \frac{M_{restore}(\omega)}{\delta_f(\omega)} \qquad \textbf{6.11}$$

where $M_{rest}(\omega)$ is the restoring moment of the suspension at a given frequency. The magnitude of the restoring moment acting on the vehicle body at tire saturation may be found by combining Eq. **6.8** and Eq. **6.11** to form the relationship:

$$M_{restore,sat} = \frac{M_{restore}(\omega)}{\delta_f(\omega)} \cdot \delta_{f,sat,front} \qquad \textbf{6.12}$$

Figure **6.9** shows the suspension torque vs. input frequency.

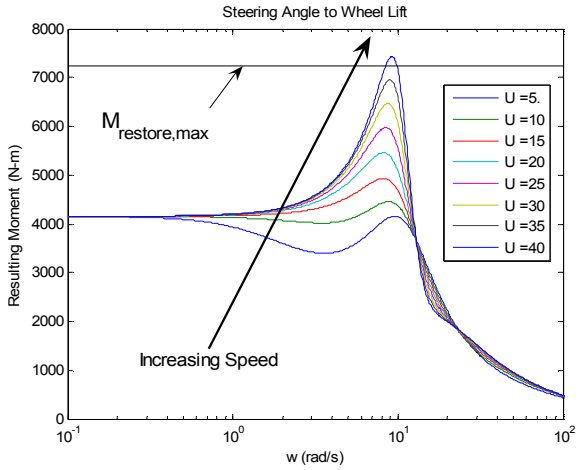

Figure **6.9**: Suspension Torque at Tire Saturation vs. Input Frequency, Speed Varied

An interesting result shown in Figure **6.9** is the size of the resonant peak at large speeds. It is clear that when driving fast, a driver may quickly find himself entering a rollover when reacting to an emergency situation, as typical highway driving generally involves low frequency steering inputs. However, while a resonant peak is evident in Figure **6.9**, the moment induced by the suspension cannot be infinite. At some point, wheel lift will occur, and this limiting value $M_{rest,max}$ must be found.

To find the relationship between steering input and suspension moment, a procedure is presented based on a simple force balance. The effect of the suspension on the tires is shown graphically in Figure **6.10**. The moment M_{rest} is the restoring moment supplied by the suspension and W is the weight of the vehicle. The equivalent couple moment acting on the tires resulting from the suspension is shown in light blue, and has a magnitude of M_{rest}/t. Additionally, a positive suspension displacement and equal weight distribution about the x-z plane (i.e. $I_{xz} = 0$) are assumed.

Summing forces in the vertical direction on the passenger side tire (right-hand side) gives:

$$\sum F_{pass.tire} = \frac{-M_{restore,sat}}{t} + \frac{W}{2} \qquad \textbf{6.13}$$

Substitution of the vehicle parameters in Table **6.1** gives the threshold torque for wheel lift to be:

$$M_{restore.sat} = \frac{W}{2} \cdot t = \frac{10{,}115N}{2} \cdot 1.43m = 7{,}231N \cdot m \qquad \textbf{6.14}$$

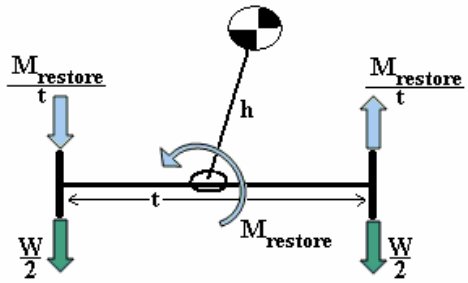

Figure **6.10**: Free-Body Diagram of the Suspension-Wheel Interaction

Applying the wheel-lift threshold to the vehicle representation in Figure **6.9**, the approximate speed and frequency at which rollover is most likely may be found. This approximation is made by taking the maximum suspension moment at each speed and comparing it to the threshold specified by Eq. **6.14**. Using this criteria, it was found that the Mercury Tracer will have a chance of rolling before sliding at approximately 40 m/s if the steering command particularly excites frequencies around 9.2 rad/s. Since this speed is significantly higher than typical highway speeds, it is unlikely that the Tracer will roll before sliding in an emergency situation unless the vehicle is already being driven at unsafe speeds.

An alternative approach to determine the slide-before-roll condition is to determine the steering angle at which wheel lift will occur. This angle may then be compared to the steering angle at which tire saturation occurs: If the steering angle for wheel lift is lower than the steering angle for tire saturation, then there is an increased probability that the vehicle will roll before sliding.

By using the ratio defined by Eq. **6.11** and recognizing that the maximum allowable moment is expressed in Eq. **6.14**, the steering angle at which wheel-lift is likely to occur may be solved by the equation:

$$\delta_{f,lift} = \frac{\delta_f}{M_{rest}} \cdot M_{rest,\max} \qquad \textbf{6.15}$$

This minimum steering angle required for wheel lift can be calculated from Eq. **6.11** and Eq. **6.15**. The result is shown in Figure **6.11**.

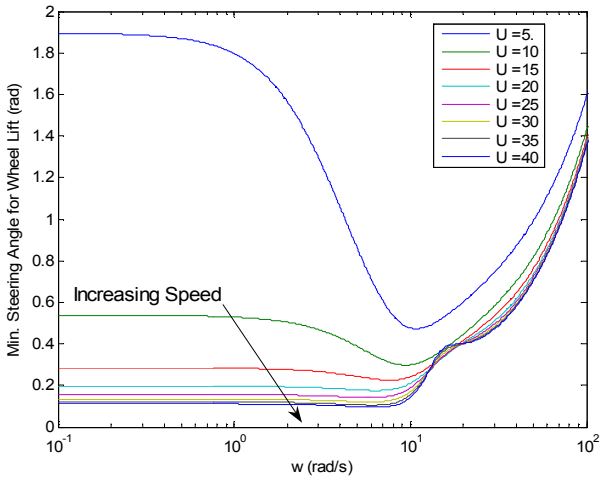

Figure **6.11**: Minimum Steering Angle for Wheel Lift vs. Input Frequency, Speed Varied

A qualitative comparison between Figure **6.11** and Figure **6.6** may be obtained. A side-by-side comparison between the minimum steering angle required to saturate the tires and

the minimum steering angle required induce wheel lift is shown in Figure **6.12** at both 5 and 40 m/s. Numerically, the approximate velocity and speed at which wheel lift will occur prior to tire saturation may be found by comparing the two steering angles at each frequency, for each speed. Using this procedure, it is readily seen that the predicted speed and input frequency for wheel-lift using both methods is identical, 40 m/s and 9.2 rad/sec steering inputs.

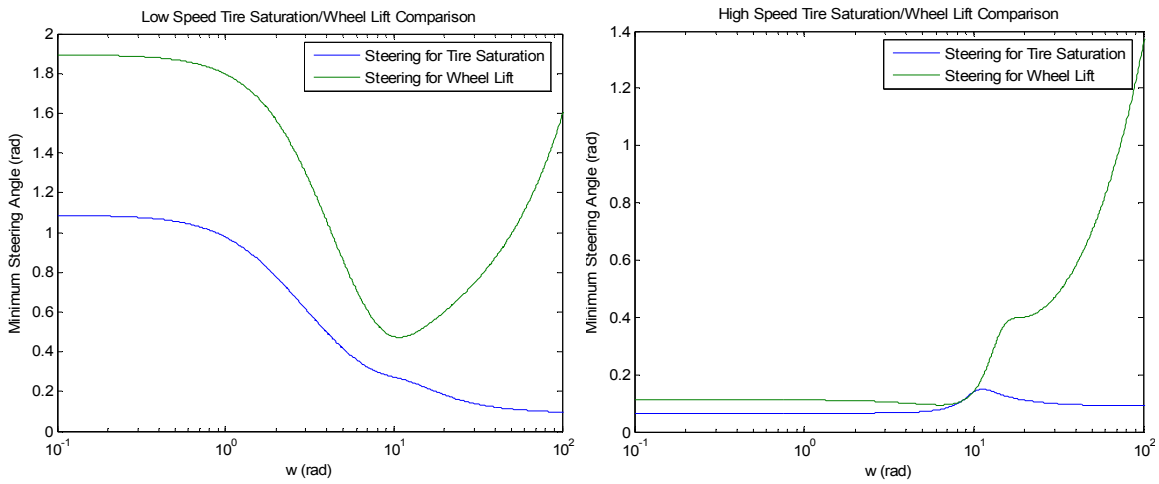

Figure **6.12**: Comparison of Minimum Steering Angles for Wheel Lift and Tire Saturation at 5 m/s and at 40 m/s, Mercury Tracer

The validity of these methods is further enforced when examining the Jeep Grand Cherokee. A complete set of parameters for this vehicle may be found in [3], and are shown below in Table **6.2**. Using both of the above methodologies, it is predicted that the Jeep Grand Cherokee will slide before rolling at any speed up until 40 m/s – far in excess of speeds actually attainable by the vehicle. The results for the roll-moment threshold method are shown below in Figure **6.13**, and the results for the steering angle comparison method are shown in Figure **6.14**.

Table 6.2: Vehicle Parameters for the Jeep Grand Cherokee

Variable	Value	Units	Variable	Value	Units
m	1663	kg	l	2.578	m
m_s	1338	kg	h	0.682	m
I_{zz}	2704	kg-m^2	K_φ	56957	N*m/rad
I_{xx}	602	kg-m^2	D_φ	3496	N*m*s/rad
I_{xz}	85	kg-m^2	C_f	-29748	N/rad
l_f	1.147	m	C_r	-54700	N/rad
l_r	1.431	m			

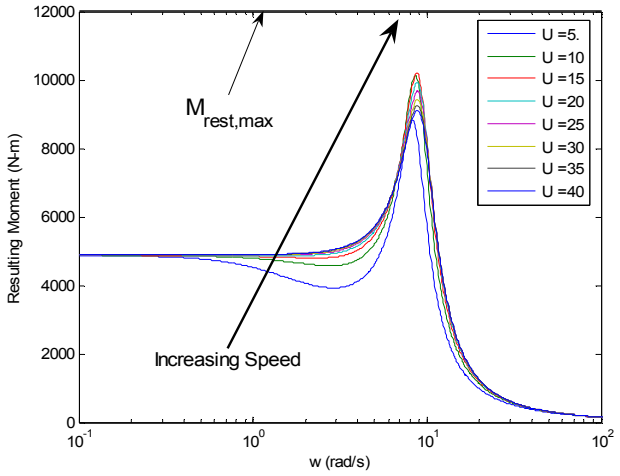

Figure 6.13: Suspension Torque at Tire Saturation vs. Input Frequency, Speed Varied, Jeep Grand Cherokee

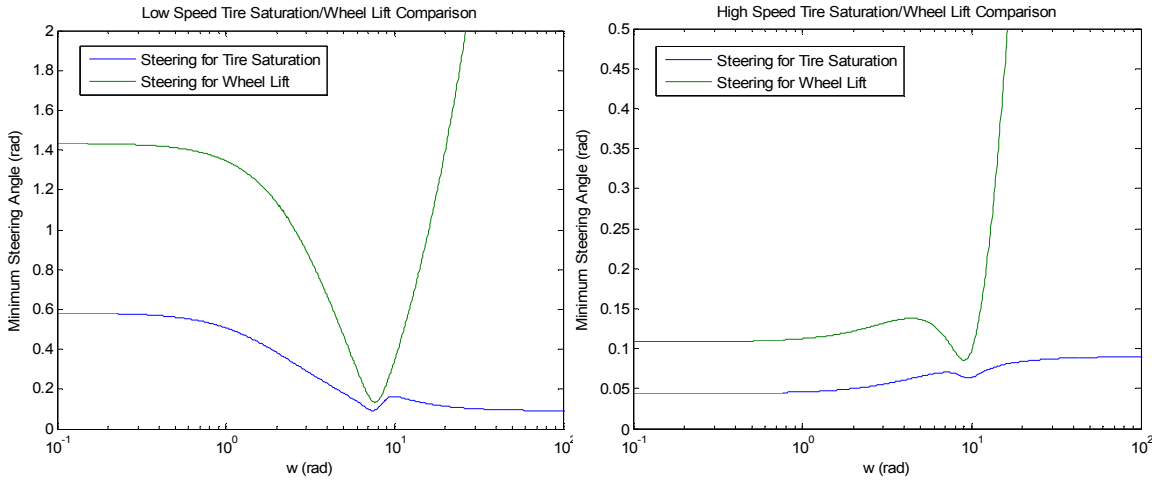

Figure **6.14**: Comparison of Minimum Steering Angles for Wheel Lift and Tire Saturation at 5 m/s and at 40 m/s, Jeep Grand Cherokee

This result agrees qualitatively with dynamic testing performed by NHTSA [4], whose results indicate that they were unable to observe wheel lift for any of their standard test maneuvers performed on the Jeep Grand Cherokee. Another interesting fact shown in the report is that the Jeep Grand Cherokee has a nearly identical Static Stability Factor (SSF) to the Ford Ranger, the Isuzu Trooper, and the Acura SLX. However, the Ranger, Trooper, and SLX showed wheel lift for all four of the tests performed, while the Cherokee showed wheel lift in none of them. Based on the SSF, the 2001 Grand Cherokee received only two stars for rollover resistance. Such findings show the serious flaw in relying on the SSF measurement for determining rollover resistance and reinforce why NHTSA includes dynamic testing in their current rating system. The 2006 Cherokee model has a four star rating.

6.2 Rollover Prevention Algorithms

While both the Mercury Tracer and the Jeep Grand Cherokee demonstrate excellent resistance to experiencing an untripped rollover, it is clear from the NHTSA testing performed [4] that many vehicles will exhibit wheel lift due to transient inputs. For example, while the Jeep Grand Cherokee has an SSF of 1.07 and performed well during the dynamic tests performed by the government, the Isuzu Trooper and Acura SLX both have an SSF of 1.08 and showed wheel lift in all of NHTSA's dynamic tests.

Choosing parameters likely to induce wheel lift (and possibly rollover), a fictitious vehicle will be created in order to investigate the feasibility of a number of proposed control strategies. This vehicle will have the same characteristics as the Mercury Tracer (shown in Table **6.1**), yet with the damping rate reduced by one-half. This vehicle will hereafter be referred to as the *High Roller*. For reference, the restoring-moment as a function of input frequency for the High Roller is shown below in Figure **6.15**.

The remainder of this Chapter focuses on control methods that prevent wheel lift. Specifically, the methods attempt to reduce the resonant peak observed in the roll-moment response such that steering inputs will not cross the critical threshold until the vehicle is traveling at or above 40 m/s, e.g. recover the behavior of the well-designed Tracer vehicle. A challenge of each control method is to achieve rollover prevention while having little to no apparent effect on the vehicle's planar dynamics. In other words, the overall design goal is to have the High Roller perform in much the same manner as the Tracer by means of a steer-by-wire system without affecting steerability.

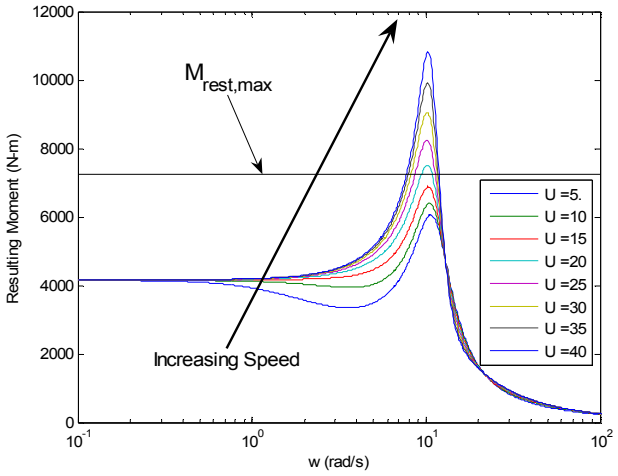

Figure **6.15**: Suspension Torque at Tire Saturation vs. Input Frequency, Speed Varied, High Roller

6.2.1 Open-Loop Control Methods

This section outlines the open-loop control methods to be investigated. The reason for exploring open-loop control strategies is their simplicity. However, there are a number of shortcomings to these methods that will be outlined in the proceeding sections. The methods that will be investigated are notch filter, pole cancellation, and deadbeat control. This section will provide a definition and general outline of each of the open-loop control strategies, presenting the general design procedure, overall effect on the system, and drawbacks. A second order, underdamped system will be used as an example due to its simplicity and resonant mode comparable to that of the vehicle's roll mode.

6.2.1.1 Notch Filter Design

6.2.1.1.1 Basic Principle

The notch-filter approach assumes that there is a certain range of inputs in the frequency domain that greatly contribute to an undesirable response and the filter attempts to eliminate signal transfer at these frequencies. Such a situation is similar to what is observed in the High Roller, where a certain frequency range causes a particularly high suspension response. Typically, this range of inputs centers about the natural frequency(ies) of the plant to be controlled. The basic control strategy is outlined in Figure 6.16, with the filter designed to block the undesirable frequency range of input. An alternative name for the notch filter is a band-stop filter.

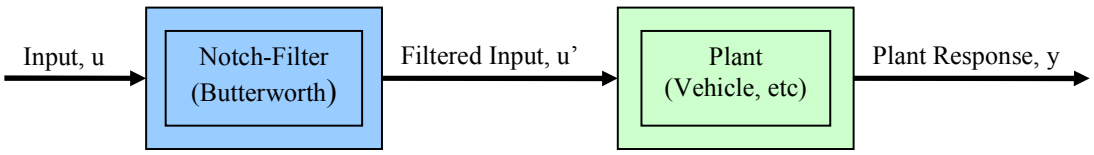

Figure 6.16: Open-Loop Control Strategy 1, Notch Filtering

To present an example of a notch filter, consider a lightly damped SISO second-order system. The plant described by Eq. 6.16 has a natural frequency, or ω_n, of 1.3 rad/s, and a damping ratio, or ξ, of 0.1. Examination of its Bode plot (Figure 6.17) shows that for inputs corresponding to the natural frequency, an observer may expect to see a gain ratio of approximately 15. Specifying a arbitrary design criteria that the gain cannot be greater than 10, the initial boundaries for the band-stop filter are chosen to be between 1.1 and 1.5 rad/s.

$$\frac{y}{u} = \frac{s + \omega_n^2}{s^2 + \omega_n \zeta + \omega_n^2} = \frac{s + 1.69}{s^2 + 0.13s + 1.69} \qquad \textbf{6.16}$$

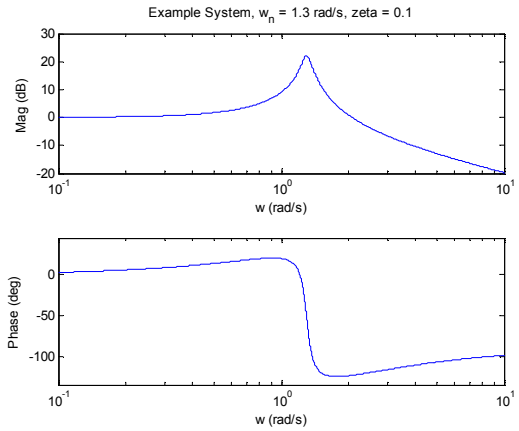

Figure **6.17**: Bode Plot of Example System

The frequency boundary values for the band-stop filter are passed to the MATLAB function *butter* and a second order band-stop filter is specified. The resulting filter is defined by:

$$\frac{u'}{u} = \frac{s^4 + 3.3 \cdot s^2 + 2.722}{s^4 + 0.5657 \cdot s^3 + 3.46 \cdot s^2 + 0.9334 \cdot s + 2.722} \qquad \textbf{6.17}$$

The effect of the filter may be seen by examining the Bode plot of the cascaded filter-plant system. The frequency response of the filter is shown in Figure **6.18**; it is seen that the input frequencies are severely reduced the immediate vicinity of the natural frequency, while the remainder of the spectrum is largely unaffected.

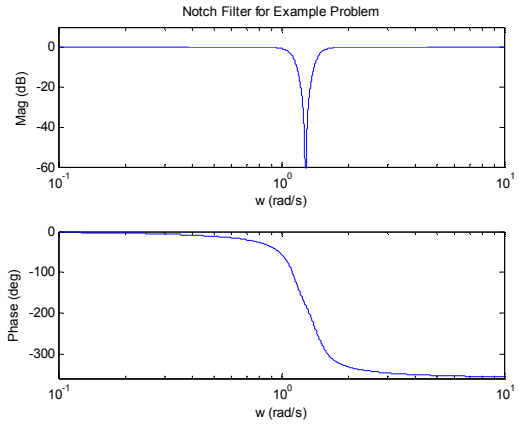

Figure **6.18**: Band-Stop Filter for Example System

By cascading the filter with the plant, the resulting input/output frequency response indeed meets the gain limits imposed earlier, with a maximum gain of 9.22.

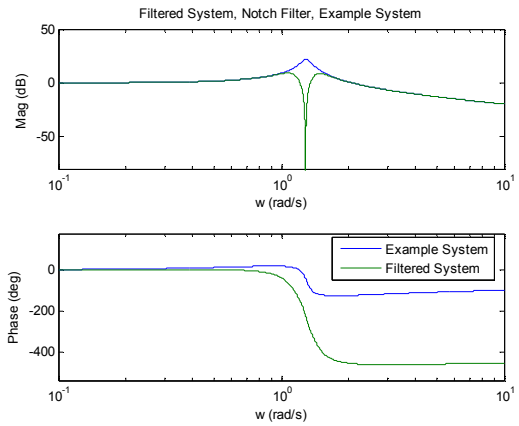

Figure **6.19**: Example System after Application of Notch Filter

6.2.1.1.2 Drawbacks of the Notch Filter

As can be seen from Figure **6.19**, the net effect of the notch filter is that the influence of the inputs at the natural frequency are not only limited, but are effectively

eliminated altogether. This effect may not be desirable for plants such as a passenger vehicle. For instance, if a driver were to attempt a lane change maneuver near the frequency chosen for the band-stop filter, the car would not move laterally and hence the vehicle may behave unpredictably. To achieve lateral motion, the driver must significantly change his/her input to compensate for the effect of the filter. An example of this type of behavior is shown in Figure **6.20**, where the example system is subjected to a chirp input. The starting frequency is 0.5 rad/s, with a final frequency of 3 rad/s at the end of 60 seconds. This simulation is to show the response of the system as the input passes through the filtered region.

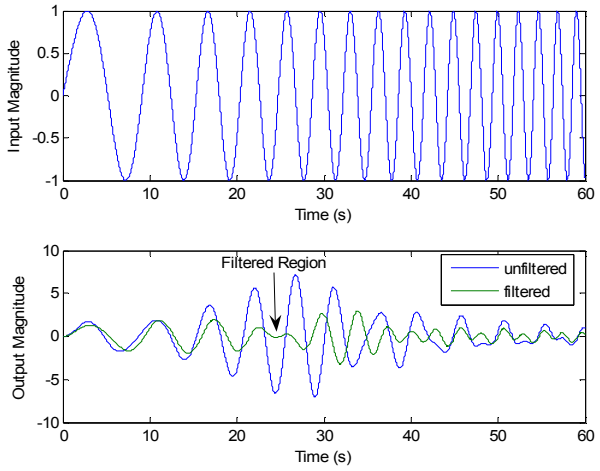

Figure **6.20**: Chirp Response of the Example System Before and After the Application of the Notch Filter

6.2.1.2 Pole Cancellation

6.2.1.2.1 Basic Principle

Building on the previous method, it would be more desirable to simply level out the resonant peak than to completely eliminate the response about that frequency. Placing Eq. **6.16** into factored form, the example system becomes:

$$\frac{y}{u} = \frac{s + 1.69}{(s + 0.065 + 1.2984\mathrm{i})(s + 0.065 - 1.2984i)} \qquad \textbf{6.18}$$

On first examination, a simple method for eliminating the resonant peak would be to design the filter to be:

$$\frac{u'}{u} = (s + 0.065 + 1.2984\mathrm{i})(s + 0.065 - 1.2984i) \qquad \textbf{6.19}$$

While application of this filter would eliminate the resonant poles, it would also create a system where the order of the numerator is greater than the order of the denominator. Because the order of the numerator is equal to or greater than the denominator, the transfer function is not proper. The importance of proper transfer functions relates to a concept known as determinism. Essentially, if a system is not proper, then it is non-deterministic. This means that the system may have more than one possible output for a given input. In a deterministic system, the output may be determined by the current state of the system and thus the time response may be predicted exactly. This may be seen by recognizing that the Laplace transform of the derivative is "s", and the Laplace transform of successive derivatives is s^n, where n is the order of the derivative. As an example, take the transfer function:

$$\frac{y(s)}{u(s)} = \frac{s^2 + 3s + 4}{s + 3} \qquad \textbf{6.20}$$

From the definitions above, this system is not proper, and is therefore non-deterministic. This becomes more apparent when we separate the system back into the input and output components:

$$\left(s^2 + 3s + 4\right) \cdot u(s) = \left(s + 3\right) \cdot y(s) \qquad \textbf{6.21}$$

and take the inverse Laplace transform:

$$\frac{d^2u}{dt} + 3\frac{du}{dt} + 4u = \frac{dy}{dt} + 3y \qquad \textbf{6.22}$$

Recalling that u is the input to the system and y is the output, Eq. **6.22** implies that the second derivative of the input is known, but the second derivative of the output is not known. Such a system is non-deterministic, which means that the state of a system can not be predicted exactly i.e. there is more than one possible output for a given input.

To ensure a proper filter, one can add higher order dynamics. Such a filter has the general structure:

$$\frac{u'}{u} = \frac{\left(s + p_1\right) \cdot \left(s + p_2\right)}{\left(s + p_{H1}\right) \cdot \left(s + p_{H2}\right)} \qquad \textbf{6.23}$$

where $p_{1,2}$ is the complex pair of poles that are to be canceled and p_{H1} and p_{H2} are the higher frequency poles that enforce determinism. For the current example, the filter will be defined by the transfer function:

$$\frac{u'}{u} = \frac{1.18 \cdot \left(s + 0.065 + 1.2984\mathrm{i}\right) \cdot \left(s + 0.065 - 1.2984i\right)}{\left(s + 1\right) \cdot \left(s + 2\right)} \qquad \textbf{6.24}$$

which has the Bode plot:

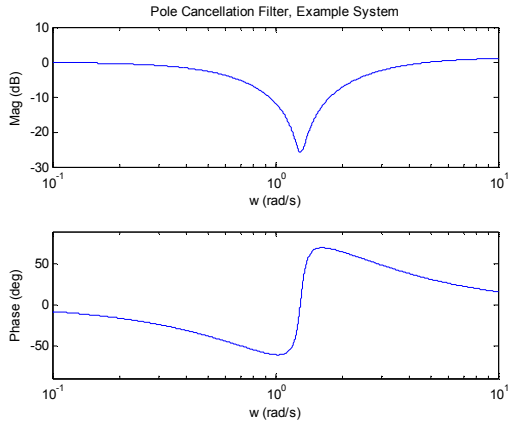

Figure **6.21**: Pole Cancellation Filter for Example System

Note that while the poles of -1 and -2 are not considered to be higher frequency than the existing poles, the location of the zero at 1.3 rad/s would cause an increase in magnitude gain of 20 dB/decade until the higher frequency poles have any effect. Following application of the filter, we see that the response of the filter changes from:

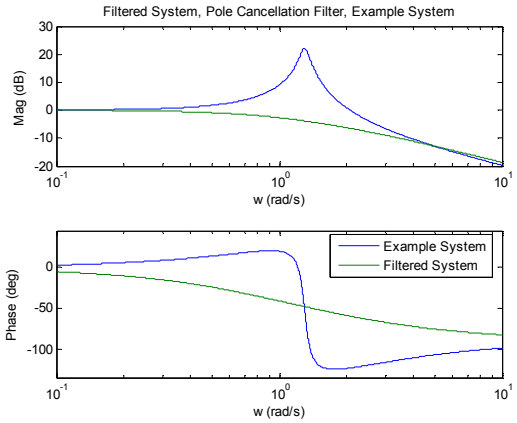

Figure **6.22**: Example System after Application of Pole Cancellation Filter

The input/output response of the pole cancellation filter is similar to the notch filter in that there is mitigation of the resonant frequency oscillations. However, the pole cancellation filter is an improvement because it flattens, rather than cancels, the response

of the system to input frequencies near resonance. The net result is a system with much greater damping.

6.2.1.2.2 Drawbacks of the Pole Cancellation Method

From the previous example, it would seem that the pole cancellation filter would be an ideal choice: it is simple in structure, and is easy to design. However, the method also assumes perfect knowledge of the system. In practice this is not the typical case. To investigate the effect of model uncertainty, the example system will be the "approximated system", while the "actual system" will be described by the transfer function:

$$\frac{y_{actual}}{u_{actual}} = \frac{s+\omega_n^2}{s^2+\omega_n\zeta+\omega_n^2} = \frac{s+2.56}{s^2+0.16s+2.56} \qquad 6.25$$

This system has the same damping ratio as the approximate system, but has a natural frequency of 1.6 rad/s as opposed to 1.3 rad/s. Applying the filter described by Eq. 6.24 to this system will result in a frequency response of:

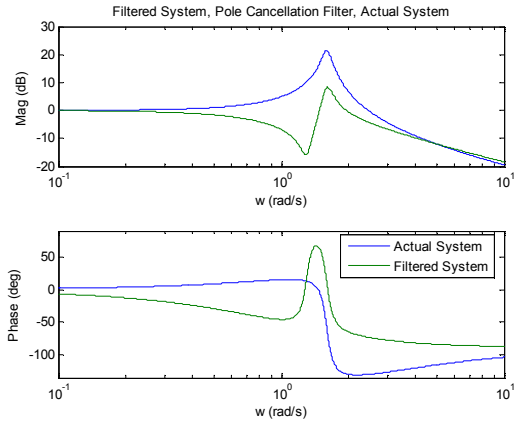

Figure 6.23: Pole Cancellation Filter Applied to Example System with Uncertainty

Following the addition of model error, the maximum gain magnitude of the filtered system is 10.4dB, violating the 10dB constraint specified earlier. Additionally, the response of the system about the natural frequency now has a rather abrupt change in both magnitude and phase. This example clearly shows how this method, while simple, requires accurate knowledge of the system.

6.2.1.3 Dead-Beat Control

6.2.1.3.1 Principle of Operation

The final open-loop control method that will be examined is known as dead-beat control. This form of control does not seek to simply cancel out certain undesirable dynamics. Rather it replaces the dynamics of a system with the desired dynamics. For the current example, the damping ratio is 0.1. In the desired system this will be increased to 0.7 (chosen arbitrarily to illustrate the use of the dead-beat controller). Additionally, the desired system will not have any zeros.

The structure of this controller is relatively simple. By representing the example system as:

$$\frac{y}{u}=\frac{s+1.69}{s^2+0.13s+1.69}=\frac{s+1.69}{(s+0.065+1.2984\mathrm{i})(s+0.065-1.2984i)}=\frac{B(s)}{A(s)} \qquad 6.26$$

and defining the desired system as:

$$\frac{y}{u}=\frac{1}{s^2+0.91s+1.69}=\frac{1}{(s+0.455+1.2178\mathrm{i})\cdot(s+0.455-1.2178i)}=\frac{B_d(s)}{A_d(s)} \qquad 6.27$$

then the complete system may be represented in block diagram format as:

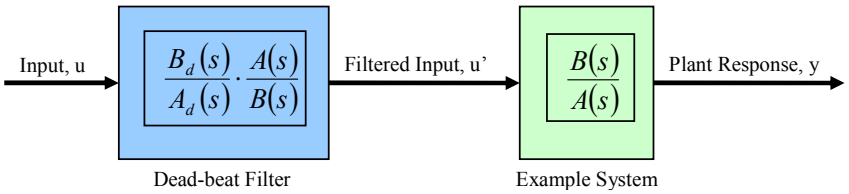

Figure **6.24**: Dead-Beat Filter Structure

By simple block diagram algebra, the resulting system becomes the desired system and may be realized by a simplified structure as:

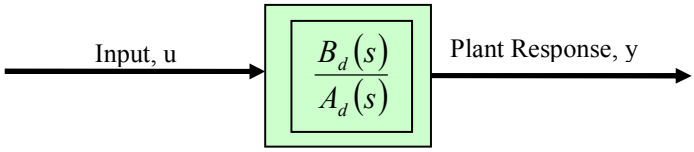

Figure **6.25**: Filtered System, Dead-Beat Filter

Therefore, by applying the filter:

$$\frac{u'}{u} = \frac{(s+0.065+1.2984\mathrm{i})\cdot(s+0.065-1.2984i)}{(s+0.455+1.2178\mathrm{i})\cdot(s+0.455-1.2178i)\cdot(s+1.69)} \qquad \textbf{6.28}$$

the resulting change in system dynamics are shown in Figure **6.27**.

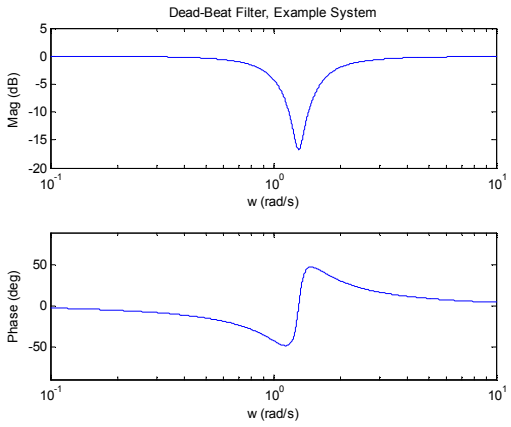

Figure **6.26**: Dead-Beat Filter

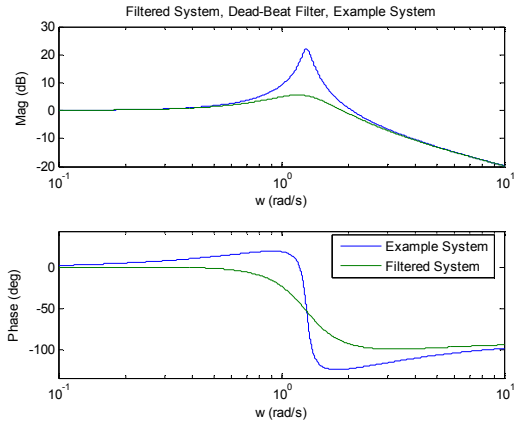

Figure 6.27: Filtered System, Dead-Beat Filter, Example System

Clearly, the filter produced the desired system dynamics. Note that the dead-beat controller is quite similar to the pole cancellation controller except that the designer is specifying the high-frequency components to achieve dynamic matching to a reference model.

6.2.1.3.2 Drawbacks of the Dead-Beat Control Method

As with the previous control strategies, this same controller will be applied to a system with uncertainty. By taking the "actual" system defined by Eq. 6.25 and applying the dead-beat filter, the resulting system has the response described by Figure 6.28.

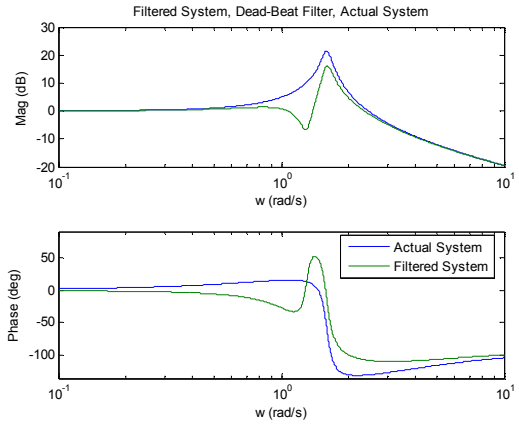

Figure **6.28**: Filtered System, Dead-Beat Filter, Actual System

Comparing this result with those shown in Figure **6.23**, it is seen that while the DC gain of the system remains unchanged, the response about the natural frequency of the actual system exhibits an increase in both magnitude and phase similar to the one shown in the pole-cancellation controller. Additionally, the peak gain amplitude of the resulting system is 15.9 – considerably higher than the results shown by the application of the pole-cancellation filter. A similar situation will arise if there are unmodeled dynamics in the system.

Another drawback to dead-beat control is that it requires the zeros of the open-loop system to be stable, a situation that may not necessarily be common. For example, all real systems possess some time delay which can be approximated by unstable zeros with a Padé approximation. A Padé approximation is a rational function that approximates another known polynomial to a specified order. This approximation is accomplished by a ratio of two polynomials, and for a time delay (an infinite polynomial) is represented in the frequency domain as [5]:

$$e^{-Ts} \approx \frac{\left(1-\frac{T}{2n}s\right)^n}{\left(1+\frac{T}{2n}\right)^n} \qquad \textbf{6.29}$$

where T is the time delay of the system and n is the order of the approximation. One can see from the numerator that a true time delay introduces an infinite number of unstable zeros, and that even low-order approximations of time delay will introduce a few unstable zeros. Non-minimum phase zeros will therefore pervasive in approximating system behavior because time delays are quite common in actuator dynamics, sensor acquisition, control algorithm computation times, and the like.

The application of this time delay on an actual plant P(s) causes the output of the system to be changed to be:

$$y(s) = P(s)\cdot u(s)\cdot e^{-Ts} \qquad \textbf{6.30}$$

If P(s) is subjected to a step input at t = 0, the effect of a first order Padé approximation will cause the input at t = 0 to be slightly negative for an initial transient period [6].

Setting the time delay equal to 0.01s and utilizing a 2nd order Padé approximation, the delay is approximated by:

$$\frac{y}{u} = \frac{s^2 - 800\cdot s + 160000}{s^2 + 800\cdot s + 160000} = \frac{(s-400)^2}{(s+400)^2} \qquad \textbf{6.31}$$

While the inclusion of this time delay into the dynamic model does not alter the stability of the original system, it does in fact make the dead-beat controller unstable as the unstable zeros in the numerator of the uncompensated system become the unstable poles of the filter.

6.2.2 Closed-Loop Control

All of the open-loop methods described above share a similar intent – canceling unwanted dynamics in favor of a preferred behavior. But they all share a similar shortcoming – they are not robust to uncertainty or unmodeled dynamics and therefore require absolute knowledge of the system. In the case of dead-beat control, the problem is even worse in that, even with absolute knowledge of the system, one may produce an unstable controller. Such shortcomings are characteristic of open-loop systems: because they lack feedback, open-loop systems can have large sensitivities to unmodeled dynamics, modeling errors, and disturbances.

Building on the desire to create more favorable dynamics in the system, a closed – loop control method will be employed. As a result of the necessity of feedback, the implementation of such a method is more complex than the open-loop algorithms presented above. However, closed-loop control is typically preferred, as the added robustness generally outweighs the cost of implementation.

6.2.2.1 Model Reference Control

6.2.2.1.1 Principle of Operation

The goal of Model Reference Control (MRC) is to control the system in a manner that causes it to behave like the desired system through a combination of feed-forward and feedback methods that will be described below. This method is known as model

reference control (MRC). The basic feedforward/feedback structure of MRC is outlined in Figure **6.29**.

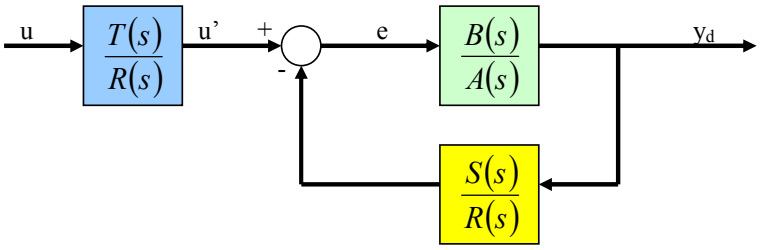

Figure **6.29**: MRC Control Architecture

By selecting T(s), R(s), and S(s) properly, the system will appear to have the simplified structure shown by Figure **6.25**. Carrying out block diagram algebra on the feedback loop, it is simplified to the form shown in Figure **6.30**.

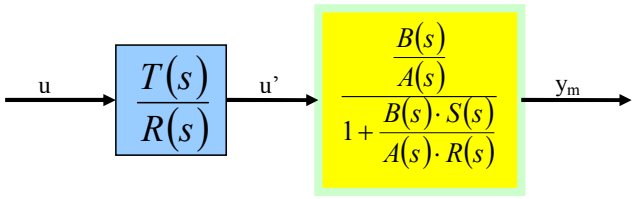

Figure **6.30**: MRC Control Structure, Simplification Step 1

The yellow-green block may be further simplified by:

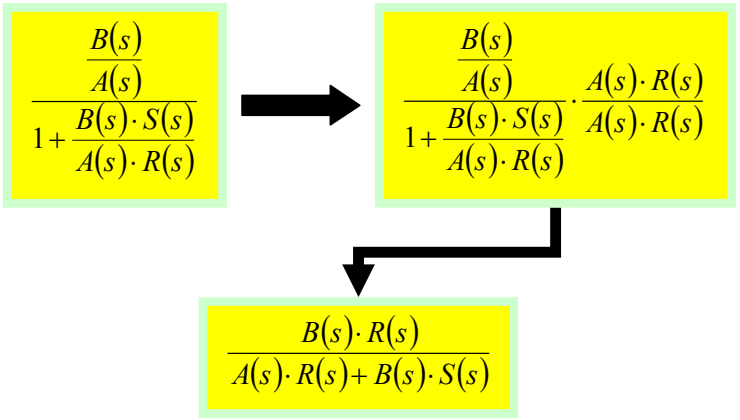

Figure **6.31**: MRC Control Structure, Simplification of Inner Loop

which allows the system to be fully reduced to the form shown in Figure **6.32**.

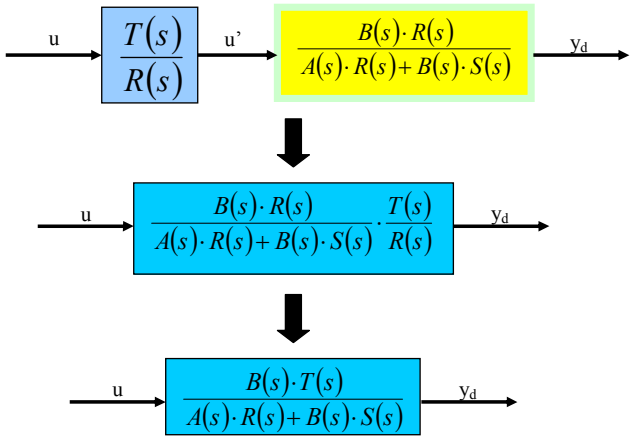

Figure **6.32**: MRC Control Structure, Full Simplification

Therefore, the transfer function of the MRC system is:

$$\frac{B(s)\cdot T(s)}{A(s)\cdot R(s)+B(s)\cdot S(s)}=\frac{y_d}{u} \qquad \textbf{6.32}$$

where:

$$A(s)\cdot R(s)+B(s)\cdot S(s)=A_c(s) \qquad \textbf{6.33}$$

is known as the Diophantine equation and is equal to the characteristic polynomial of the closed-loop system. Eq. **6.32** may therefore be rewritten as:

$$\frac{B(s)\cdot T(s)}{A(s)\cdot R(s)+B(s)\cdot S(s)}=\frac{B(s)\cdot T(s)}{A_c(s)} \qquad \textbf{6.34}$$

The remaining equations and conditions will follow the procedure outlined by Astrom and Whittenmark [7]. Recalling that the goal of MRC is to have the plant follow the dynamics of a reference model, the following relationship is specified as the desired dynamics of the system:

$$\frac{B_d(s)}{A_d(s)}=\frac{y_d(s)}{u(s)} \qquad \textbf{6.35}$$

When combined with Eq. **6.34**, Eq. **6.35** gives:

$$\frac{B(s)\cdot T(s)}{A_c(s)}=\frac{B_d(s)}{A_d(s)}=\frac{y_d(s)}{u(s)} \qquad \textbf{6.36}$$

An important insight here is that feedback control does not affect the zeros of a system. This may be seen by the appearance of *T(s)* – part of the feedforward controller – in the numerator of Eq. **6.36**, while $A_c(s)$ contains *S(s)* and *R(s)* – the elements of the feedback controller – are in the denominator. This relationship implies that there is some sort of cancellation of terms between the desired system and the closed-loop transfer function described by Eq. **6.32**. Knowing this, *B*(s) must be split into two components described by:

$$B(s)=B^{+}(s)\cdot B^{-}(s) \qquad \textbf{6.37}$$

The first component, $B^{+}(s)$, is the portion of $B(s)$ that is stable, well-damped, and will be cancelled by the controller. The second component, $B^{-}(s)$, is the portion of $B(s)$ that is either unstable or not well damped and therefore cannot be cancelled or affected by the controller. Since B(s) is in the numerator, unstable or poorly damped zeros do not necessarily affect the stability of the system. However, in order to the controller to cancel these terms, it would have to have unstable or poorly damped poles – a highly undesirable characteristic.

From these definitions, it is implied that $B^{-}(s)$ is a factor of $B_d(s)$ since it is not cancelled by the controller. Another implication is that $B^{+}(s)$ is a factor of $A_c(s)$ since the controller cancels it out. These implications lead to the definitions:

$$B_d(s) = B^{-}(s) \cdot B_d^{'}(s) \qquad \textbf{6.38}$$

$$A_c(s) = A_0(s) \cdot A_d(s) \cdot B^{+}(s) \qquad \textbf{6.39}$$

where $B_d^{'}(s)$ is comprised of the remaining factors of $B_d(s)$ that are not contained in $B^{-}(s)$ and $A_0(s)$ is comprised of the remaining factors of $A_c(s)$ that do not appear in $A_d(s) \cdot B^{+}(s)$. Substituting Eq. **6.38** and Eq. **6.39** back into Eq. **6.33**, the Diophantine equation becomes:

$$A(s) \cdot R(s) + B^{+}(s) \cdot B^{-}(s) \cdot S(s) = A_0(s) \cdot A_d(s) \cdot B^{+}(s) \qquad \textbf{6.40}$$

The appearance of $B^{+}(s)$ on both the left and right sides of Eq. **6.40** and the requirement that $B^{+}(s)$ must cancel implies that:

$$R = R'(s)\cdot B^{+}(s) \tag{6.41}$$

making the Diophantine equation:

$$A(s)\cdot R'(s)\cdot B^{+}(s)+B^{+}(s)\cdot B^{-}(s)\cdot S(s)=A_0(s)\cdot A_d(s)\cdot B^{+}(s) \tag{6.42}$$

which simplifies to:

$$A(s)\cdot R'(s)+B^{-}(s)\cdot S(s)=A_0(s)\cdot A_d(s) \tag{6.43}$$

Now, taking:

$$\frac{B(s)\cdot T(s)}{A_c(s)}=\frac{B_d(s)}{A_d(s)} \tag{6.44}$$

and substituting in Eq. **6.38** and Eq. **6.39**, Eq. **6.44** becomes:

$$\frac{B^{+}(s)\cdot B^{-}(s)\cdot T(s)}{A_0(s)\cdot A_m(s)\cdot B^{+}(s)}=\frac{B^{-}(s)\cdot B_d'(s)}{A_d(s)} \tag{6.45}$$

Equating sides yields:

$$\frac{T(s)}{A_0(s)}=B_d'(s)\Rightarrow T(s)=A_0(s)\cdot B_d'(s) \tag{6.46}$$

Since the goal in finding a solution is to obtain the polynomials R(s), T(s), and S(s) in order to obtain the feedforward controller $T(s)/R(s)$ and a feedback element $S(s)/R(s)$, it is required that the solutions obtained are at least proper (deterministic), e.g.:

$$\deg(S(s))\le\deg(R(s)) \tag{6.47}$$

$$\deg(T(s))\le\deg(R(s)) \tag{6.48}$$

If the plant dynamics $B(s)/A(s)$ are restricted to being strictly proper and the restrictions provided by Eq. **6.47** and Eq. **6.48** are considered, it may be seen that:

$$\deg(A(s)\cdot R(s)) > \deg(B(s)\cdot S(s)) \Rightarrow \deg(A(s)\cdot R(s)) = \deg(A_c(s)) \qquad \textbf{6.49}$$

Since:

$$\deg(A(s)\cdot R(s)) = \deg(A(s)) + \deg(R(s)) \qquad \textbf{6.50}$$

a restriction on the degree of R(s) is determined to be:

$$\deg(R(s)) = \deg(A_c(s)) - \deg(A(s)) \qquad \textbf{6.51}$$

By examining the possible solutions for the Diophantine equation, the final restriction on the degrees of the above equations may be found. Since Eq. **6.33** has two unknowns, an infinite number of solutions may be found. If $R^0(s)$ and $S^0(s)$ are solutions to R(s) and S(s), respectively, then the representations:

$$R(s) = R^0(s) + Q(s)\cdot B(s) \qquad \textbf{6.52}$$

$$S(s) = S^0(s) - Q(s)\cdot A(s) \qquad \textbf{6.53}$$

are also solutions, with Q(s) being an arbitrary polynomial. This is known as a Youla Parameterization; further details may be found in [5] (page 142). While there are an infinite number of solutions, one may always be obtained such that $\deg(S(s)) < \deg(A(s))$ so one can therefore find a solution where $\deg(S(s))$ is at most equal to $\deg(A(s)) - 1$. As a result of this relationship, Eq. **6.47** results in:

$$\deg(A_c(s)) \geq 2\cdot\deg(A(s)) - 1 \qquad \textbf{6.54}$$

For this application, equality of the left and right hand sides of Eq. **6.54** will be enforced to keep the order of the controller to a minimum.

For compatibility between the original plant and the reference plant, the following conditions also need to apply:

$$\deg\left(A_d(s)\right) = \deg\left(A(s)\right) \qquad \textbf{6.55}$$

$$\deg\left(B_d(s)\right) = \deg\left(B(s)\right) \qquad \textbf{6.56}$$

Under these conditions, Eq. **6.39** implies that:

$$2\cdot\deg\left(A(s)\right)-1 = \deg\left(A_0(s)\right)+\deg\left(A(s)\right)+\deg\left(B^+(s)\right) \qquad \textbf{6.57}$$

Solving for $\deg\left(A_0(s)\right)$, the final compatibility condition is obtained as:

$$\deg\left(A_0(s)\right) = \deg\left(A(s)\right)-\deg\left(B^+(s)\right)-1 \qquad \textbf{6.58}$$

Application of the above rules and formulas allows for a unique solution of both the feedforward and feedback elements of the MRC control loop. An example will now be presented in order to illustrate the design procedure.

6.2.2.1.2 Application of MRC to the Example System

Recalling that the example system is:

$$\frac{y}{u} = \frac{s+\omega_n^2}{s^2+\omega_n\zeta+\omega_n^2} = \frac{s+1.69}{s^2+0.13s+1.69} \qquad \textbf{6.59}$$

the desired system will be defined by:

$$\frac{B_d(s)}{A_d(s)} = \frac{s+9}{s^2+2.12s+9} \qquad \textbf{6.60}$$

Adhering to the rules defined above, the design procedure is as follows:

(1) Check compatibility

- $\deg(A_d(s)) = \deg(A(s)) \Rightarrow \deg(s^2+0.13s+1.69) = \deg(s^2+2.12s+9)$
- $\deg(B_d(s)) = \deg(B(s)) \Rightarrow \deg(s+9) = \deg(s+1.69)$

(2) Define components of B(s) and $B_d(s)$

- $B(s) = B^+(s) \cdot B^-(s)$
- $B^+(s) = s+1.69$
- $B^-(s) = 1$
- $B_d(s) = B^-(s) \cdot B_d^{'}(s)$
- $B_d^{'}(s) = s+9$

(3) Find $A_0(s)$ and $A_c(s)$

- $\deg(A_0(s)) = \deg(A(s)) - \deg(B^+(s)) - 1 = 2-1-1 = 0$
- choose $A_0(s) = 1$
- $A_c(s) = A_0(s) \cdot A_d(s) \cdot B^+(s) = 1 \cdot (s^2+2.12s+9) \cdot (s+1.69)$

(4) Solve for R(s)

- $\deg(R(s)) = \deg(A_c(s)) - \deg(A(s)) = 3-2 = 1$
- $R = R^{'}(s) \cdot B^+(s) = R^{'}(s) \cdot (s+1.69)$
- therefore, R'(s) is a constant and will be set equal to 1

(5) Solve Diophantine Equation

- $\deg(S(s)) \le \deg(R(s)) \Rightarrow \deg(S(s)) = 1$
- $$\underbrace{A(s) \cdot R^{'}(s) + B^-(s) \cdot S(s) = A_0(s) \cdot A_d(s)}_{\Downarrow}$$
  $$(s^2+0.13s+1.69) \cdot 1 + 1 \cdot (a_1 \cdot s + a_0) = 1 \cdot (s^2+2.12+9)$$
- $S(s) = 1.99 \cdot s + 7.31$

(6) Solve for T(s)

- $T(s) = A_0(s) \cdot B_d'(s) = 1 \cdot (s+9)$

Applying the equations R(s), S(s), and T(s) to Eq. **6.32**, the resulting frequency response reshaped by this MRC in Figure **6.33**.

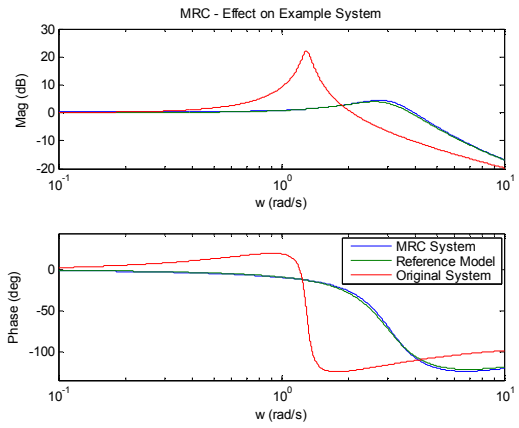

Figure **6.33**: Effect of MRC on the Example System

In order to test the robustness of the algorithm to parametric uncertainty, the controller is tested again with nominal system A(s) and B(s) being replaced with the terms from the "perturbed" system defined by Eq. **6.25**. One can see from the response of Figure **6.34** that, unlike the open-loop methods described previously, MRC is still able to produce results that are quite close to the desired response even with model perturbations away from nominal.

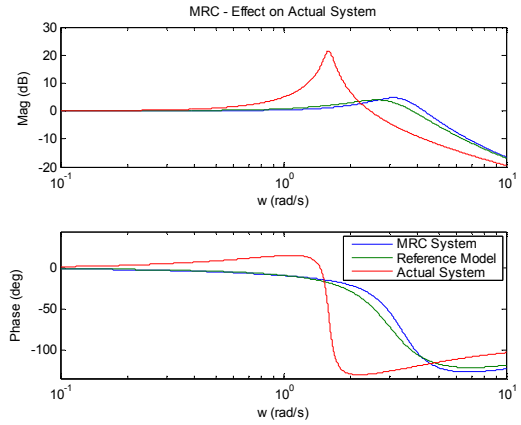

Figure **6.34**: Effect of MRC on the Actual System

Additionally, MRC will work on a system with unstable zeros. Applying the above design method to the following system:

$$\frac{y}{u} = \frac{s - 1.69}{\left(s^2 + 0.13s + 1.69\right)} \qquad \textbf{6.61}$$

results in $R(s) = (s - 1.69)$, with T(s) and S(s) remaining unchanged The bode plots of the open-loop and closed-loop responses using this controller are shown in Figure **6.35**.

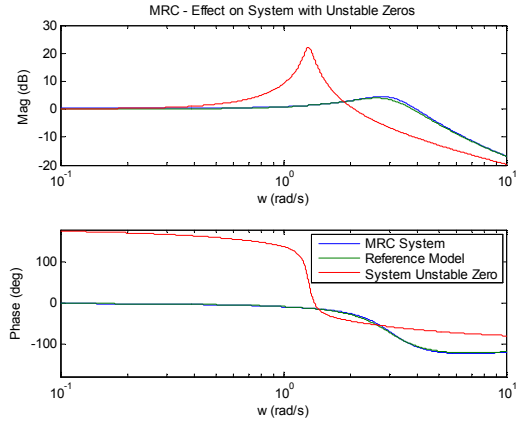

Figure **6.35**: Effect of MRC on a Plant with Unstable Zeros

6.2.2.1.1 Drawbacks of MRC

MRC will mitigate to a certain degree uncertainty in a plant, will work with systems that have unstable zeros. The only apparent drawback to using MRC is that the design procedure could become complicated for higher order systems, and the necessity of good system feedback.

6.3 Design of Control Methods to Mitigate Vehicle Rollover

This section will apply the above control methods to the High Roller. For a steering input, two driving maneuvers were used. The first maneuver is a sinusoidal excitation. By examining the frequency dependent wheel-lift and tire-slip limits for the High Roller at 30 m/s, it was determined that a sinusoidal input of $\omega = 8.2$ rad/s, amplitude equal to 0.1 rad would cause the suspension to produce a response at the wheel-lift limit. However, this same input will not cause the tires to saturate. Thus a sinusoidal input with the above frequency and amplitude specification will provide a good frequency-based comparison of the performance of each method.

The second test will be a pseudo-step response similar to the one executed on the Mercury Tracer in Chapter 5. The time specified for the rise and fall portion of the steering command is 0.25s each, with a maximum amplitude of 0.09 rad. This maneuver was chosen in order to gain a better qualitative understanding of the vehicle's performance.

For each of the control methods, the High Roller with and without control effort will be compared to the Mercury Tracer with all of the maneuvers being executed at 30

m/s. Also for each controller, a plot will be provided showing a comparison between the three vehicles plotting each state and the suspension restoring moment. An additional plot showing the global position of each of the vehicles will be provided in order to give a clearer picture of how the different controllers affect the lateral dynamics of the three vehicles. Ideally, they should all be approximately the same as the driver should not see major variations in vehicle drivability with the implementation of a roll-prevention controller.

6.3.1 Notch-Filter Implementation

The design methodology for the notch-filter is rather straightforward. As previously stated, the general control strategy is to make the High Roller behave in a similar manner to the Mercury Tracer. With this in mind, the frequency bounds for the notch-filter will be selected with the use of Figure 6.15.

By examining the curve at 40 m/s, it is seen that sinusoidal inputs ranging from 7.76 rad/s to 11.97 rad/s presents a risk for wheel lift. This range is determined by detecting the frequency dependent wheel-lift threshold crossover points. Using the MATLAB command *butter*, the second order Butterworth bandstop filter is given to be:

$$\frac{u'}{u} = \frac{s^4 + 185.8s^2 + 8629}{s^4 + 5.953s^3 + 203.5s^2 552.9s + 8629} \qquad 6.62$$

with the Bode plot:

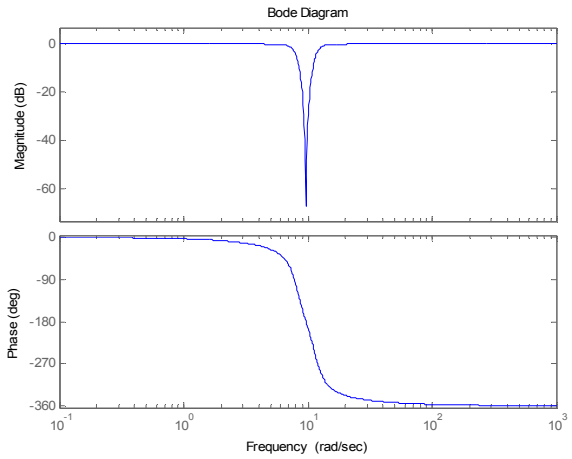

Figure 6.36: Bode Plot, 2nd Order Butterworth Bandstop Filter, 7.76 rad/s to 11.97 rad/s

The results for the sinusoidal excitation maneuver are shown below in Figure 6.37. The steering input is significantly altered, with both the magnitude and phase being affected. The phase is by far the more significant problem, since it introduces a lag in the response. Any lag will be detrimental to quickly responding to emergency events; a driver cannot determine in advance when an emergency will occur. However, the lag seen in the bandstop filter is expected as the frequency content of the maneuver is within the region influenced by the filter.

While the amplitude of the restoring moment is greatly reduced, the lateral dynamics of the High Roller with filtering are significantly different from both the High Roller without filtering and the Mercury Tracer. The aggregated result of these differences may be seen when looking at the global position of the three vehicles, shown below in Figure 6.38. Here, it is clear that the notch-filter causes the High Roller with filtering to travel in nearly a straight line, with very little of the serpentine motion exhibited by the other two.

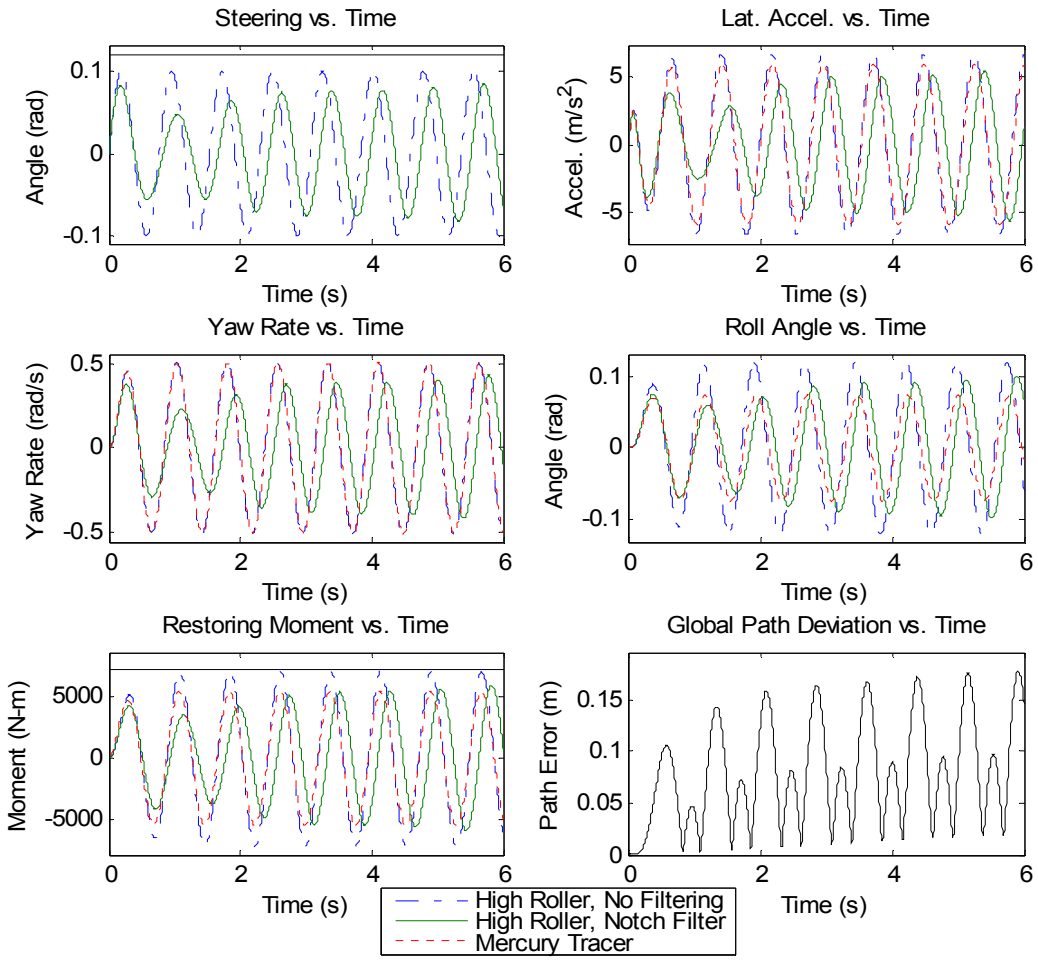

Figure **6.37**: Results of the Notch Filter, Individual States, Sinusoidal Excitation, 8.2 rad/s, 0.1 rad amplitude

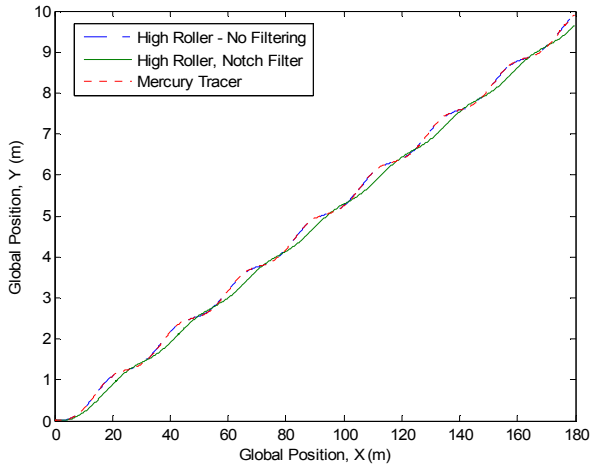

Figure **6.38**: Results of the Notch-Filter, Global Position, Sinusoidal Excitation, 8.2 rad/s, 0.1 rad amplitude

Comparison of the response of the individual states for the pseudo-step maneuver (Figure **6.39**) shows that the High Roller with filtering actually has an increased maximum roll moment and roll angle than the High Roller without filtering. With filtering, the maximum roll moment of the High Roller is 5,894 N-m as opposed to 5,703 N-m for the unfiltered version. While this is a relatively small difference, it shows that the notch-filter is not an apt choice for rollover mitigation.

When comparing the global position of the filtered vehicle to the other two (Figure **6.40**), it is seen that the High Roller without filtering follows nearly the same path as the Mercury Tracer. However, the path of the filtered vehicle is approximately 1.73 m apart from the Mercury Tracer. This was determined by taking the maximum distance found between the two vehicle paths at each time step. Such a deviation is greater than the width of the vehicle (1.43 m), and is likely not desirable in an emergency situation.

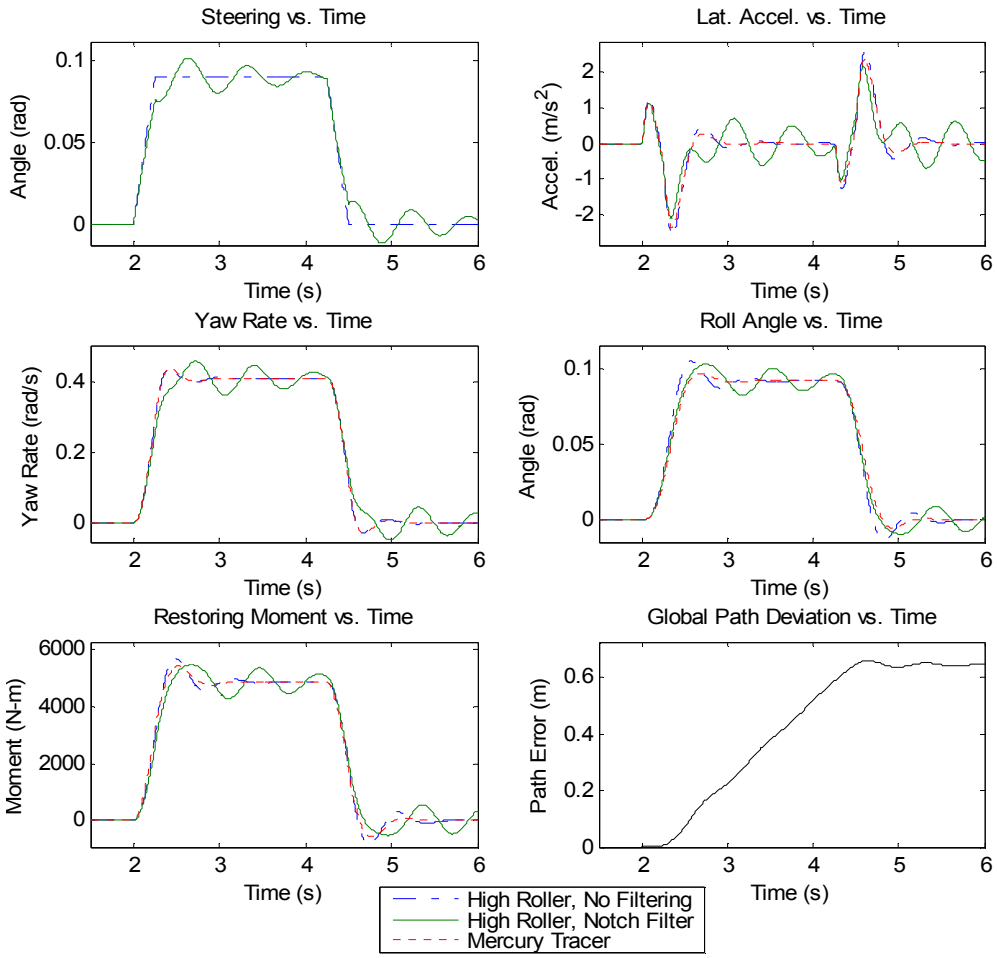

Figure **6.39**: Results of the Notch Filter, Individual States, Pseudo-Step, 0.09 rad amplitude, 30 m/s

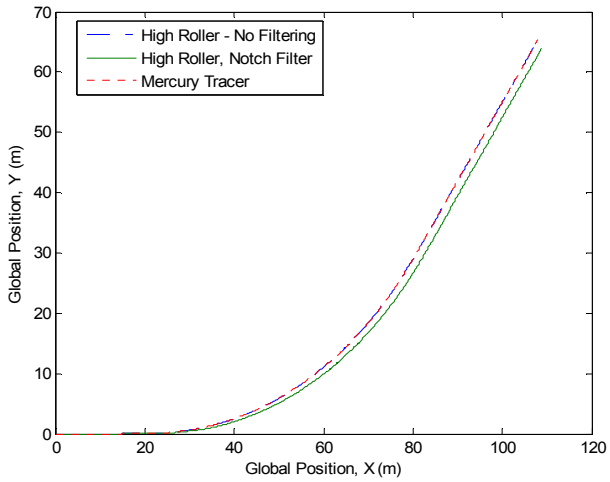

Figure 6.40: Results of the Notch Filter, Global Position, Pseudo-Step, 0.09 rad amplitude, 30 m/s

As a result of these observations, it is clear that the use of a notch filter is not necessarily the best choice for rollover mitigation. The primary reason for this is that the filter significantly reduces the effect of a portion of the steering response while adding phase to it. While selecting a narrower band for the filter would help with this, it would not solve it, since the problem is inherent to the filter. Additionally, while making the filtered band narrower will reduce this problem, it will also begin to have little or no effect on some of the critical frequencies.

6.3.2 Pole Cancellation Implementation

For the design of the pole cancellation filter, it is necessary to first define the pole(s) that need to be cancelled. Examination of Figure 6.15 shows that the poles will be complex and have a natural frequency of approximately 9.5 rad/s. Solving for the poles of the High Roller at 30 m/s shows that the filter needs to cancel out the complex

pair -2.9984 ± 9.4883i. These have a natural frequency of ω_n= 9.95 rad/s, and a damping ratio of ξ = 0.3.

For the Mercury Tracer, the complex pole pair closest to the complex pair for the High Roller specified above is -4.6978 ± 8.2499i. This gives rise to a natural frequency of ω_n=9.5 rad/s and a damping ratio of ξ = 0.5. Therefore, the pole cancellation filter will be:

$$\frac{u'}{u} = \frac{(s + 2.9984 \pm 9.4883i)}{(s + 4.6978 \pm 8.2499i)} \cdot 0.91 = \frac{0.91 \cdot (s^2 + 5.997s + 99.02)}{(s^2 + 9.396s + 90.13)} \qquad \textbf{6.63}$$

where the gain of 0.91 is applied to ensure that the DC gain of the filter is zero. The bode plot of the filter is:

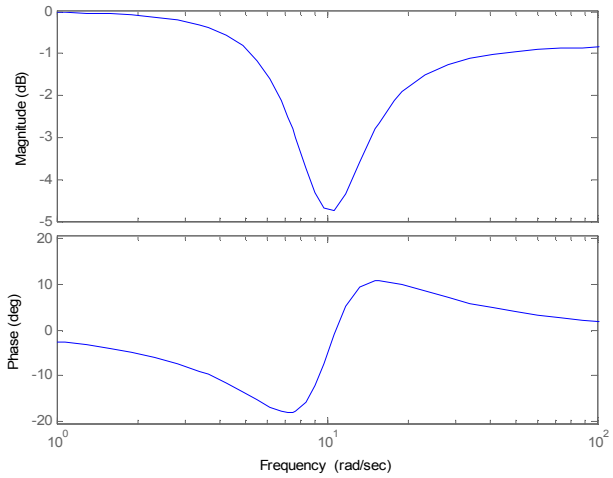

Figure **6.41**: Pole Cancellation Filter, High Roller

The results for the sinusoidal excitation are shown below, with the individual states shown in Figure **6.42** and the global position shown in Figure **6.43**. It is evident from examining the roll dynamics that the High Roller with filtering nearly matches the

response of the Mercury Tracer. However, the magnitude of the response of the lateral dynamics appears to be significantly lower by comparison.

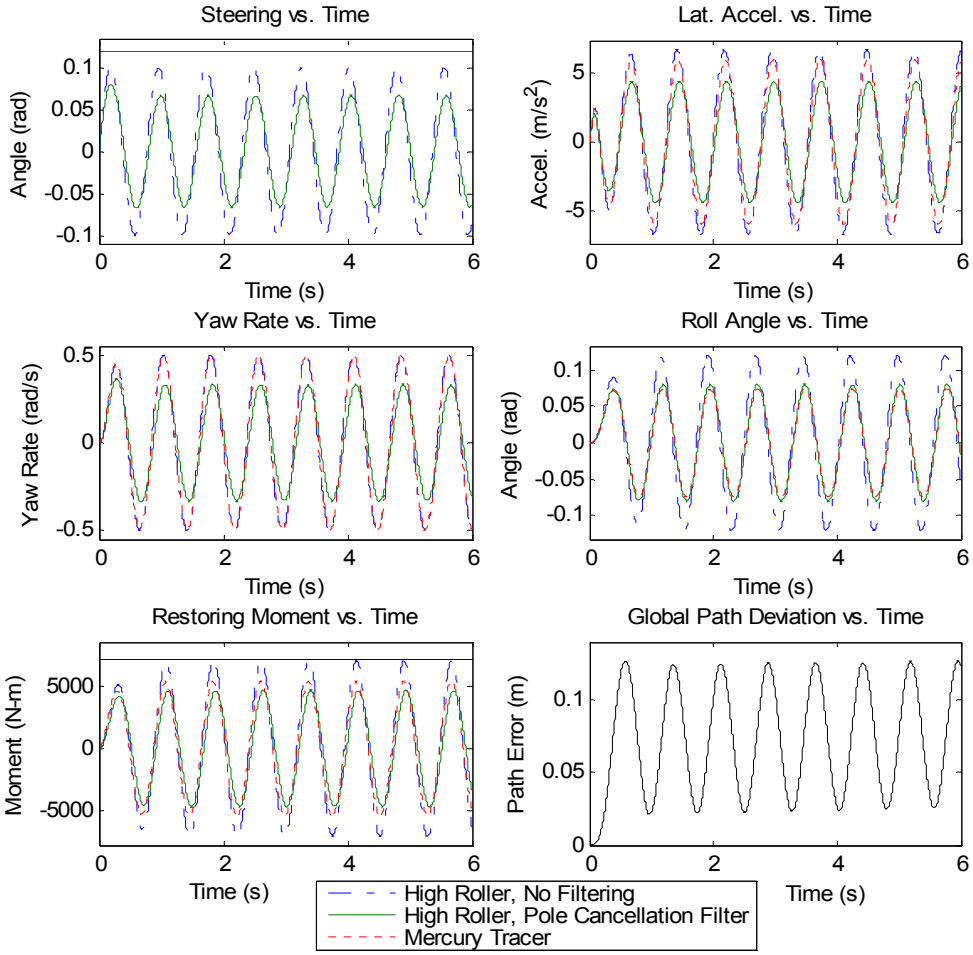

Figure **6.42**: Results of the Pole Cancellation Filter, Individual States, Sinusoidal Excitation, 8.2 rad/s, 0.1 rad amplitude

When the global positions are compared, however, the largest distance between the Tracer and the filtered vehicle is only 14 cm. Such a difference is acceptable, as it is an order of magnitude smaller than the width of the vehicle.

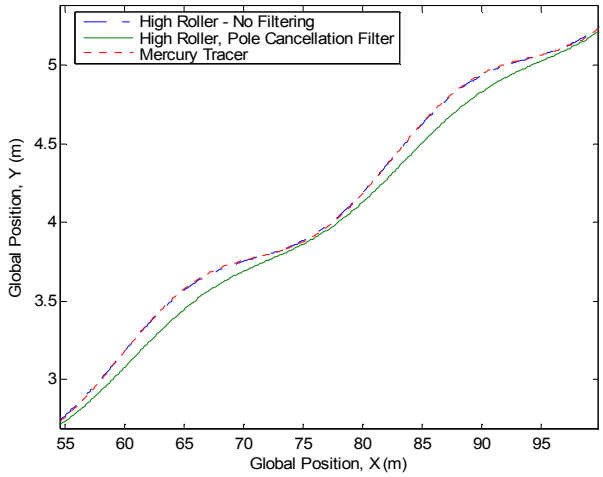

Figure **6.43**: Results of the Pole Cancellation Filter, Global Position (Zoomed), Sinusoidal Excitation, 8.2 rad/s, 0.1 rad amplitude

When executing the step response, the results are equally favorable when examining the response of the states (Figure **6.44**). Every response shows much more damping in the filtered vehicle than in the unfiltered vehicle. As with the sinusoidal response, the roll moment and roll angle of both the Tracer and the filtered vehicle are nearly identical. The method falls short, however, when comparing the global positions of the two cars. The path of the filtered vehicle under a pseudo-step input differs by as much as 1.18m – nearly the width of the vehicle.

Given the generally good performance of the pole cancellation filter, it would seem to be a fair choice for use in rollover mitigation. The major shortcomings of the method are a slight decrease in lateral response resulting in the high path deviation seen in the step response and sensitivity to model uncertainty (as described above). However, the method does produce a much more favorable roll response when compared to the unfiltered High Roller.

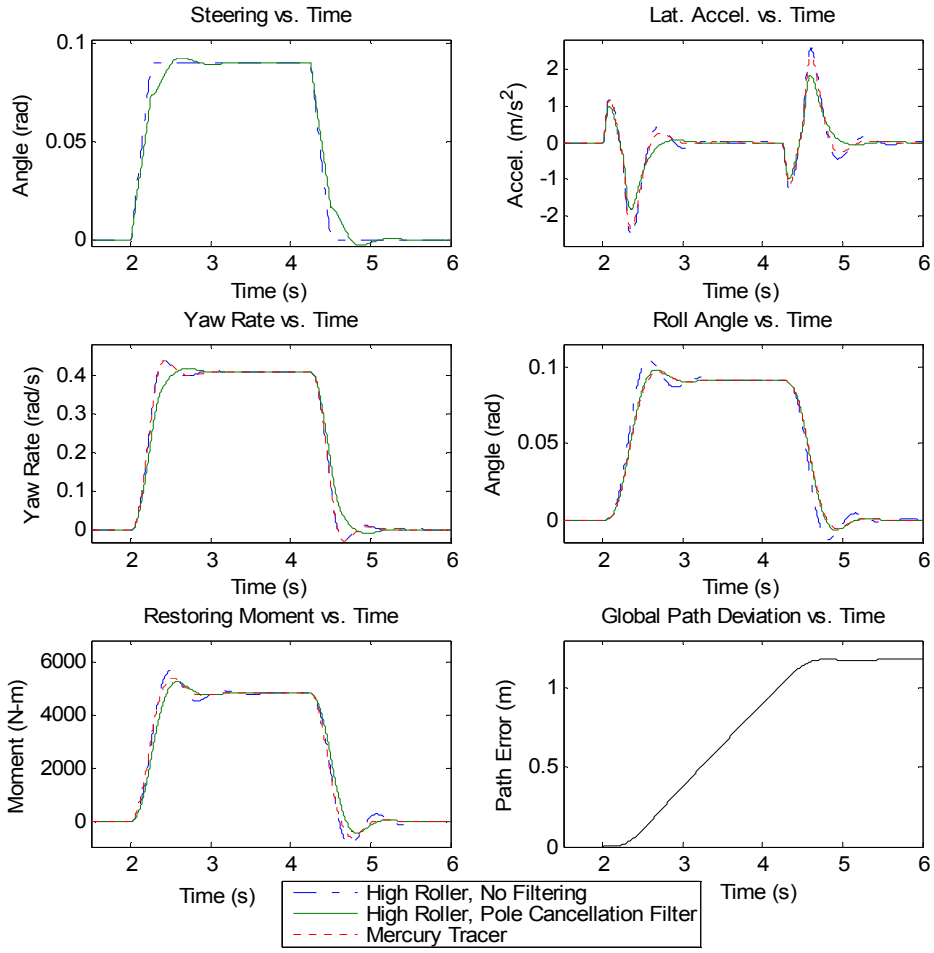

Figure **6.44**: Results of the Pole Cancellation Filter, Individual States, Pseudo-Step, 0.09 rad amplitude, 30 m/s

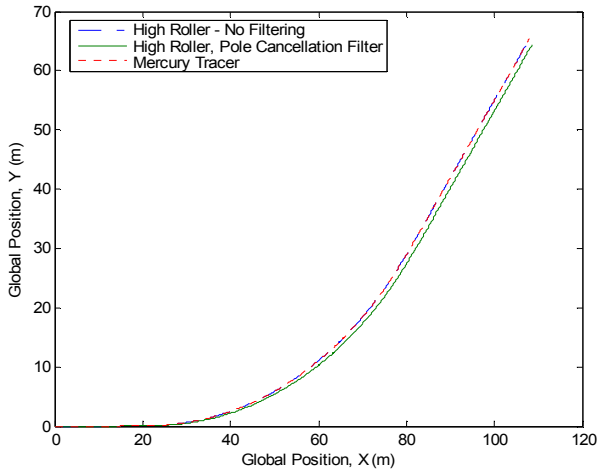

Figure **6.45**: Results of the Pole Cancellation Filter, Global Position, Pseudo-Step, 0.09 rad amplitude, 30 m/s

6.3.3 Dead-Beat Controller

Following the same design strategy as the pole-cancellation filter, the dead-beat controller will be designed such that it completely cancels out the existing roll moment response:

$$\frac{B(s)}{A(s)} = \frac{(s+17.67)\cdot(s+5.258\pm13.23i)}{(s+10.191\pm7.291i)\cdot(s+2.998\pm9.488i)} \qquad \textbf{6.64}$$

and replaces it with the roll moment response of the Mercury Tracer:

$$\frac{B_d(s)}{A_d(s)} = \frac{(s+8.833)\cdot(s+5.258\pm7.291i)}{(s+12.067\pm7.291i)\cdot(s+4.698\pm8.25i)} \qquad \textbf{6.65}$$

This makes the deadbeat controller simply:

$$\frac{u'}{u} = \frac{(s+8.833)\cdot(s+5.258\pm7.291i)}{(s+12.067\pm7.291i)\cdot(s+4.698\pm8.25i)}\cdot\frac{(s+10.191\pm7.291i)\cdot(s+2.998\pm9.488i)}{(s+17.67)\cdot(s+5.258\pm13.23i)}\cdot 2 \qquad \textbf{6.66}$$

where the constant gain of 2 is applied such that the DC gain of the filter is zero. The bode plot of this filter is shown below:

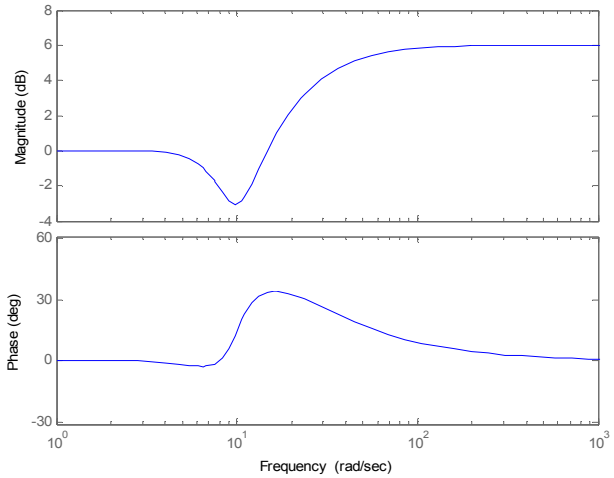

Figure **6.46**: Bode Plot, Deadbeat Filter

Not surprisingly, the roll moment response (Figure **6.47**) of the High Roller with filtering matches the response of the Mercury Tracer identically. There is also a noted decrease in the roll angle of the filtered vehicle from the unfiltered High Roller. Finally, while the filtered vehicle shows a reduced magnitude response in the lateral dynamics, the global position of the three vehicles (Figure **6.48**) is nearly identical, with the maximum deviation of the filtered vehicle from the path of the Mercury Tracer to be 5 cm.

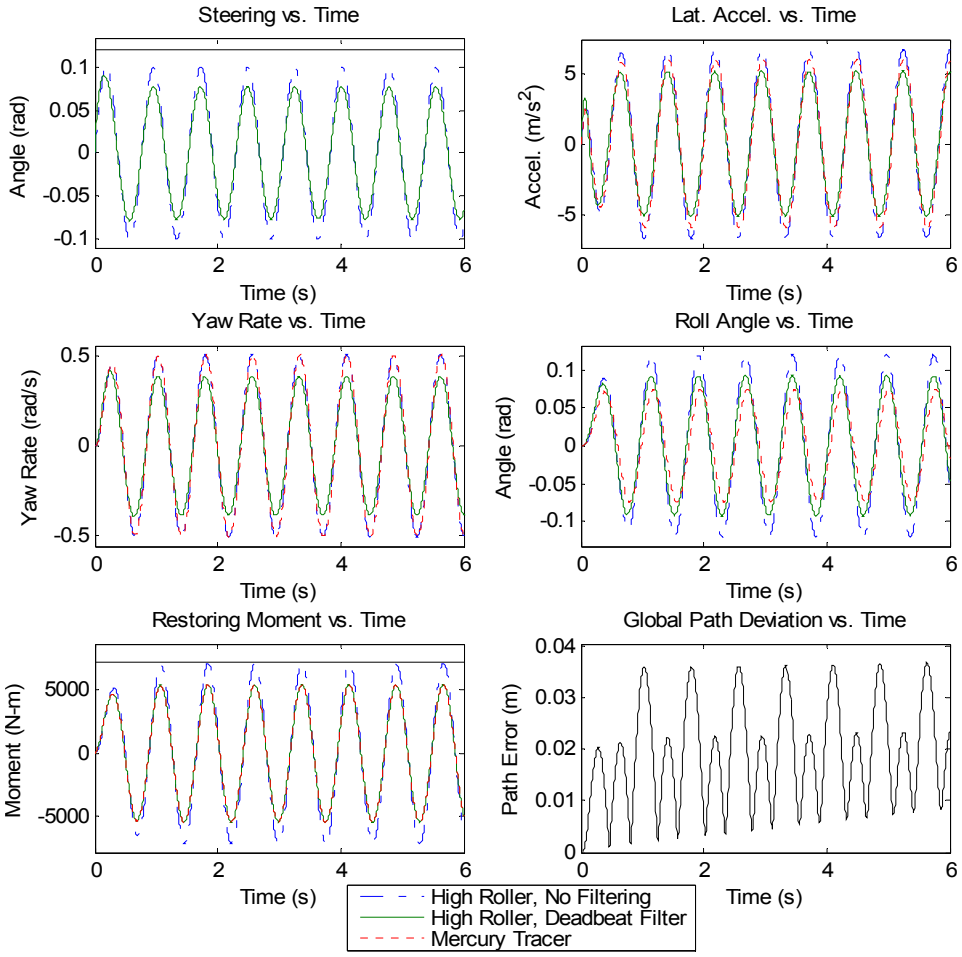

Figure **6.47**: Results of the Deadbeat Filter, Individual States, Sinusoidal Excitation, 8.2 rad/s, 0.1 rad amplitude

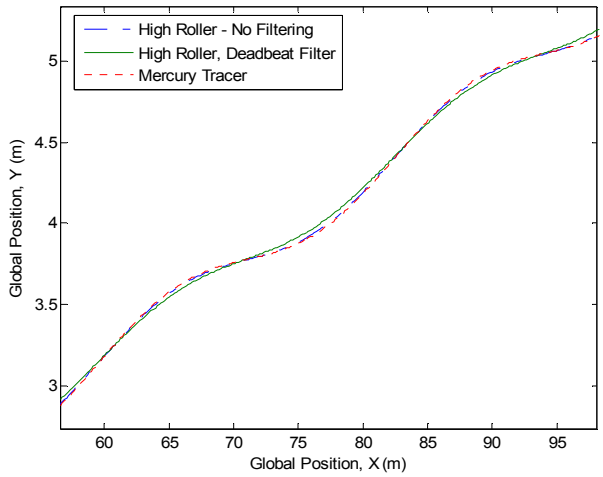

Figure **6.48**: Results of the Deadbeat Filter, Global Position (Zoomed), Sinusoidal Excitation, 8.2 rad/s, 0.1 rad amplitude

For the step response, the roll moment response for the filtered vehicle and the Tracer are again identical (Figure **6.49**). It is interesting to note that the maximum magnitude of the roll angle response for both versions of the High Roller are nearly identical, but the filtered version has much better damping. The lateral dynamics are also very well damped.

A comparison of the global positions of the three vehicles (Figure **6.50**) also shows that the vehicle under deadbeat control responds in a nearly identical manner to the other two vehicles. The maximum deviation found between the Tracer and the filtered vehicle was only 11 cm. Such a difference is acceptable, as it is less than an order of magnitude smaller than the width of the vehicle.

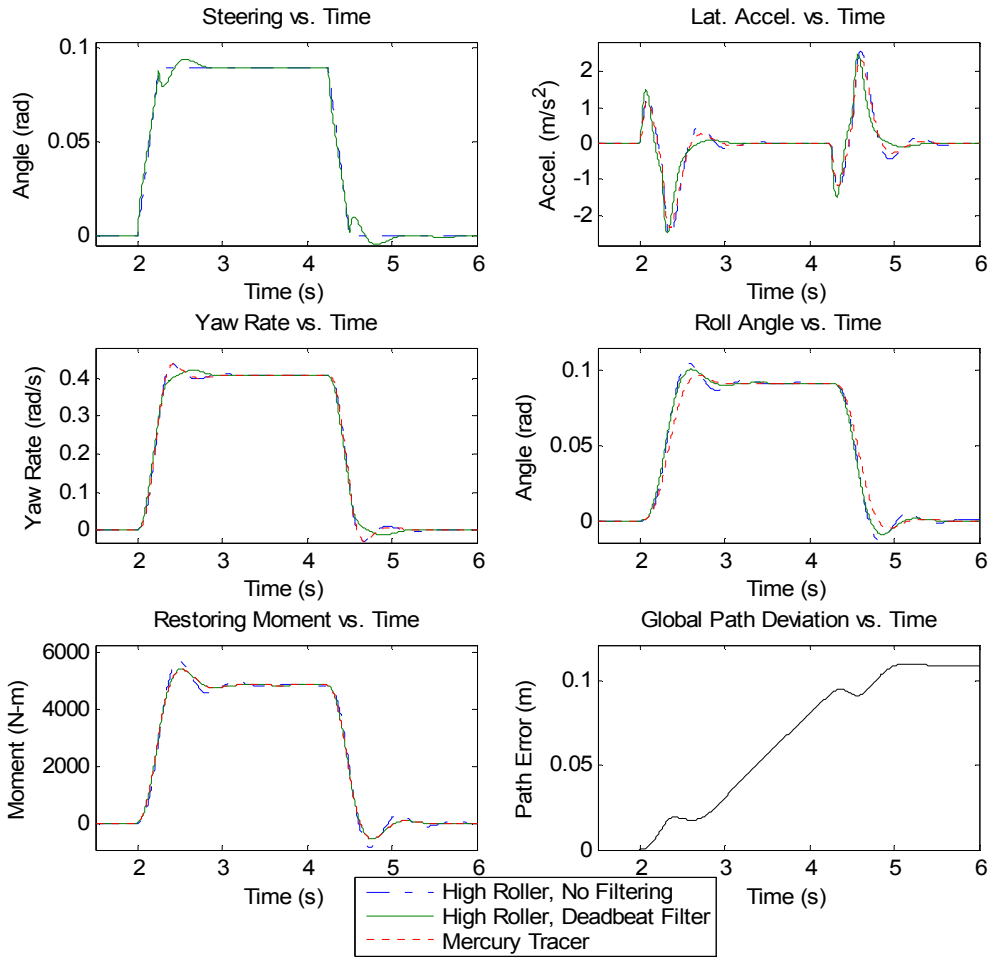

Figure **6.49**: Results of the Deadbeat Filter, Individual States, Pseudo-Step, 0.09 rad amplitude, 30 m/s

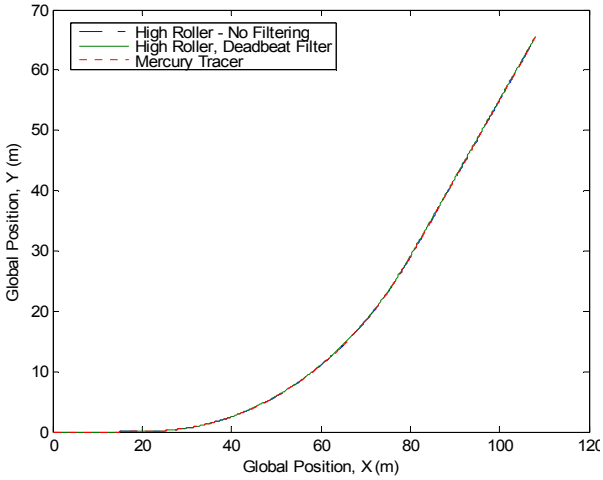

Figure **6.50**: Results of the Deadbeat Filter, Global Position, Pseudo-Step, 0.09 rad amplitude, 30 m/s

At first glance, it would appear that the deadbeat controller is an excellent choice for rollover mitigation. One must be cautioned by the fact that these results are only valid under the assumption of perfect model knowledge – something that is not likely in the real world. However, its relative simplicity makes it an attractive option.

6.3.4 Model-Reference Control Implementation

As stated previously, the goal of model reference control is to change the input-output characteristics of a plant or portion of the plant to have more desirable characteristics specified by the designer. In the case of the High Roller, the design has focused on the relationship of steering input to restoring moment on the suspension. As indicated in Figure **6.15**, the High Roller begins to show a risk of wheel-lift at approximately 20 m/s. In order to improve its performance to be more like the Mercury Tracer, the reference model will be the transfer function of steering input to restoring

moment of the Mercury Tracer at 30 m/s (Eq. **6.67**) and the plant will be the transfer function of steering input to restoring moment of the High Roller at the same speed (Eq. **6.68**).

$$\frac{B_d(s)}{A_d(s)} = \frac{(s+8.833)\cdot(s+5.258\pm 7.291i)}{(s+12.067\pm 7.291i)\cdot(s+4.698\pm 8.25i)} \qquad \textbf{6.67}$$

$$\frac{B(s)}{A(s)} = \frac{(s+17.67)\cdot(s+5.258\pm 13.23i)}{(s+10.191\pm 7.291i)\cdot(s+2.998\pm 9.488i)} \qquad \textbf{6.68}$$

The procedure to solve for the controller will follow the steps outlined in Section **6.2.2.1.1** and is as follows:

(1) Check compatibility

- $\deg(A_d(s)) = \deg(A(s)) \Rightarrow$

  $\deg((s+12.067\pm 7.291i)\cdot(s+4.698\pm 8.25i)) = \deg((s+10.191\pm 7.291)\cdot(s+2.998\pm 9.488i))$
- $\deg(B_d(s)) = \deg(B(s)) \Rightarrow$

  $\deg((s+8.833)\cdot(s+5.258\pm 7.291i)) = \deg((s+17.67)\cdot(s+5.258\pm 13.23i))$

(2) Define components of B(s) and $B_d(s)$

- $B(s) = B^+(s)\cdot B^-(s)$
- $B^+(s) = (s+17.67)\cdot(s+5.258\pm 13.23i)$
- $B^-(s) = 1$
- $B_d(s) = B^-(s)\cdot B_d'(s)$
- $B_d'(s) = (s+8.833)\cdot(s+5.258\pm 7.291i)$

(3) Find $A_0(s)$ and $A_c(s)$

- $\deg(A_0(s)) = \deg(A(s)) - \deg(B^+(s)) - 1 = 4-3-1 = 0$
- choose $A_0(s) = 1$
- $A_c(s) = A_0(s)\cdot A_d(s)\cdot B^+(s) =$

  $1\cdot(s+12.067\pm 7.291i)\cdot(s+4.698\pm 8.25i)\cdot(s+17.67)\cdot(s+5.258\pm 13.23i)$

(4) Solve for R(s)

- $\deg(R(s)) = \deg(A_c(s)) - \deg(A(s)) = 7 - 4 = 3$
- $R = R'(s) \cdot B^{+}(s) = R'(s) \cdot (s + 17.67) \cdot (s + 5.258 \pm 13.23i)$
- therefore, R'(s) is a constant and will be set equal to 1

(5) Solve Diophantine Equation

- $\deg(S(s)) \leq \deg(R(s)) \Rightarrow \deg(S(s)) = 3$

$$\underbrace{A(s) \cdot R'(s) + B^{-}(s) \cdot S(s) = A_0(s) \cdot A_d(s)}_{\Downarrow}$$

- $(s + 10.191 \pm 7.291) \cdot (s + 2.998 \pm 9.488i) \cdot 1 + 1 \cdot (a_3 \cdot s^3 + a_2 \cdot s^2 + a_1 \cdot s + a_0) =$
  $1 \cdot (s^2 + 2.12 + 9) \cdot (s + 12.067 \pm 7.291i) \cdot (s + 4.698 \pm 8.25i)$
- $s^4 + (26.38 + a_3)s^3 + (402.2 + a_2)s^2 + (3103 + a_1)s + (1.791 \times 10^4 + a_0) =$
  $s^4 + 33.53s^3 + 515.6s^2 + 4043s + 1.791 \times 10^4$
- $S(s) = 7.15s^3 + 113.4s^2 + 940s$

(6) Solve for T(s)

- $T(s) = A_0(s) \cdot B_d'(s) = 1 \cdot (s + 8.833) \cdot (s + 5.258 \pm 7.291i)$

It is important to note that in Step 5, the coefficients of the terms in *A(s)* must be smaller or equal in order than the corresponding coefficients of $A_d(s)$ in order for the feedback portion of the controller to be stable. Additionally, the order of *S(s)* should be one degree less than the order of $A_d(s)$ in order for it to be able to influence every one of the coefficients of *A(s)*.

The results of this controller are shown below in Figure **6.51** (individual states) and in Figure **6.52** (global position). The High Roller with and without MRC are compared to the Mercury Tracer, with all three vehicles responding to a sinusoidal excitation of ω = 8.2 rad/s, amplitude equal to 0.1 rad.

Note that in Figure **6.51** the predicted steering limit for tire saturation is indicated in the steering angle vs. time plot and the predicted wheel-lift limit is shown in the restoring moment vs. time plot, both as black lines. It may be seen that the restoring moment of the High Roller with MRC matches the restoring moment of the Mercury Tracer. While the High Roller without MRC comes up to the predicted wheel-lift limit, both the Tracer and the steer-by-wire vehicle do not.

The effect of MRC on the vehicle states is shown as well, and a more qualitative comparison may be obtained in Figure **6.52**. When examining the global position of each of the vehicles, there is very little apparent difference. However, the sinusoidal excitation does not command the vehicle to move very much in the lateral direction, and the differences between the path traveled by the MRC vehicle and the other two may appear to be more significant in maneuvers that command more of a net change in lateral position.

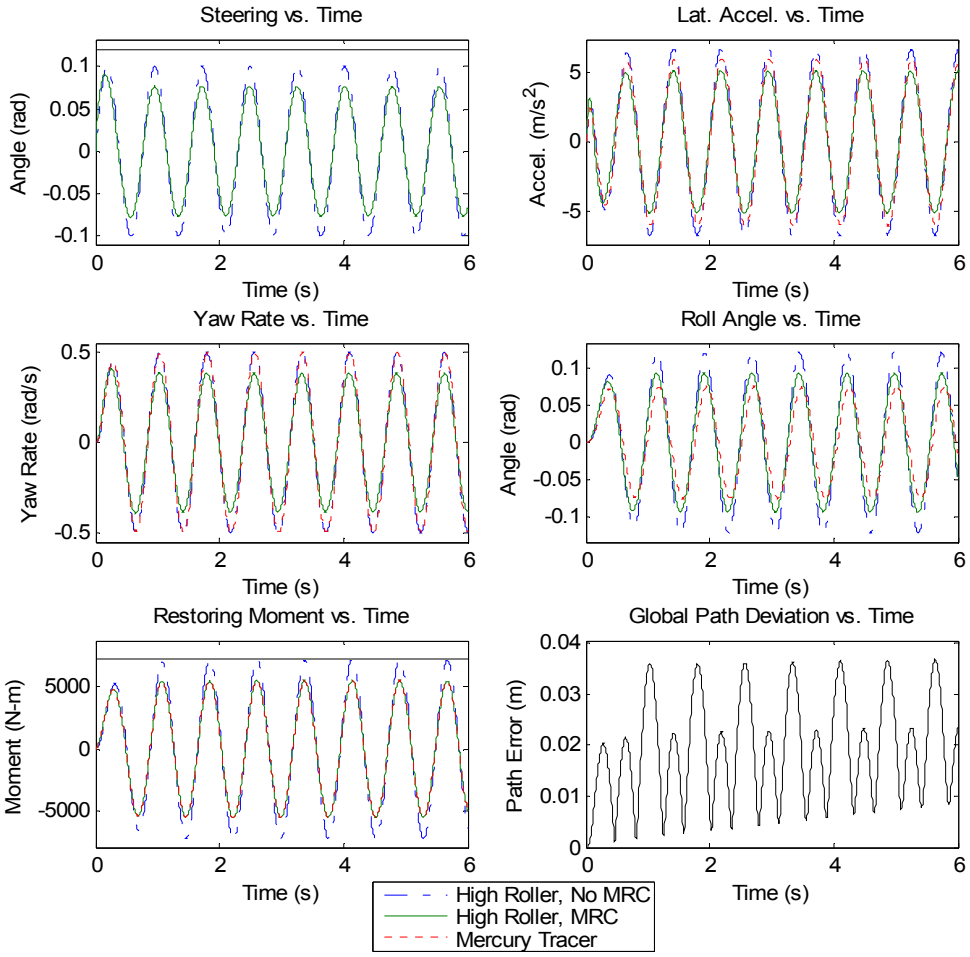

Figure **6.51**: Results of the Model Reference Controller, Individual States, Sinusoidal Excitation, 8.2 rad/s, 0.1 rad amplitude

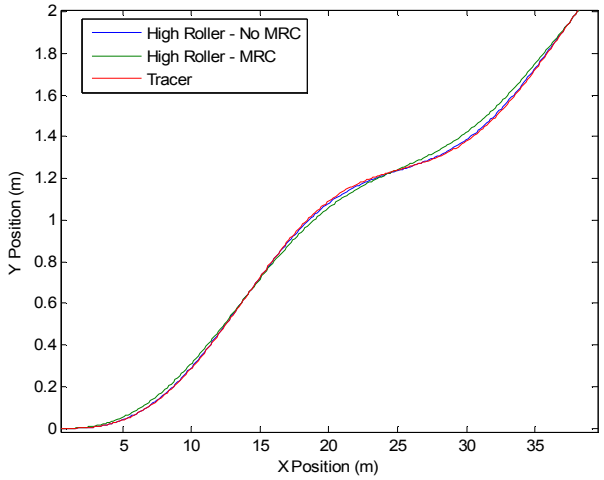

Figure **6.52**: Results of the Model Reference Controller, Global Position (Zoomed), Sinusoidal Excitation, 8.2 rad/s, 0.1 rad amplitude

In order to gain a better qualitative understanding of the MRC vehicles performance, a pseudo-step response was executed in simulation. As with the sinusoidal excitation shown above, the individual states are plotted vs. time below in Figure **6.53**.

It is readily seen that while the magnitude of the response for all three vehicles is roughly similar, the High Roller with MRC and the Mercury Tracer both exhibit significantly better damped responses than the High Roller without MRC. The lateral dynamics of the High Roller with MRC appear to be more damped than the dynamics of the Mercury Tracer as well.

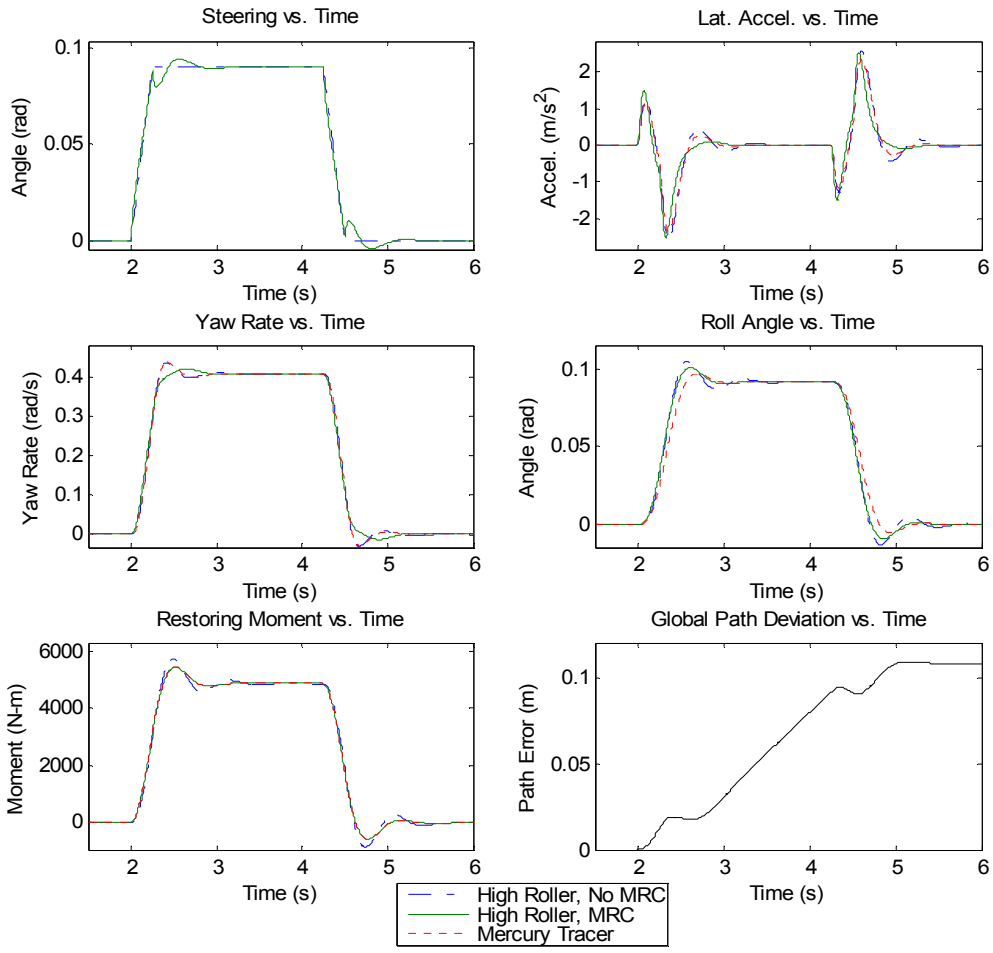

Figure **6.53**: Results of the Model Reference Controller, Individual States, Pseudo-Step, 0.09 rad amplitude, 30 m/s

Given the similarity in the response of the individual states between the vehicles, it is not surprising that the position of one vehicle in the world is nearly indistinguishable from the others. Figure **6.54** shows both the total maneuver and the area around the point of execution. Numerically, the deviation between the High Roller with MRC and the other two vehicles is approximately 11 cm.

From these results, it is reasonable to assume that the High Roller with MRC will have the desired results of having an underdamped vehicle respond as if it were well

damped while having little to no obvious decrease in lateral response. Given the relatively simple structure of this controller, combined with its favorable performance, it seems a good choice for rollover mitigation.

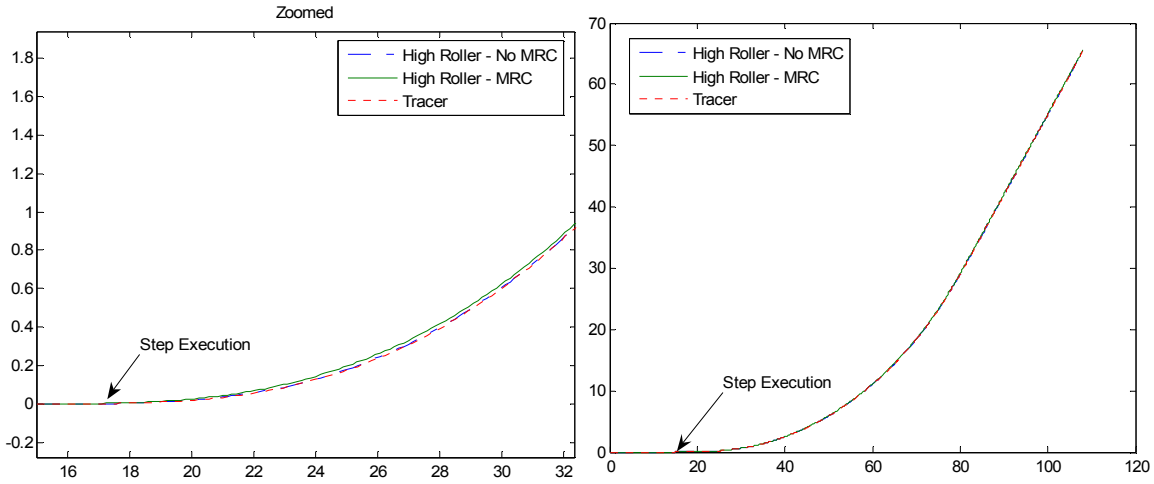

Figure 6.54: Results of the Model Reference Controller, Global Position, Pseudo-Step, 0.09 rad amplitude, 30 m/s

6.3.5 The Effect of Parametric Uncertainty on the Model Reference and Deadbeat Control Implementations

In order to gain a better understanding of how uncertainty will affect MRC and deadbeat control, a simulation was performed in which parametric error was introduced. The premise of the simulation is that the vehicle is weighed down with an additional mass placed over the rear axle. The addition of this mass caused the overall mass of the vehicle to be increased by 25%, with a corresponding increase in the sprung mass. As a result, the planar location of the CG was recalculated. The yaw and roll inertial properties were also changed by using the parallel axis theorem and the new CG location.

Finally, both the front and rear cornering stiffness values were increased by 25% to account for the additional weight on the vehicle. This was done to simulate a vehicle containing a significant in the trunk.

In this example, the same pseudo-step was used as described in the previous sections. Additionally, the MRC and deadbeat control parameters were not changed from the original designs obtained from the plant without parametric uncertainty. The results are shown below in Figure **6.55** and Figure **6.56**

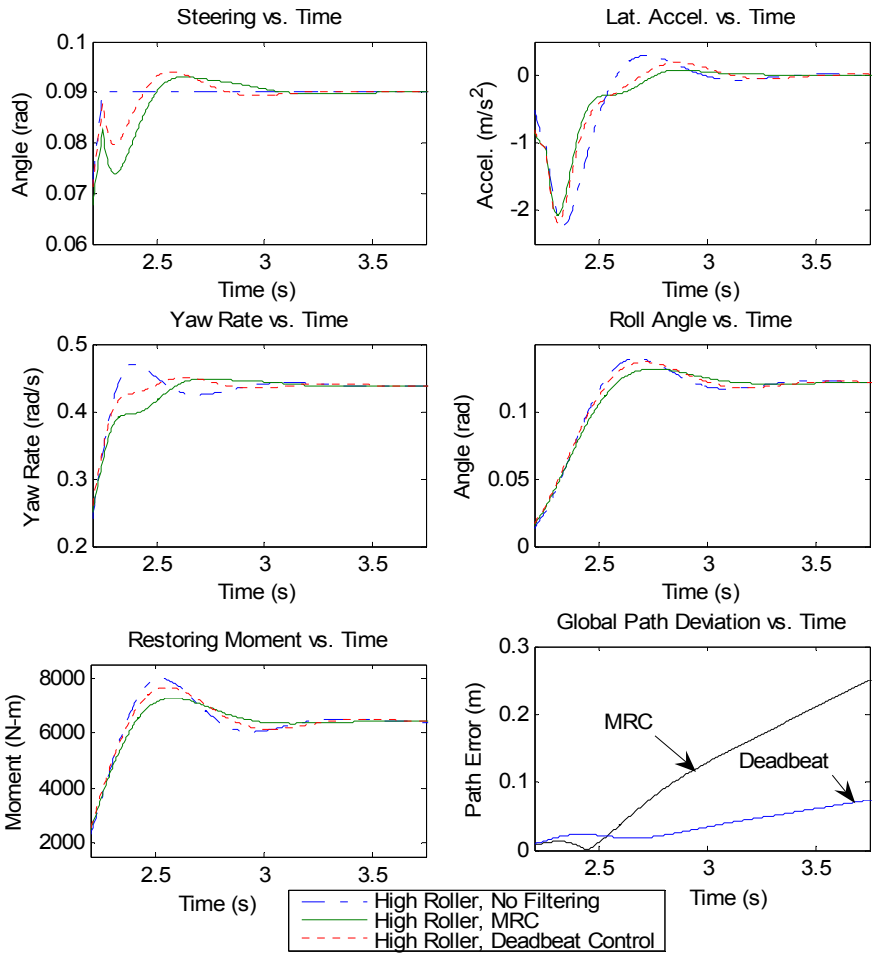

6.55: Results of MRC and Deadbeat Control with Model Uncertainty, Individual States, Pseudo-Step, 0.09 rad amplitude, 30 m/s

Examination of the individual states shows that the roll angle response is nearly identical for both vehicles. Regarding the yaw rate and lateral acceleration, the only apparent difference is that the High Roller with MRC has a more damped response than the High Roller with deadbeat control. From the driver's perspective, the vehicle with MRC may appear to have better ride comfort as the response is slightly smoother in the yaw and roll states.

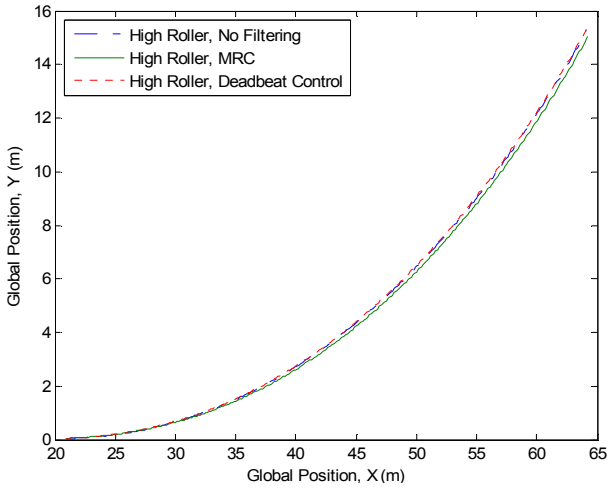

6.56: Results of MRC and Deadbeat Control with Model Uncertainty (zoomed), Global Position, Pseudo-Step, 0.09 rad amplitude, 30 m/s

Examination of the resulting global position of the vehicle under both controllers shows that there is virtually no difference in performance. Numerically, the maximum deviation found for the High Roller with MRC was 0.4m, and 0.12m for the High Roller with deadbeat control. This is somewhat surprising as the open-loop control method exhibited far more sensitivity to model uncertainty in the example shown in Section **6.2.1.3.2**. However, both deviations are still acceptable.

6.4 Concluding Remarks

This chapter presented a methodology for predicting when a vehicle may be at risk for wheel-lift prior to sliding. Additionally, multiple control strategies were presented that use the information derived from this method to mitigate vehicle rollover under the assumption of an existing steer-by-wire system. The wheel-lift prediction methodologies give a sense of a vehicle's dynamic rollover propensity, provide insight into the roll dynamics of the vehicle that may not be garnered from examination of the response from the individual states alone, and may lead to better automotive designs in regards to roll dynamics.

Reviewing the control methods, it is clear that the notch-filter is not an acceptable control method for rollover mitigation. It has both a negative impact on the lateral dynamics and at times *increases* the roll moment on the vehicle, as opposed to reducing it. While the pole cancellation filter does not possess this characteristic, the effect it has on a vehicles lateral dynamics also brings its usefulness into question.

Following these two methods, both the deadbeat controller and the MRC showed excellent performance. The roll moment and angles were reduced and showed much better damping for both controllers. Additionally, the global positions for each were comparable and had little apparent difference to the Tracer.

An interesting result came from comparing the performance of both MRC and deadbeat control to a vehicle with parametric uncertainty. While this result may not have been readily apparent from basic knowledge of the two control methods, it makes the necessity for sensitivity analysis of the plant to parametric uncertainty clear. However,

while deadbeat control showed better adherence to the intended path, MRC may be the superior choice as a result of its smoother response from the standpoint of ride comfort.

In light of these results, a trade-off must be made between complexity, path error, and ride comfort. In order to implement the MRC algorithm, one needs to detect the roll moment acting on the vehicle. While this may be done by sensing the suspension displacement and velocity, there may be considerable error in the measurement. If sufficiently large, this sensor error may further degrade the performance of the algorithm when compared to deadbeat control, and must be weighed against model uncertainty and the benefit of added ride comfort.

It should be noted that actual implementation of both MRC and deadbeat control would require that the equations include speed as a variable and have it fed back into the controller. Such sensing abilities are all ready included in all modern automobiles and therefore would not require any additions to the vehicle setup beyond the controller itself. However, it may make the implementation of MRC rather difficult given the complexity of its derivation and the additional sensing requirements on the roll moment of the vehicle.

[1] H.-J. Kim, H. S. Yang, and Y.-P. Park, "Robust roll control of a vehicle: experimental study using a hardware-in-the-loop set-up," *Proceedings of the Institution of Mechanical Engineers, Part D (Journal of Automobile Engineering)*, vol. 216, pp. 1-9, 2002.

[2] J. C. Dixon, *Tires, Suspension, and Handling*, 2nd ed. Warrendale, PA: The Society of Automotive Engineers (SAE), 1996.

[3] B.-C. Chen and H. Peng, "Differential Braking Based Rollover Prevention for Sport Utility Vehicles with HIL Evaluations," *Vehicle System Dynamics*, vol. 36, pp. 359-389, 2001.

[4] "Consumer Information; New Car Assessment Program; Rollover Resistance," National Highway Traffic Safety Administration (NHTSA) Docket No. NHTSA-2001-9663; Notice 3, 2001.

[5] S. Skogestad and I. Postlethwaite, *Multivariable Feedback Control: Analysis and Design*. West Sussex, England: John Wiley & Sons Ltd., 1996.

[6] B. C. Kuo, *Automatic Control Systems*, 7 ed. West Sussex, England: John Wiley & Sons Ltd., 1995.

[7] C. J. Astrom and B. Wittenmark, *Adaptive Control*: Addison-Wesley Publishing Company, 1995.

Chapter 7

Conclusions

The conclusions for this thesis will be divided into the following subsections: general conclusions from the thesis, conclusions regarding vehicle modeling assumptions and procedures, conclusions specific to the wheel-lift prediction method developed, and conclusions pertaining to the wheel-lift mitigation techniques tried. A discussion on future work that should be pursued in this area will then follow.

7.1 General Conclusions

It has been shown that a relatively simple dynamic model is capable of modeling both the planar and roll dynamics of a vehicle well under constant speed conditions. While this model is subjected to additional constraints on account of it being linear, it may be used to predict the propensity of a vehicle to rollover with regard to specific input frequencies. Finally, this information may be used in conjunction with relatively simple control algorithms to greatly improve a vehicle's dynamic handling, with little notice to the driver.

Another interesting conclusion is that relatively accurate measurements may be taken of a vehicle's dynamics with relatively inexpensive commercial grade sensors. While more expensive equipment would clearly produce better results in areas such as lateral acceleration, it is clear the data provided by the commercial grade equipment is

still largely useful. This is an important result as it shows that the roll dynamics of a vehicle may be seen with inexpensive, automotive grade equipment. Such sensors are commonly packaged in production vehicles. Additionally, experimental vehicle dynamics studies may be performed on even a highly restrictive budget provided the investigator has access to the appropriate facilities to conduct such research.

7.2 Conclusions Regarding the Modeling of Vehicle Chassis Dynamics

One of the most important results from the comparison between the various models used in this study is that, while parameters such as cornering stiffness, roll stiffness, and roll damping are difficult to directly measure, approximations may be easily found using the methods described in this work. This is a result of the conclusion that a complex plant description is not necessary to accurately describe the roll dynamics of a vehicle.

The fact that a complex or high order model is not required is readily shown by the data presented in Chapter 5, where the predicted roll rate response in both the frequency and time-domain match the measured data well. If the models used in this study were more complex and/or of higher order, additional parameters that are difficult to measure would be required. Such parameters include tire damping as in [1], the location of the mass center of the sprung mass and the unsprung mass as in [2], and the angle of inclination of the roll axis as in [2-4]. If such parameters were required, additional tests to determine them would need to be derived. The results of this thesis

suggest that it is unlikely that an increase in modeling accuracy would be observed by adding this additional complexity.

Considering only the planar dynamics of the vehicle, it was found that the inclusion of roll dynamics in the physical description of the model makes little difference to the planar motion as long as the roll dynamics are well damped. This result agrees with expectations. However, many vehicles may exist that are lightly damped. For such vehicles, significant differences are predicted in the planar dynamic response, particularly around frequencies near the roll mode of the chassis. One should then expect that, for inputs rich in these frequencies, discrepancies between the 2DOF and 3DOF models will be seen. Such discrepancies are typically not observed when examining highway driving as the steering inputs are generally low frequency. This thesis should illustrate that careful consideration of driver input must be taken into account when studying a vehicle's planar dynamics.

In regards to the roll dynamics models, it is interesting that the planar dynamic response of a plant including the sprung mass in its description is nearly identical to a plant that does not include a sprung mass. However, the response of the vehicle's roll angle to steering inputs may show a difference as large as several decibels. This result is beneficial to the engineer developing vehicle models primarily concerned in modeling planar dynamics. The assumption to ignore the sprung mass allows for a simplification of the plant description and eliminates a parameter that is difficult to directly measure. An additional benefit of the simplified model is that it still is a good description of the behavior of the planar dynamics about the resonant mode of the roll dynamics. However,

if the researcher is also interested in the roll dynamics of the vehicle, then the sprung mass needs to be included in the plant description.

When examining the response of slip angle to steering input, the inclusion of roll steer appears to affect the low frequency response and hence it may be important in the determination of whether a car slides before rolling. However, no apparent difference may be seen in the lateral, yaw, or roll response of a vehicle by including this term compared to a plant that does not include it.

7.3 Conclusions Regarding the Wheel-Lift Prediction Methodology

This thesis presents a method to predict conditions for untripped wheel lift. The most important aspect of this method is that it directly relates driver input to vehicle wheel-lift through a vehicle model, and not through limits on particular states such as accelerations or roll angles. By basing the wheel lift prediction on a dynamic model, the intent is to make clear any interdependencies and frequency-dependent effects that are not obvious when one simply examines the individual vehicle states of lateral velocity, yaw rate, roll rate, and roll angle. One insight in the development of this methodology is that wheel-lift, e.g. the onset of rollover, is directly related to the restoring moment of the suspension and the vehicle's tires. Such a result suggests that simply specifying a roll angle threshold or lateral acceleration threshold for wheel-lift does not necessarily consider the contribution of damping forces – a critical factor in the roll response.

While experimental work remains to check the validity of this method, it is reasonable to assume that it provides an indicator as to the dynamic stability of a

vehicle's roll dynamics when considering wheel-lift. From the results presented, one may infer that, if a given steering command that particularly excites the range of frequencies that produce a restoring moment above the wheel-lift threshold, there is an increased probability that this may occur.

Another primary benefit of the proposed wheel-lift prediction method is that it provides engineers with an indicator of rollover susceptibility without requiring extensive experimental measurements. Further, it directly reveals the frequency range of inputs that should most be examined. Both are great improvements over the SSF or fixed-maneuver experimental methods currently in common use to determine rollover susceptibility.

7.4 Conclusions Regarding Wheel-Lift Mitigation Strategies

It has been shown that if the parameters of a specific vehicle are known within a reasonable accuracy, relatively simple control methods may be used to improve the dynamic response of a vehicle to driver input. Additionally, it was shown that while open-loop methods such as deadbeat control work well when model uncertainty is low, and that a closed-loop method such as Model Reference Control should be used when added robustness is needed.

One important reason for using a robust control algorithm is that vehicles undergo parametric variation and uncertainty in day-to-day use. Using an SUV as an example, any rollover prevention algorithm must be able to work when there is only one passenger and an empty trunk, or when there are six passengers and the trunk is full. Additionally,

regular wear on vehicle components will gradually alter some of the model parameters over time. This is particularly true with the tires on a vehicle which will cause the cornering stiffness and limit friction characteristics to vary.

7.5 Future Work

A major issue that remains to be addressed is the quality of the test data – namely the lateral acceleration data. At the writing of this work, a military grade Differential GPS system and IMU have been purchased and are being integrated into the system architecture of the test vehicle. The system in question is a Novatel DGPS-RT2 system, with a positional accuracy of ±1 cm, velocity RMS of 0.02 m/s, roll and pitch angle RMS of 2.6×10^{-4} rad, and yaw angle RMS of 8.7×10^{-4} rad. The addition of this equipment will allow for a comparison between the data taken in this thesis and a "true source". It will also allow for the direct measurement of vehicle roll angle.

Further investigations into the validity of the wheel-lift prediction method needs to be made. The first stage of this is to examine the frequency content of the standard NHTSA test maneuvers. If the methodology outlined in this work is correct, then the maneuvers that are most noted for causing wheel lift in vehicles undergoing NHTSA testing will most exhibit critical frequencies highlighted by the dynamic method proposed in this thesis.

Additional future work could attempt to directly compare NHTSA rollover ratings to the safety margins observed with the model-based method of this thesis. Such a

correlation would only require as additional data the cornering stiffness, roll stiffness, and roll damping parameters for sample vehicles used in NHTSA testing.

A final area of future study toward the development of the predictive method would be two-fold: First, work should be conducted toward the creation of a rollover resistance metric based on the model-based method. One means to complete this would be to quantify the minimum threshold between sliding and rollover at various frequencies. Second, a new standard test maneuver should be developed to verify the mathematical model of a particular vehicle or vehicle set under varying road conditions. Such a maneuver would contrast the current NHTSA test maneuvers since it would be based off of a frequency-dependent wheel-lift profile that is vehicle-specific. This is opposed to NHTSA's current practice, where the maneuvers are typically based off of the steering angle at which the vehicle experiences 0.3g's of lateral acceleration [5]. By using a time-response maneuver that is designed to excite the roll-mode of the vehicle, the test engineer can be better assured that they are indeed testing the worst maneuver for a specific vehicle.

To address model robustness, sensitivity analysis needs to be performed on the plant to parametric uncertainty. This analysis should be conducted under various control implementations as each method will have differing levels of sensitivity . A goal should be to obtain a more quantitative analysis of the robustness of each control implementation to uncertainties and inaccuracies in the model, the parameters, and the road conditions.

Finally, additional robust control methods need to be examined outside those considered in this thesis. If uncertainty bounds are known ahead of time, one suggested algorithm would be to use H_∞ control. In the event that such specifications are

unavailable or impractical to derive, Model Reference Adaptive Control (MRAC) and Model Predictive Control (MPC) should be investigated as they will allow for the closed loop system to adapt to both parametric and environmental uncertainties as shown in [6, 7].

[1] J. K. Sprague and S.-P. Liu, "Automated Stability Analysis of a Vehicle in Combined Pitch and Roll," presented at Proceedings of the 2002 ASME International Mechanical Engineering Congress and Exposition (IMECE), New Orleans, Louisiana, 2002.

[2] B.-C. Chen and H. Peng, "Differential Braking Based Rollover Prevention for Sport Utility Vehicles with HIL Evaluations," *Vehicle System Dynamics*, vol. 36, pp. 359-389, 2001.

[3] K. T. Feng, Han-ShueTan, and M. Tomizuka, "Decoupling Steering Control for Vehicles Using Dynamic Look-Ahead Scheme," presented at Proceedings of the 5th International Symposium on Advanced Vehicle Control (AVEC), Ann Arbor, Michigan, 2000.

[4] K.-T. Feng, H.-S. Tan, and M. Tomizuka, "Automatic Steering Control of Vehicle Lateral Motion with the Effect of Roll Dynamics," presented at Proceedings of the 1998 American Control Conference, Philadelphia, Pennsylvania, 1998.

[5] United States Department of Transportation, "A Comprehensive Experimental Examination of Selected Maneuvers That May Induce On-Road, Untripped, Light Vehicle Rollover - Phase IV of NHTSA's Light Vehicle Rollover Research Program," National Highway Traffic Safety Administration HS 809 513, October 2002.

[6] C. R. Carlson and J. C. Gerdes, "Optimal Rollover Prevention with Steer-by-Wire and Differential Braking," presented at Proceedings of the 2003 ASME International Mechanical Engineering Congress and Exposition (IMECE), Washington D.C., 2003.

[7] R. Cortesao and N. Bajcinca, "Model-matching control for steer-by-wire vehicles with under-actuated structure," presented at 2004 IEEE/RSJ International Conference on Intelligent Robots and Systems (IROS), Sendai, Japan, 2004.

Appendix A

Equation Reference

A.1 State Space Equations for 3DOF Linear Model Presented by Said Mammar et. al. (Model 2)

$$A_{Mammar} = \begin{bmatrix} \frac{2\left(C_f \cdot \Gamma + C_r \Lambda\right)}{U \cdot \vartheta} & -\frac{-2C_f l_f \Gamma + 2C_r l_r \Lambda + U^2 \mathrm{E}}{U \cdot \vartheta} & \frac{hI_{zz} m_s \left(-K_\phi + m_s gh\right)}{\vartheta} & -\frac{hI_{zz} D_\phi m_s}{\vartheta} \\ -\frac{2\left(C_f \Phi + C_r \Omega\right)}{U \cdot \vartheta} & \frac{2\left(-C_f l_f \Phi + C_r l_r \Omega\right)}{U \cdot \vartheta} & -\frac{I_{xz} m\left(K_\phi - m_s gh\right)}{\vartheta} & -\frac{I_{xz} m D_\phi}{\vartheta} \\ 0 & 0 & 0 & 1 \\ \frac{2\Upsilon}{U \cdot \vartheta} & \frac{2\vartheta}{U \cdot \vartheta} & \frac{I_{zz} m\left(K_\phi - m_s gh\right)}{\vartheta} & \frac{I_{zz} m D_\phi}{\vartheta} \end{bmatrix} \quad \text{A.1}$$

$$I_{eq} = I_{xx} + h^2 m_s \quad \text{A.2}$$

$$\Gamma = I_{xz}^2 - I_{eq} I_{zz} - hI_{xz} l_f m_s \quad \text{A.3}$$

$$\Lambda = I_{xz}^2 - I_{eq} I_{zz} - hI_{xz} l_r m_s \quad \text{A.4}$$

$$\Theta = I_{eq} m + h^2 m_s^2 \quad \text{A.5}$$

$$\vartheta = \left(I_{xz}{}^2 - I_{eq} I_{zz}\right) m + h^2 I_{zz} m_s^2 \quad \text{A.6}$$

$$\Phi = hI_{xz} m_s + l_f \Theta \quad \text{A.7}$$

$$\Omega = hI_{xz}m_s - l_r\Theta \tag{A.8}$$

$$\mathrm{E} = I_{xz}^2 m - I_{eq}I_{zz}m + h^2 I_{zz}m_s^2 \tag{A.9}$$

$$\Upsilon = C_f\left(I_{xz}ml_f + hI_{zz}m_s\right) + C_r\left(-I_{xz}ml_r + hI_{zz}m_s\right) \tag{A.10}$$

$$\vartheta = C_r l_r\left(I_{xz}ml_r - hI_{zz}m_s\right) + C_f l_f\left(I_{xz}ml_f + hI_{zz}m_s\right) \tag{A.11}$$

$$B_{Mammar} = \begin{bmatrix} -\dfrac{2C_f\Gamma}{\vartheta} \\ \dfrac{2C_f\Phi}{\vartheta} \\ 0 \\ -\dfrac{2\left(I_{xz}ml_f + hI_{zz}m_s\right)}{\vartheta} \end{bmatrix} \tag{A.12}$$

$$x_{Mammar} = \begin{bmatrix} V & r & \phi & \dot{\phi} \end{bmatrix}^T \tag{A.13}$$

A.2 State Space Equations for the 3DOF Model Presented by Hyo-Jun Kim and Young-Pil Park (Model 3)

$$A_{Kim} = \begin{bmatrix} \dfrac{2I_{xx}C_0}{U\kappa} & \dfrac{I_{xx}\left(-mU^2 + 2C_1\right) + h^2U^2m_s^2}{U\kappa} & \dfrac{hm_sK_\phi - 2I_{xx}\left(C_f\dfrac{\partial\alpha_{f*}}{\partial\phi} + C_r\dfrac{\partial\alpha_{r*}}{\partial\phi}\right)}{\kappa} & \dfrac{hm_sD_\phi}{\kappa} \\ \dfrac{2C_1}{UI_{zz}} & \dfrac{2C_2}{UI_{zz}} & \dfrac{-2C_fl_f\dfrac{\partial\alpha_{f*}}{\partial\phi} + 2C_rl_r\dfrac{\partial\alpha_{r*}}{\partial\phi}}{I_{zz}} & 0 \\ 0 & 0 & 0 & 1 \\ -\dfrac{2C_0hm_s}{U\kappa} & -\dfrac{2C_1hm_s}{U\kappa} & -\dfrac{mK_\phi - 2C_fhm_s\dfrac{\partial\alpha_{f*}}{\partial\phi} - 2C_rhm_s\dfrac{\partial\alpha_{r*}}{\partial\phi}}{\kappa} & -\dfrac{mD_\phi}{\kappa} \end{bmatrix} \tag{A.14}$$

$$B_{Kim} = \begin{bmatrix} \frac{I_{xx} C_f}{\kappa} \\ \frac{C_f l_f}{I_{zz}} \\ 0 \\ -\frac{C_f h m_s}{\kappa} \end{bmatrix} \quad \textbf{A.15}$$

$$\kappa = I_{xx} m - h^2 m_s^2 \quad \textbf{A.16}$$

$$x_{Kim} = \begin{bmatrix} V \\ r \\ \phi \\ \dot{\phi} \end{bmatrix} \quad \textbf{A.17}$$

$$C_0 = C_f + C_r \quad \textbf{A.18}$$

$$C_1 = l_f C_f - l_r C_r \quad \textbf{A.19}$$

$$C_2 = l_f{}^2 C_f + l_r{}^2 C_r \quad \textbf{A.20}$$

A.3 State-Space Equations for the 3DOF Model Presented by Christopher R. Carlson and J. Christian Gerdes (Model 4)

$$A_{Carlson}\begin{bmatrix} \frac{2\cdot\left(I_{xx}+2mh^2\right)\cdot C_0}{m\cdot U\cdot I_{eq}^*} & \frac{-mU^2I_{eq}+2I_{xx}C_1+4mh^2C_1}{m\cdot U\cdot I_{eq}^*} & \frac{h\left(K_\phi-mgh\right)}{I_{eq}^*} & \frac{hD_\phi}{I_{eq}^*} \\ \frac{2C_1}{I_{zz}U} & \frac{2C_2}{I_{zz}U} & 0 & 0 \\ 0 & 0 & 0 & 1 \\ \frac{-2hC_0}{I_{eq}^*U} & \frac{-2hC_1}{I_{eq}^*U} & -\frac{K_\phi-mgh}{I_{eq}^*} & -\frac{D_\phi}{I_{eq}^*} \end{bmatrix} \quad \textbf{A.21}$$

$$B_{Carlson}=\begin{bmatrix} \frac{-2C_f\left(I_{xx}+2mh^2\right)}{mI_{eq}} \\ \frac{-2l_fC_f}{I_{zz}} \\ 0 \\ \frac{2hC_f}{I_{eq}} \end{bmatrix} \quad \textbf{A.22}$$

$$I_{eq}^*=I_{xx}+h^2m \quad \textbf{A.23}$$